Nano-scale Glucose Fuel Cells for Energy Harvesting in the Human Body Based on Proton Conduction in Cerium Oxide

By

Philipp Simons

M.Sc., Energy Science and Technology
ETH Zurich, Zurich, Switzerland, 2015

B.Sc., Physics
ETH Zurich, Zurich, Switzerland, 2013

Submitted to the Department of Materials Science and Engineering
in partial fulfillment of the requirements for the degree of

DOCTOR OF PHILOSOPHY

at the

MASSACHUSETTS INSTITUTE OF TECHNOLOGY

June 2021

Signature of Author: _____
Department of Materials Science and Engineering
May 21, 2021

Certified by: _____
Jennifer L. M. Rupp
Thomas Lord Associate Professor of Materials Science and Engineering
Thesis Supervisor

Accepted by: _____
Frances M. Ross
Ellen Swallow Richards Professor of Materials Science and Engineering
Chair, Department Committee on Graduate Students

Nano-scale Glucose Fuel Cells for Energy Harvesting in the Human Body Based on Proton Conduction in Cerium Oxide

By

Philipp Simons

Submitted to the Department of Materials Science and Engineering on May 21, 2021
in partial fulfillment of the requirements for the degree of
Doctor of Philosophy in Materials Science and Engineering

Abstract

Future implantable medical devices such as sensors, drug delivery systems, and electroceuticals require efficient, reliable, and highly miniaturized power sources. To date, the predominant power source of implants is the Li–I_2 pacemaker battery, which is limited in its scale-down potential without sacrificing capacity. Therefore, new power sources for implantable devices are needed. In this thesis, a ceramic-electrolyte glucose fuel cell is invented, which constitutes the smallest potentially implantable glucose fuel cell to date. By use of the ceramic proton-conducting electrolyte ceria and a free-standing membrane device architecture, the novel ceramic-electrolyte glucose fuel cell can be scaled down to a thickness below 400 nm. The ceramic-electrolyte glucose fuel cell is biocompatible by materials choice, and unlike polymer-electrolyte glucose fuel cells, can be easily thermally sterilized for future implantation. This thesis demonstrates fabrication, fundamentals and the performance of the first ceramic-electrolyte glucose fuel cells, with a power density of up to 43 μW cm^{-2}, and shows unusually broad performance statistics across 150 devices thanks to a custom-designed measurement apparatus. A fundamental property required to realize such glucose fuel cells was to define a proton-conducting ceramic thin film electrolyte. Therefore, beyond device design and development, this thesis explores the proton transport properties of ceria. Through a ceria model system deposited *via* wet-chemical spray pyrolysis, sufficient proton conductivity is observed. Moreover, slow hydration kinetics, at the order of several days, is detected in ceria, which could explain the large discrepancies of observed proton conductivity in the literature to date. Finally, the structural properties of ceria deposited through spray pyrolysis are studied under various thermal processing conditions, providing guidelines on the cost-effective processing of ceria as a proton-conducting electrolyte. Here, it is found that Raman spectroscopy can be employed to observe texture evolution in ceria thin films, which is relevant for both glucose fuel cells and other catalytic applications. Overall, this thesis constitutes a study of the processing, structure, proton transport, and device development of ceria, resulting in nano-scale ceramic-electrolyte glucose fuel cells that could enable the next generation of miniaturized implants.

Thesis Supervisor: Jennifer L. M. Rupp

Title: Thomas Lord Associate Professor of Materials Science and Engineering

Acknowledgements

This PhD thesis would not have been possible without the amazing people who all, in some way, contributed to this work. Throughout the five-and-a-half years of my PhD, I had the great honor and pleasure to meet and work with some of the smartest and kindest people in the world.

First of all, I would like to thank my advisor Professor Jennifer Rupp for her support, guidance, and mentorship throughout my PhD. I appreciate the opportunity to pursue a PhD in her group and perform research that is creative and risky, but also incredibly rewarding. Also, a great thank you to my committee members Professor Harry Tuller and Professor Michael Cima, who provided valuable guidance and helped me reflect on the research I performed.

Secondly, I am deeply indebted to the incredible students who I had the honor to supervise during my time at MIT, namely Marco Gysel, Steven Schenk, Lorenz Olbrich, and Kierstin Torres. This work would not have been possible without your outstanding contributions, and I have learned so much from you all.

Next, I am incredibly grateful to have worked in a research lab that has been supportive and fun from the first to the last day. The collaborative spirit in the lab, the regular after-work sessions in 50-110, and the overall support I received from everyone in this group were outstanding and mean the world to me. Thank you to Iñigo Garbayo and Yanuo Shi for helping me get this project started. Thank you to Alfonso Carrillo, Felix Messerschmitt, Eva Sediva, Alex Bork, Andreas Nenning, and Reto Pfenninger, for being phenomenal colleagues and great friends, and for being an incredible group to move across the Atlantic with. I also want to thank the great colleagues and friends from the Zurich days who decided to stay in Switzerland, particularly Rafael Schmitt, Sebastian Schweiger and Sören Boyn. Professor Will, thank you for great discussions, convincing me to start rock-climbing, and the occasional beer at the Muddy. I would be amiss to thank the incredible people who joined our lab at MIT: Juan-Carlos Gonzalez Rosillo, Kunjoong Kim, Zach Hood, and Haemin Paik, thanks for all your wisdom and your friendship. Sara Sand, Willis O'Leary, Thomas Defferriere, Jesse Hinricher and Moran Balaish, thank you for great discussions on research and on life. Also thank you Yuntong Zhu, Drew Buzzell, Hyunwon Chu and Kasia Sokol for being great teammates! Also, a huge thanks to Dino Klotz and George Harrington, for help in making sense of my data, and for fun evenings at the Muddy and at conferences. Finally, this work, and most everything this lab does, would be impossible without the incredible support from Josephine Baer in Zurich, and Priyanka Chaudhuri at MIT. Your diligence was exemplary, and your kindness was heartwarming.

I am also deeply thankful to the incredible research staff who supported me through trainings, guidance, and discussions – I learned so much from you and could not have done this work without you. Thank you

to Kurt Broderick, Gary Riggott, and Dennis Ward at MTL, to Charlie Settens and Tim McClure at MRL, and to Tim Cavanaugh at Harvard CNS. A huge thank-you to Adam Shervanian, for single-handedly getting our labs running at MIT, and for your support with the small and large requests we had over the years. I am also deeply thankful to the academic staff at DMSE, Angelita Mireles and Dominique Altarejos, for always being available to help when I had an administrative question, and always being friendly and kind. Also thank you Lars Llorente for your help and support to me and the lab.

I also want to acknowledge the funding sources that enabled me to pursue risky and ambitious research ideas during my PhD: the Broshy Fellowship, the Hugh Hampton Young Fellowship, and Merck KGaA in Germany.

Outside of the lab, I have had the honor to call some incredibly kind and smart people my friends. I am thankful to Tim, Elad, Anshi, and Parker for always having an open ear, and being the most supportive and selfless friends. Thank you to the B+ - crew Max, Katherine, Jackie, Parker, Jasper, George, and Kate for making the first year bearable, lifting heavy items off the ground, and many fun nights dancing to Shakira. Thank you to Eesha for your contagious enthusiasm, and to Zach for being a great IM buddy. I am also tremendously grateful for the fantastic people I met through the GAC, and who became some of my best friends: Affi, Jens, Jonas, Chris, Kathi, Rahel, Daniel, D, Yannik, Yukio, and Till. A big thank-you also goes out to Isabel for being a great friend when I needed it the most.

Throughout the last year, I also had the incredible fortune to become part of the LGO community, and the tight bonds that this program produces does not stop to amaze me. Thank you to the best core team in the history of the program, The Flying Kiwis: Chris, Ben, Lois, Mike, Sean, and Amit, and also to Anjali and Alex for your friendship and support inside and outside of classes. In addition, I am hugely thankful for the all the help I got from the LGO staff, in particular Patty and Ted, and the financial support from the LGO program. A huge thank you also goes out to the best MBA core team, the incredible Pac Cranes Haley, John, Rachel, Tianbo, Chris, and Yas: Cranez4Lyfe.

I am eternally grateful for the support and love from my family: My mom Antonette, my dad Axel, and my brothers Jan and Peter. This PhD, and most anything in my life, would not have been possible without your unconditional support and understanding. DANKE!

Finally, I want to thank my better half Linn: Your support and love mean the world to me, and I am grateful to have my best friend as my partner. I am beyond excited for what the future holds for us.

Table of Contents

Abstract 3

Acknowledgements 5

Table of Contents 7

List of Figures 11

List of Tables 19

1. Chapter 1: Introduction 20

1.1 Glucose Fuel Cells 20

1.1.1 Glucose Fuel Cell Types 21

1.1.2 Catalysis in Glucose Fuel Cells 21

1.1.3 Operation Under Mixed Fuel Containing Both Glucose and Oxygen 23

1.1.4 Historical Development of Glucose Fuel Cells 25

1.1.5 Physiological Operating Conditions for Implantable Glucose Fuel Cells 27

1.2 Proton Conductivity in Solids 29

1.2.1 Overview of Solid-State Proton Conductors 29

1.2.2 Proton Conduction in Ceria – Mechanistic Insights 32

1.3 Open Research Questions 34

1.4 Thesis Outline 35

2. Chapter 2: Ceramic-Electrolyte Glucose Fuel Cell for Implantable Electronics 36

2.1 Introduction 37

2.2 Results and Discussion 43

2.2.1 Ceramic-based glucose fuel cell design and electrochemical operational principle 43

2.2.2 Designing ceramic glucose fuel-cell functional components with high degree of miniaturisation 44

2.2.3 Overall cell resistance and electrolyte conductivity via electrochemical impedance spectroscopy 47

2.2.4 OCV statistics of 150 ceramic glucose fuel cells and power generation performance via IV curves 49
2.3 Conclusion 53
2.4 Experimental Methods 54
2.4.1 Overview 54
2.4.2 Fuel-cell fabrication 54
2.4.3 Characterisation and measurements 55
3. Chapter 3: Ceramic-Electrolyte Glucose Fuel Cell Design Evolution and Developing a Glucose Fuel Cell Testing Apparatus 57
3.1 Introduction 58
3.2 Operational principle of glucose fuel cells 60
3.3 Materials Selection 61
3.3.1 Functional Considerations of Ceria as the Proton-Conducting Electrolyte 61
3.3.2 Functional Considerations of Platinum Electrodes for Selective Catalysis and Microfabrication 62
3.4 Device Geometry 64
3.5 Fabrication Process 66
3.5.1 Microfabrication route 66
3.5.2 Pt Electrode Deposition and Optimization for the Glucose Fuel Cell 68
3.5.3 Ceria Electrolyte Thin Film Deposition Optimization for the Glucose Fuel Cell 69
3.5.4 Overall Fabrication Yield 73
3.6 Designing a Glucose Fuel Cell Test Setup for Electrochemical Characterization 74
3.6.1 Measurement Enclosure: Liquid Flow Case 75
3.6.2 Characterization Setup: Periphery 77
3.7 Glucose Fuel Cell Design Stages 79
3.8 First Experiments 80
3.8.1 Initial Tests: OCV Under Stagnant Conditions 80
3.8.2 OCV Measured in Liquid Flow Case 82

3.9 Conclusion 82
4. Chapter 4: Careful Choices in Low Temperature Ceramic Processing and Slow Hydration Kinetics Can Affect Proton Conduction in Ceria 85
4.1 Introduction 86
4.2 Results and Interpretation 90
4.2.1 Microstructure and Phase Analysis 90
4.2.2 Temperature-dependent Impedance under Dry and Moist Air 91
4.2.3 Time-dependent Proton Conductivity 96
4.2.4 The Influence of Thermal Annealing on Conductivity 97
4.3 Conclusions 102
4.4 Experimental Methods 104
4.4.1 Sample Preparation 104
4.4.2 Characterization 104
5. Chapter 5: Deposition Parameters and Raman Crystal Orientation Measurements of Ceria Thin Films Deposited by Spray Pyrolysis 105
5.1 Introduction 106
5.2 Experimental Methods 109
5.3 Results and Interpretation 111
5.3.1 Film Critical Thickness 111
5.3.2 Structural and Phase Evolution of Spray Pyrolysis Manufactured Films 113
5.3.3 Raman Analysis 120
5.4 Conclusions 127
6. Chapter 6: Conclusions and Future Directions 128
6.1 Conclusions 128
6.2 Future Directions 129
6.2.1 Mechanistic Studies of Ceramic Glucose Fuel Cell Operation 129
6.2.2 Future Ceramic-Electrolyte Glucose Fuel Cell Development for *in-vivo* Operation 130

7. Biographical Notes and Publications 133

8. Appendix 135

8.1 Appendix A: Supplementary Information to Chapter 2 135

8.2 Appendix B: Supplementary Information to Chapter 4 140

8.3 Appendix C: Supplementary Information to Chapter 5 141

8.4 Appendix D: Preliminary Mechanistic Studies of Losses in the Ceramic-Electrolyte Glucose Fuel Cell System 144

9. References 147

List of Figures

Figure 1.1: Categorization of glucose fuel cells. **a)** On the highest level, glucose fuel cells can be separated between *implantable* glucose fuel cells to power implantable devices, and *external* glucose fuel cells which serve as stationary power sources. **b)** Among implantable glucose fuel cells, three different catalyst types can be employed, namely abiotic, enzymatic and microbial catalysts. [23–25] **c)** Abiotically catalyzed implantable glucose fuel cells can in turn be categorized by their design to create operation under a mixed fuel. Here, selective catalysis at the two electrodes, a depletion design which creates a concentration gradient in the cell, and perm-selective membranes have been proposed as possible configurations. 22

Figure 1.2 Solid-state proton conductors sorted by operating temperature. **a)** Perovskite oxides are frequently employed in protonic-ceramic fuel cells (PCFCs) with operating temperatures of ~500 °C, but their toxicity is prohibitive for implantable applications. **b)** Solid acids can be used as intermediate temperature fuel cell electrolytes, however, they are soluble in water. **c)** Proton exchange membranes such as Nafion are commonly used in fuel cells operating around 90 °C. They have good proton conductivity, but are not thermally sterilizable and limited in their miniaturization potential. d) Fluorites such as ceria conduct protons at temperatures as low as body temperature, and are non-toxic and thermally stable. They form a promising candidate material to be used as a ceramic electrolyte for implantable glucose fuel cells. Structures reproduced from [73,74]. 30

Figure 1.3 Models of proton transport modes in ceria. a) Gregori et al. propose that protons can be transported 1. through the grain, 2. along grain boundaries (denoted as GB) in the interior, 3. along an adsorbed water layer and/or 4. within an enriched water layer just below the surface.[83] b) Manabe et al. describe these same modes of proton transport, and in addition, suggest that the surface above a bulk grain (denoted as intra-grain transport above a single grain) and above a grain boundary (denoted as inter-grain transport between different grains) exhibit different proton transport resistances.[79] Both models suggest that proton transport in ceria is dominated by surface proton conduction. 32

Figure 2.1 Techno-historical timeline of implant technology and implantable power source development. Implantable devices and their power sources have affected each other since the 1960s. The dominant implantable power source for most established, market-stage devices to date is the LiI_2 pacemaker battery, invented in 1971. Recent trends in implant technology include increased miniaturisation and neural interfacing, sparking a new push for highly miniaturised, long-term-stable implantable power sources. New power sources, e.g., tribo-electric and piezo-electric nano generators, aim to combine efficient energy harvesting with on-chip integration to meet the requirements of new, miniaturised implantable devices.[2,11,21,31,32,101–105] 39

Figure 2.2 Schematic of glucose fuel cell, chip and individual device. a) Schematic of a ceramic glucose fuel cell based on a free-standing membrane of a porous Pt anode / CeO_2 electrolyte / dense Pt cathode. **b)** Optical photograph of fuel-cell chip containing 30 individual glucose fuel-cell devices. **c)** Optical microscopy image of an individual free-standing ceria membrane. 43
Figure 2.3 Schematic of ceramic glucose fuel cell and SEM analysis of its components. a,b) Schematic of ceramic glucose fuel cell consisting of free-standing ceria membrane as the proton-conducting electrolyte, a porous Pt anode, and a dense Pt cathode. **b)** Two different microstructures of the ceria electrolyte were employed, namely a dense, columnar microstructure (left) and a rough, cauliflower-like microstructure (right). **c, d)** Top-view **(c)** and cross-sectional view **(d)** SEM micrographs of the dense ceria electrolyte microstructure. **e, f)** Top-view **(e)** and cross-sectional view **(f)** SEM micrographs of the rough ceria electrolyte microstructure. **g, h)** SEM images of different magnifications of the porous Pt anode. **i, j)** Cross-sectional SEM images at different magnifications of a full glucose fuel cell, measuring 370 nm in thickness and consisting of a porous Pt anode (top), rough ceria ceramic proton-conducting electrolyte (middle), and dense Pt cathode (bottom). 45
Figure 2.4 Impedance and proton conductivity of glucose fuel-cell devices. a) Impedance spectrum and equivalent circuit for a glucose fuel-cell membrane at 23.5 °C. **b)** Arrhenius-type plot of conductivity of the fuel-cell system extracted from EIS measurements, proving protonic conductivity at low temperatures in the hydrated case. **c)** Mechanism of proton conductivity through the rough ceria electrolyte structure. 48
Figure 2.5 Performance and comparison of ceramic glucose fuel cells. a, b) Histograms of the open-circuit potentials of **(a)** 120 ceramic glucose fuel cells with dense ceria electrolyte and **(b)** 30 ceramic glucose fuel cells with porous ceria electrolyte. **c)** Test setup allowing for rapid screening of 30 individual glucose fuel-cell devices through spring-loaded needles and plug board. **d)** Polarisation curve of a ceramic glucose fuel cell, exhibiting a peak power density of 43 $\mu W\ cm^{-2}$. **e)** Comparison of previously reported polymer-electrolyte-based glucose fuel cells with those in this work, *i.e.,* ceramic-electrolyte glucose fuel cells: power density as a function of fuel-cell thickness. The ceramic glucose fuel cells show 3 times higher miniaturisation and higher power densities than existing abiotic glucose fuel cells.[29,41,123–126] 50
Figure 3.1 Overview over different implantable devices, from mature technologies such as the pacemaker, cochlear implant, or drug delivery systems, to new classes of devices such as deep brain neural stimulators, electroceutical or implantable sensors. Implantable devices follow two trends: they are being increasingly miniaturized in order to minimize their impact on patients and they require a steady supply of energy between100 nW to 1 mW. 58
Figure 3.2 Operation principle of a glucose fuel cell. At the anode, glucose is oxidized to form gluconic acid, which releases two protons and two electrons. The protons travel through the electrolyte to the

cathode, where they react with oxygen and electrons to form water. The electrons travel from the current collectors through an external circuit powering a load. 61
Figure 3.3 Schematic of the geometric layout of the ceramic on-chip glucose fuel cell. **a)** Glucose fuel chip with 30 membranes consisting of a ceria solid electrolyte and top/bottom Pt electrodes, and cross-sectional schematic of an individual glucose fuel cell membrane, measuring a total thickness of 370 nm. **b)** Alpha design stage: First iteration of the glucose fuel cell design, with the top and bottom of the device fully covered with Pt, such that all 36 glucose fuel cells are connected simultaneously. **c)** Beta design stage: Second iteration of the geometric layout, where each glucose fuel cell has an individual contact pad such that devices could be probed individually. Because of space requirements, the number of devices was reduced to 30 in this layout. 65
Figure 3.4 Microfabrication route to fabricate ceramic-electrolyte glucose fuel cells. The microfabrication route is based on standard semiconductor fabrication processes for easy on-chip silicon integration of the glucose fuel cell device. A combination of photo-lithography, reactive ion etching, wet etching, magnetron sputtering, and pulsed laser deposition is employed. Two different fabrication routes were explored. **a)** In Route 1, the Si_xN_y support layer is removed via reactive ion etching immediately after the ceria electrolyte deposition. **b)** In Route 2, the porous Pt anode is deposited first as an additional mechanical support, before removal or the Si_xN_y support layer 67
Figure 3.5 Geometric configuration of free-standing membranes fabricated via anisotropic silicon etching with KOH. A square opening measuring 840 µm × 840 µm is etched into Si_xN_y using photolithography and reactive ion etching. The anisotropic etch of silicon with KOH creates a characteristic angle of 54.7° by etching along the (111) plane, which results in a free-standing membrane of Si_xN_y measuring 300 µm × 300 µm. 68
Figure 3.6 Schematic of ceria electrolyte microstructures. **a)** Schematic of the glucose fuel cell free-standing membrane configuration. **b)** Schematic of a dense, columnar ceria microstructure assembled via a low PLD oxygen background pressure of 0.026 mbar. **c)** Schematic of a rough, disordered, cauliflower-type microstructure obtained via a high PLD oxygen background pressure of 0.078 mbar. 70
Figure 3.7 Overview of the different ceria electrolyte microstructure designs. **a-d)** SEM micrographs of **a,c)** dense and **b,d)** rough ceria electrolyte. **a)** Top view and **c)** cross-sectional SEM micrograph of dense ceria, showing a dense, columnar microstructure. **b)** Top view and **d)** cross-sectional SEM micrograph of rough ceria, showing a disordered, cauliflower like microstructure. **e-h)** Optical micrographs of free-standing ceria membranes, **e,f)** prior to and **g,h)** after the removal of the Si_xN_y support layer below the ceria electrolyte. e) Dense ceria shows significant buckling before Si_xN_y removal, whereas **f)** rough ceria does not show any visible buckling prior to Si_xN_y removal. **g,h)** After removal **g)** dense ceria shows stronger

buckling with narrower ridges compared to **h)** rough ceria. These images before and after Si_xN_y removal indicate significantly lower stress in rough ceria membranes than in dense ones. 73
Figure 3.8 Liquid flow case as measurement enclosure, and rapid-screening contacts. **a, b)** CAD drawing of the custom-designed liquid flow case, in **a)** closed and **b)** open form. The glucose fuel cell chip is placed in a tightly fitted slot, and liquid sealing is achieved with silicone paste. Glucose solution flows over the top side or anode of the chip, whereas the bottom side or cathode is exposed to ambient air as the oxygen source. **c-e)** Enhanced characterization setup with the ability to perform rapid screening and contact all 30 individual glucose fuel cells in a reproducible and controlled fashion. This is enabled through a plugboard for electrical contact and **e)** spring loaded needles for reliable contacting. 77
Figure 3.9 Photographs of the full characterization setup including the liquid flow case, as well as gas and liquid handling, and electrical connections. A peristaltic pump was used to pump glucose solution from a water bubbler for deaeration to the glucose fuel cell flow case. The setup was placed inside a metallic Faraday cage for shielding during measurements, and the flow case was placed on a hot plate for electrochemical characterization at elevated temperature..... 78
Figure 3.10 Pictures and OCV of a preliminary ceramic-electrolyte glucose fuel cell. a) Post-mortem optical photograph of the first successfully assembled glucose fuel cell chip with free-standing glucose fuel cell membranes. b) Optical micrograph of an individual free-standing membrane device functioning as a ceramic glucose fuel cell. c) OCV profile of the glucose fuel cell, where each sharp peak in the voltage corresponds to the addition of a droplet of glucose solution to the surface of the fuel cell device. OCV peaks are negative due to the polarization of the measurement. A peak OCV of 140 mV was observed, verifying the electrochemical activity of the ceramic glucose fuel cell chip..... 81
Figure 3.11 OCV measurement of a preliminary glucose fuel cell placed inside the custom-made flow case. Blue regions correspond to the flow of pure water, and the yellow region corresponds to the flow of glucose solution in PBS. The OCV reached a peak value of 57 mV after the fuel supply was switched to glucose solution, and decays to -10 mV after switching back to pure water. This verifies that the glucose solution is the source of the observed OCV. The device failed after 5 minutes..... 83
Figure 4.1 a) Ionic conductivity of various ionic conductors as a function of temperature.[48,72,140-142] **b)** Schematic of a hydrated ceramic showing the two types of proton transport mechanisms: the vehicular mechanism in which hydroxyl or hydronium ions carry charge along the surface water layer and the Grotthus mechanism where protons hop between water molecules. Regions where proton transport occurs in the hydrated ceramic are shown as 1) bulk 2) grain boundary 3) proton enriched layer in the grain 4) surface of bulk 5) surface of grain boundary. 87
Figure 4.2 a) Optical micrograph of the as-deposited film, deposited via spray pyrolysis. **b-c)** Top view scanning electron micrograph of the as-deposited **(b)** and the post-annealed film **(c)**, confirming that

smooth, dense, thin films were deposited. **d)** X-ray diffraction patterns of the as-deposited (black) and post-annealed (red) films with fluorite structure ceria reference for comparison (black). As films are annealed, peak width decreases, and intensity increases as a result of increasing grain size and crystallinity..... 91

Figure 4.3 a) Arrhenius plot of extracted conductivities from impedance measurements taken in dry and moist atmospheres for the as-deposited film. Two temperature regions are shown: Region I with Arrhenius-like conduction behavior indicating oxygen ion conduction, and Region II with increasing conduction for decreasing temperature indicating proton conduction. In Region II, dry air conductivity was below the detection limit of the impedance bridge used and hence not seen in the plot. **b-c)** Exemplary impedance spectra under moist and dry air at low (25 °C and 50 °C) and high (400 °C) temperatures, respectively, with peak frequencies labeled. **b)** At low temperatures under moist air, a compressed impedance arc is observed, attributed to proton conductivity. **c)** At higher temperatures under both dry and moist air, two arcs are observed, with the low frequency arc attributed to oxygen ion conduction along the interfaces within the film and the high frequency arc to oxygen ion conduction through the grain bulk. **d)** Equivalent circuit used for fitting impedance spectra, representing grain bulk, interface (grain boundary and amorphous-to-crystalline interfaces), and electrode impedance contributions. 93

Figure 4.4 Nyquist plot of the as-deposited film starting under dry air (red) **a)** over 5.5 hours under moist air (blue) and **b)** over 74 hours after thermal cycling to 400 ºC under moist air (blue), revealing the long equilibration times and slow hydration kinetics: Proton conductivity initially stabilized after 5 hours under moist air, however after thermal cycling to 400 ºC, conductivity significantly increased and took an additional 47.5 hours to reach steady state. 97

Figure 4.5 Conductivity of the as-deposited film as a function of time at 25 ºC **a)** over >100 hours under moist air and **b)** magnification of the first 6 hours under moist air, before thermal cycling to 400 ºC. After 76 hours of exposure to moist air (47.5 hours after thermal cycling) conductivity stabilized to a value of $9 \cdot 10^{-6}$ S/cm, showing the extremely slow kinetics of the equilibration process. An exponential relaxation was fitted to guide the eye. 98

Figure 4.6 Nyquist plot with maximum frequencies of as-deposited and post-annealed films at **a)** 25 ºC under moist air and **b)** at 400 ºC under moist air with peak frequencies labeled. Annealing increases both the proton conductivity at low temperatures and the overall oxygen ion conductivity at high temperatures by approximately one order of magnitude which is explained by a change in interface density and amorphous-to-crystalline ratio caused by annealing the film. 99

Figure 4.7 Room temperature proton conduction pathways for biphasic films **a)** as-deposited and **b)** annealed at 500 ºC. The lower conductivity pathway is through the amorphous phase (red) and the higher conductivity is along the amorphous-crystalline interface and grain boundaries (green). As films are

annealed, grain size increases and the amorphous phase fraction decreases, increasing the amount of high conductivity paths and explaining the increase in the overall proton conductivity of annealed films..... 100
Figure 5.1 a) Schematic of the thickness gradient stemming from volume of precursor deposited during spray pyrolysis with optical micrographs of a sprayed wafer deposited at 500 °C from the center to 4 cm away. **b)** Film thickness as a function of distance from the center of a sprayed silicon wafer, with a critical thickness of 300 nm for all deposition temperatures. 112
Figure 5.2 XRD of as-deposited sprayed films deposited at 350 °C, 400 °C, 450 °C, and 500 °C. Broad, weak ceria peaks are observed, corresponding to largely amorphous ceria with dispersed nano-crystallites. 114
Figure 5.3 XRD of as-deposited and annealed films deposited at **a)** 350 °C **b)** 400 °C **c)** 450 °C **d)** and 500 °C. For all films, annealing causes XRD peaks to become sharper and more intense. For thin films deposited at 450 °C and 500 °C, annealing induces significant texture in favor of <100> orientations..... 115
Figure 5.4 Average grain size as a function of annealing temperature calculated using the Scherrer equation for the (111) peak. Post-annealing induces crystallization and grain growth of the largely amorphous as-deposited ceria thin films. 116
Figure 5.5 Raman spectra of a sprayed film as-deposited at 350 °C and annealed at 500 °C, 650 °C, and 800 °C. All films show sharp F_{2g} Raman peaks, and the film as deposited shows a signature of the organic precursor, indicating that organic precursor was incorporated into the film during deposition. 121
Figure 5.6 Raman spectra of the F_{2g} peak of as-deposited and annealed films deposited at **a)** 350 °C, **b)** 400 °C, **c)** 450 °C, **d)** and 500 °C. 122
Figure 5.7 F_{2g} Raman peaks positions as a function of annealing temperature. Two regions are observed in the Raman F_{2g} peak position. Region I: For as-deposited films and some films annealed at 500 °C, the F_{2g} peak is below the bulk ceria value of 465 cm^{-1}. Region II: High temperature annealed films show a F_{2g} peak position above 465 cm^{-1}. 123
Figure 5.8 F_{2g} Raman peaks positions as a function of annealing temperature, for annealed thin films. The Raman F_{2g} peak position is correlated with the increasing (200) texture coefficient observed in annealed ceria thin films. 126
Figure 6.1 Development of the ceramic-electrolyte glucose fuel cell from **a)** a dual chamber, air-breathing cathode configuration, to **b)** the operation under two separate mixed, liquid fuel streams, and finally to **c)** a true single-chamber glucose fuel cell with a single fuel containing glucose and oxygen in solution..... 130
Figure 8.1 Microfabrication route to fabricate free-standing ceria membranes as glucose fuel cell devices. 135
Figure 8.2 Optical micrographs of ceria membranes with dense **(a,b)** and porous **(c,d)** microstructure. Images **a)** and **c)** were captured before the deposition of the porous top-electrode and before the removal of

the Si_xN_y support layer via reactive ion etching. Images **b)** and **d)** were captured after top-electrode deposition and Si_xN_y support layer removal. It can be seen that the dense microstructure shows a higher stress state, manifested in the more pronounced buckling pattern. For the porous microstructure, stress is released during deposition. In particular, before removal of the Si_xN_y support layer, the membrane with a rough microstructure does not show a visible buckling pattern at all, indicating significantly reduced stress in the film. 136

Figure 8.3 (a) X-ray diffraction pattern and **(b)** Raman spectrum of a ceria ceramic electrolyte thin film. The XRD pattern confirms the phase-pure, cubic fluorite structure of cerium oxide, in agreement with ICDD:00-067-0121. In the Raman spectrum, a single, sharp peak at 465 cm^{-1} is observed, corresponding to the F_{2g} oxygen breathing mode of cerium oxide. The data is in good agreement with the literature.[118]. 137

Figure 8.4 Precipitates observed during post-mortem analysis. SEM and EDS analysis shows that precipitates forming at the surface of glucose fuel cells are Na-containing depositions, i.e. likely salts precipitating from the glucose/PBS solution. 138

Figure 8.5 Measurement setup used to perform glucose fuel cell electrochemical performance measurements. Detailed accounts for the design of this setup are provided in Chapter 3 of this thesis. .. 138

Figure 8.6 a) Exemplary time profile of fuel cell voltage and current density over the course of more than 10 hours. **b)** Voltage and power density as a function of time for record performing glucose fuel cell, extracted from the time series reported in **a)**. 139

Figure 8.7 a) Optical micrograph of post-annealed film. **b)** Scanning electron micrograph of an un-annealed film, confirming a dense deposition. A large drift made thickness analysis impossible. **c)** Scanning electron micrograph of a post-annealed film with a small amount of cracks and **d)** magnified micrograph of a crack. 140

Figure 8.8 Schematic of spray pyrolysis deposition chamber 141

Figure 8.9 Optical micrograph of films deposited at an air pressure of **a)** 0.5 bar, **b)** 1.0 bar, and **c)** 1.5 at otherwise fixed deposition conditions. Optical micrograph of films deposited at **d)** 266 minutes, **e)** 332 minutes, and **f)** 420 minutes at otherwise fixed conditions (with the exception of **a)** being deposited at 0.6 bar and the others at 0.4 bar). 141

Figure 8.10 Micrograph of film along wafer from left to right: center, 1-4 cm from the center deposited at a) 350 C, b) 400 °C, and c) 450 °C. Scale bar valid for all micrographs. 143

Figure 8.11 Temperature-dependent electrochemical impedance spectroscopy performed under dry air, and extracted total conductivity plotted in an Arrhenius-type plot. The observed activation energy is 0.35 eV, which is in good agreement with electronic conductivity in ceria. 145

Figure 8.12 Electrochemical impedance spectroscopy under bias, performed under dry air conditions. A decreasing impedance with increasing bias indicates that grain boundaries or interfaces are dominant in charge transport at these temperatures. 145

List of Tables

Table 1.1 Typical physiological operating conditions of glucose fuel cells 28

Table 4.1 Proton conductivity onset temperatures reported from literature for fluorite-structured oxides with varying synthesis methods, processing temperatures, and microstructures. The onset temperature in this work varies from previous studies due to differences in microstructure, crystallinity, and processing conditions. 95

Table 5.1 (200)-Texture coefficient and lattice constant (calculated from the (111) peak) of films at the four annealing and deposition temperatures. Texture in the <100> direction increases with annealing, and no trend is observed in the lattice constant with annealing 118

Table 5.2 Raman F_{2g} peak positions for different deposition and annealing temperatures. 124

1. Chapter 1: Introduction

1.1 Glucose Fuel Cells

Implantable medicine today is rapidly evolving from traditional passive devices and simple electronic systems, to complex, highly miniaturized electronic devices. A major challenge in today's implantable medicine is that the miniaturization of biomedical implantable devices such as sensors, drug delivery systems and bioelectronics requires small, powerful and long-lasting power sources. For example, in recent years the emerging field of bioelectronic medicine has seen significant interest in research and industry, most notably through the establishment of Galvani Bioelectronics, a $715 million joint venture between GlaxoSmithKline and Google parent Alphabet's life science unit Verily, which was announced in August 2016.[1] This joint venture is developing micro-implants, which stimulate specific nerves to precisely treat chronic diseases such as diabetes, arthritis or asthma. Another example of novel highly miniaturized bioelectronic implants is so-called neural dust, highly miniaturized sensor implants that can track and modulate signals of the nervous system.[2] This field has also attracted significant interest from the biomedical industry, e.g. with the acquisition of Iota Biosciences for a total of $429 million including planned investments by Astellas in 2020.[3] However, in order to power such miniaturized implants and enable further miniaturization, a new class of miniature implantable power sources is needed. Traditionally, batteries are used to power implants such as pacemakers, however, those are based on rather bulky set-ups and require replacement by surgery on the patient due to their limited battery-life time every 7-10 years.[4] This is not just a major inconvenience for the patient, but puts the patient at an increased risk of complications such as infections at the implantation site, bleeding, or anesthesia-related complications. A study has found that the complication rate for pacemaker replacement or upgrade surgeries is 18.7%.[5]

Among the plethora of suitable energy storage and conversion devices, batteries store their energy inside the active components, *i.e.,* the electrodes, in chemical bonds and therefore increasing the energy content of a battery means that the size of the battery needs to be increased. In contrast, fuel cells are not limited by a specific storage capacity exhibited by batteries if they use energy sources readily available in the body, such as glucose. This makes glucose fuel cells candidates for small scale, long term implantable power sources, and explains the increased research efforts in recent years.[6–8] After an initial spark of interest in the 1960s, the attention of implantable power source research shifted towards pacemaker batteries in the subsequent years. However, recently, miniaturized bioelectronics have received great attention, and with this, interest in long term, small-scale power sources such as glucose fuel cells has been revived.

1.1.1 Glucose Fuel Cell Types

Glucose fuel cells can be most broadly categorized into external and implantable glucose fuel cells, see **Figure 1.1 a**. External glucose fuel cells serve as stationary power sources, and convert glucose as a primary component of biomass into electricity. As such, external glucose fuel cells are bio-fuel cells that constitute a promising candidate to replace fossil fuel systems in the pursuit to a greener energy supply. Glucose fuel cells typically do not require the feedstock to be fully purified, which opens up the opportunity to use them for harvesting energy from biomass sources such as agricultural waste.[8,9] Implantable glucose fuel cells, in contrast, serve to be implanted into the human organism in order to power implantable biomedical devices. They form an alternative to other implantable power sources such as batteries,[10–12] wireless transfer through RF, microwave, or inductive electromagnetic means,[13,14] ultrasonic energy transfer,[2] and thermoelectric,[15,16] triboelectric,[17,18] or piezoelectric generators.[19,20] To date, the pacemaker battery, a primary battery based in Li-I_2 chemistry, is the predominant energy source of implantable devices.[21] However, batteries such as the pacemaker battery store their energy in the anode and cathode, and therefore, increasing the available energy requires an increase in volume. This has drastic consequences: for a typical pacemaker today, the battery constitutes at least 50% of the volume of the implant.[22] The large battery volume is a critical challenge for the miniaturization of implantable devices since it is desired to minimize the size of an implant, and therefore its impact on the patient. Implantable glucose fuel cells do not require volume to store energy; rather, they convert energy that is readily available inside the human body into electricity. This means that they constitute a power source with significantly lower volume than batteries. In addition, batteries require replacement surgery whenever the stored energy in the battery is depleted. In contrast, glucose fuel cells harvest energy that is readily available inside the human body, which means that in principle they form a perpetual power source that does not require a replacement surgery.

1.1.2 Catalysis in Glucose Fuel Cells

Glucose fuel cells can be categorized by the type of catalyst used to catalyze the electrode reactions, i.e. the oxygen reduction reaction and the glucose oxidation reaction. Three types of catalysts are commonly employed in glucose fuel cells, namely enzymatic, microbial and abiotic catalysts, **Figure 1.1 b**.

Enzymatic Catalysts

Enzymatic glucose fuel cells constitute the most common type of glucose fuel cells researched to date. In this type of fuel cell, isolated enzymes are stabilized on the electrode surface to catalyze the respective

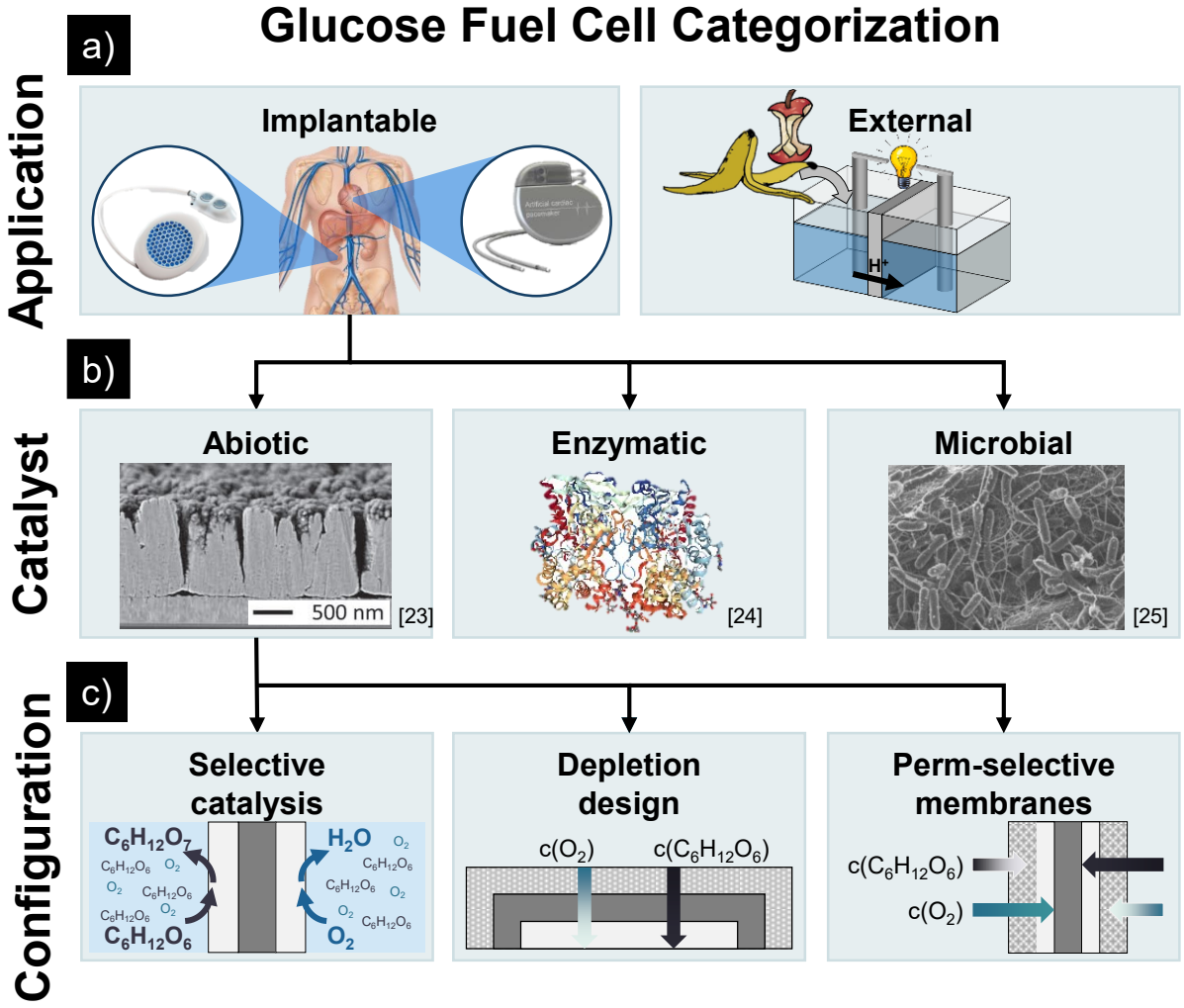

Figure 1.1: Categorization of glucose fuel cells. **a)** On the highest level, glucose fuel cells can be separated between *implantable* glucose fuel cells to power implantable devices, and *external* glucose fuel cells which serve as stationary power sources. **b)** Among implantable glucose fuel cells, three different catalyst types can be employed, namely abiotic, enzymatic and microbial catalysts. [23–25] **c)** Abiotically catalyzed implantable glucose fuel cells can in turn be categorized by their design to create operation under a mixed fuel. Here, selective catalysis at the two electrodes, a depletion design which creates a concentration gradient in the cell, and perm-selective membranes have been proposed as possible configurations.

electrode reactions. Glucose oxidase and laccase oxidase are the most commonly used enzymes for enzymatic glucose fuel cells.[7] Enzymatic glucose fuel cells benefit from the high selectivity of enzymes, in particular of glucose oxidase toward the electro-oxidation of glucose. Electron transfer between a stabilized, isolated enzyme and its metallic support is difficult due to the electronically insulating nature of the surrounding protein matrix. However, electron transfer can be enhanced through two different methods:

in mediated electron transfer, a mediator material that is typically a low-molecular-weight redox-active species serves to transfer electrons between the enzyme and the electrode. In direct electron transfer, electrons are transferred directly between the redox-active site of the enzymatic catalyst and the electrode substrate.[7]

Microbial Catalysts

Microbial catalysts use electroactive microbes to catalyze the electrochemical conversion of oxygen and glucose to electrical energy.[26] There are major concerns to use microbes in implantable devices, however, due to fears of infection caused by the bacteria used in such microbial glucose fuel cells. Therefore, microbial glucose fuel cells are not seriously considered for implantable applications, but have a high potential to function as stationary power sources that convert biomass. For such stationary applications, microbial glucose fuel cells have the benefit that they typically do not require full purification of feedstocks, which means they can convert relatively low quality feedstocks such as agricultural waste.[8,9]

Abiotic Catalysts

Abiotic catalysts are non-biological materials such as noble metals, ceramics, carbon, or composites thereof, that catalyze the electrode reactions of glucose fuel cells. While abiotic catalysts were investigated already during the 1960s, they have recently received increased interest for implantable glucose fuel cell applications, since they promise to overcome some of the challenges associated with enzymes. Abiotic catalysts promise better long-term stability than their enzymatic counterparts since the materials involved are inherently more robust and stable. Such materials include noble metals and their alloys as well as activated carbon or carbon nanotubes. While abiotically catalyzed glucose fuel cells generally show lower power output performance than enzymatic glucose fuel cells due to lower selectivity and activity, these drawbacks are outweighed by long-term stability and the ability to be easily integrated into micro-electro-mechanical (MEMS) devices.

1.1.3 Operation Under Mixed Fuel Containing Both Glucose and Oxygen

When implanted, a major challenge toward the operation of glucose fuel cells is the presence of both fuel types in the same liquid, i.e. that both oxygen and glucose are present in body fluids such as blood or interstitial fluid. This forms a stark contrast to conventional, hydrogen-based fuel cells, where both fuels are usually stored in separate tanks and each electrode only faces one of the reactants. Therefore, it is crucial for the operation of implantable glucose fuel cells to ensure that each electrode can operate under the presence of the other electrode's fuel, i.e. that at the cathode, the oxygen reduction reaction occurs under

the presence of glucose, and at the anode, the glucose oxidation reaction occurs under the presence of oxygen. The inherent mixed nature of the two fuels glucose and oxygen requires that any implantable glucose fuel cell operates as a single chamber fuel cell. Multiple designs have been explored to operate glucose fuel cells in mixed fuel.

Selective Catalysis

One approach to generate an electrochemical potential in a mixed fuel is through selective catalysts using a single chamber fuel cell arrangement. In this configuration, the electrode catalysts show high selectivity toward one species (glucose or oxygen) under the presence of the other. Enzymatic glucose fuel cells typically rely on this approach, since enzymes such as glucose oxidase show near perfect selectivity: They have evolved over millions of years to specifically catalyze one reaction such as glucose oxidation, even in complex media like body fluids. However, enzymatic glucose fuel cell catalysts suffer from major drawbacks such as a short lifetime of typically less than 30 days, which is caused by enzyme and charge transfer degradation, and leaching of enzymes and mediators into aqueous solution.[27,28] In addition, charge transfer between enzymes and the catalyst support is generally difficult to achieve due to the complex nature of enzyme molecules.

Inspired by biological catalysts, there has been a push toward developing abiotic catalysts with high selectivity for the catalysis of the glucose oxidation and oxygen reduction reactions, respectively. The goal here is to achieve similar selectivity and activity as abiotic catalysts, while overcoming the stability and charge transfer challenges associated with enzymatic catalysts. Materials that have been explored as abiotic catalysts include noble metals, carbon, ceramic, and combinations thereof.[6] For example, Raney-type platinum and platinum alloys have been explored as selective catalysts for both the oxidation of glucose and the oxygen reduction reaction. The selectivity of the Raney-type system relies on the different rate-limiting steps of the two reactions.

Depletion Design

In the depletion design, one electrode is sealed off from direct contact with the fuel-containing liquid. By employing a selective catalyst at the fuel-facing electrode, one species is depleted at that electrode. This means that the concentration of that species is depleted at the other electrode, voiding the need for a selective catalyst at the buried electrode. The design is schematically depicted in **Figure 1.1 c.** For example, in the design presented by Rapoport et al., only the cathode is in direct contact with the fuel, whereas the anode is buried underneath the cathode and electrolyte membrane.[29] They employed single-walled carbon nanotubes as a selective catalyst for the oxygen reduction reaction, causing a depletion of oxygen at the cathode without affecting the concentration of glucose. Glucose can then migrate through the semi-

permeable membrane to reach the anode, where it is oxidized over a non-selective catalyst. By depleting the oxygen at the cathode side, this design effectively creates an oxygen-free fuel at the anode side of the fuel cell, which serves to build up the electrochemical potential driving the fuel cell.

This design constitutes a method of effectively creating a two-chamber fuel cell design, where the buried electrode effectively forms a second chamber with a different fuel composition than openly exposed electrode. However, the need for diffusion of one species through the fuel cell electrolyte to the buried electrode, and the required removal of reaction products from a buried electrode, pose significant challenges in the operation of such device. This is because the slow diffusion of reactants and products to and from the buried electrode creates a high overpotential under operation, thus lowering glucose fuel cell's power output.

Perm-selective Membranes

Perm-selective membranes can be employed to allow the selective passage of only one reactant to an electrode surface, thereby effectively creating a two-chamber fuel cell configuration. In this configuration, membranes are placed at one or both electrodes, which block off one species from reaching the electrode while the other species passes through. For example, a hydrophobic membrane can be employed at the cathode by allowing for gaseous oxygen to diffuse through the membrane while blocking the passage of glucose.[30] In a common embodiment of this design paradigm, the anode does not employ a selective membrane or a selective catalyst. Instead, the outer section of anode constitutes a sacrificial layer, where glucose and oxygen react with the goal to consume oxygen. Then in the inner region of the catalyst, oxygen is depleted and an electrochemical potential between the cathode and anode exists. Importantly, this operation principle only functions because the glucose concentration in body fluids is normally much higher than that of oxygen, meaning that oxygen depletion leaves residual glucose for the operation of the fuel cell.[6] A benefit of the perm-selective membrane design is that it does not require selective catalysts, which allows for the use of highly active, but unselective catalysts such as platinum.

1.1.4 Historical Development of Glucose Fuel Cells

The first report of an abiotically catalyzed glucose fuel cell was presented by Bockris *et al.* in 1964.[31] Bockris and co-workers researched the applicability of cellulose, glucose and other biotic carbohydrates towards fuel cells, and their fuel cell system relied on platinized platinum electrodes. During the same year, Yahiro *et al.* presented an enzymatically catalyzed glucose fuel cell proof-of-concept.[32] This enzymatic glucose fuel cell utilized glucose oxidase, as well as D-amino acid oxidase and yeast alcohol dehydrogenase to catalyze the anodic reaction in bio-fuel cell. The first abiotically catalyzed glucose fuel cell that was to

operate on glucose from body fluids was presented Warner and Robinson in 1967.[33] Already in this early study, a remarkably long fuel cell operation of 240 hours was reported. Only three years later, in 1970, the first reports of truly implanted abiotic glucose fuel cells were presented by Drake *et al.*[34] and Wolfson *et al.*[35]. These implanted glucose fuel cells were part of a larger push toward implantable power sources for pacemakers and artificial hearts, and were carried out by the American Hospital Supply Corporation and Michael Reese Hospital, respectively. The study by Drake and co-workers demonstrated a peak power density of 6.4 μW cm^{-2} and a power density of 2.2 μW cm^{-2} in continuous operation in an implanted glucose fuel cell tested for 30 days.[34] In 1973, Fishman and Henry presented a study on potentially implantable abiotic glucose fuel cells using noble metal alloy catalysts such as Au-Pd and Pt.[36] However, some of their electroplated catalyst alloys contain lead, a toxic heavy metal which makes the implantability of this system impossible. In particular, they report that the glucose selectivity stems from the presence of lead acetate in the electroplating bath. In addition, they observed unstable performance over time. During this first peak of research interest in implantable glucose fuel cells, the Artificial Heart Program of the United States National Heart, Lung, and Blood Institute was crucial at funding the development of glucose fuel cells as implantable power sources.[34,37] Besides these efforts in the United States, a team at Siemens was also active in the development of implantable glucose fuel cells. Rao *et al.* at Siemens presented a glucose fuel cell in 1973 in which a non-selective noble metal anode was sandwiched between two selective cathodes prepared from activated carbon.[38]

Despite these promising first development on glucose fuel cells, with the rise of the pacemaker battery invented by Greatbatch *et al.* in 1971[11], interest in the research and development of implantable glucose fuel cells rapidly declined. The pacemaker battery, a solid-state primary battery based on Li-I_2 chemistry, quickly became the predominant power source for implantable devices and remains the most prolific commercially used implantable power source to date. Despite its reliability, the pacemaker battery suffers from two key drawbacks, namely the limited degree to which it can be miniaturized and that it is a non-rechargeable primary cell, requiring risky replacement surgery whenever the energy stored in the battery is depleted. With a rising interest in highly miniaturized implantable electronics, and given the interest to overcome the need for replacement surgery, there has been a renewed interest in glucose fuel cells in recent years. This interest has driven research in both enzymatically catalyzed and abiotic glucose fuel cells.

Starting in 2010, a group of researchers around Kerzenmacher published a series of papers on a new type of abiotically catalyzed polymer-electrolyte glucose fuel cells.[39–42] These studies described abiotic selective catalysis of both oxygen reduction and glucose oxidation using Raney-type platinum catalysts, and assembled full depletion-layout fuel cells, using a polymeric polyethersulfone (Supor®-450) membrane. The assembled cell shows an open circuit voltage of 700 mV and a power density of 4.4 μW cm^{-2} under

simulated physiological conditions.[41] In the work published in 2011 by Kloke et al. from the same group, they transferred the previous results to an in-plane single-chamber fuel cell design where the two electrodes are located side-by-side. In this way they reached a power density of 2.2 μW cm^{-2}.[42]

In 2012, Rapoport et al. have described a fuel cell design which employs a fuel depletion design.[29] In their fuel cell system, a cathode made up of a mesh of single walled carbon nanotubes (CNTs) is surrounding a proton conducting polymer membrane and a Raney-type platinum anode, making use of the selectivity of CNTs towards to reduction of oxygen under the presence of glucose. The authors report a steady state power density of 3.4 μW cm^{-2}. This cell design was fabricated on a Si-chip, but employed Nafion as the electrolyte, making thermal sterilization difficult.

Oncescu and Erickson in 2013 reported on a thin film glucose fuel cell constructed in a concentric in-plane layout.[27] The demonstrated fuel cell's operation principle is based on the selective catalysis of the electrode reactions using Raney-type platinum alloys, namely Pt/Ni at the anode and Pt/Al at the cathode. Here it is noteworthy that the biocompatibility of Ni is questionable. The reported peak power density of the cell is 1.32 μW cm^{-2} for an individual cell and 2.01 μW cm^{-2} per cell when the cells are stacked. Two peculiarities are noteworthy in this design. Firstly, the electrode distance is 500 μm and therefore relatively large and secondly, the fuel cell employs a membraneless design. In this design, no dedicated electrolyte membrane separates the cathode and anode, and rather, the glucose fuel cell uses the fuel solution as the electrolyte. This design choice makes operation uncontrolled due to the complex nature of the body fluid fuel, which contains endogenous species that can interfere with the glucose fuel cell operation.

Besides these abiotic glucose fuel cell systems, there has also been renewed interest in enzymatic glucose fuel cells in recent years. Barton et al. thoroughly reviewed the field of enzymatic glucose fuel cells.[7] Most noteworthy, in 2011, Zebda et al. presented enzymatic glucose fuel cells with high power density of up to 1 mW cm^{-2} under physiological conditions and high open circuit voltage of 0.95 V.[43] However, these enzymatic glucose fuel cells raise concerns over lacking long-term stability and enzyme leaching under operation in aqueous milieu, which can be overcome with abiotic catalysts. Therefore, this thesis only considers abiotic glucose fuel cells as more attractive future power sources for implantable medical devices.

1.1.5 Physiological Operating Conditions for Implantable Glucose Fuel Cells

The physiological operating conditions for implantable glucose fuel cells are summarized in **Table 1.1**. The concentration of glucose varies by location in the body as well as with type of body fluid, which affects the conditions under which an implanted fuel cells operates. Physiological glucose concentrations range from 3.9 to 6.7 mM for blood,[44] 3 to 4 mM for interstitial fluid,[45] and 2.5 to 4.4 mM for cerebrospinal fluid.[46] The physiological oxygen concentration varies more widely in the body, due to physical activity, location,

and type of tissue. The usual range of oxygen concentration lies between 3 and 8 kPa, corresponding to a concentration of 0.02 to 0.06 mM.[6] Typically, studies of glucose fuel cells assume a 7% oxygen saturation at 37 °C, which corresponds to 0.06 mM. In addition, glucose fuel cells need to operate at body temperature, i.e. 37 °C.

Glucose Concentration	
Blood	3.9 – 6.7 mM [44]
Interstitial fluid	3 – 4 mM [45]
Cerebrospinal fluid	2.5 – 4.4 mM [46]
Oxygen Concentration	
Physiological range	0.02 – 0.06 mM [6]
Typical simulated condition	0.06 mM (7% saturation)
Operation Temperature	
Body temperature	37 °C

Table 1.1 Typical physiological operating conditions of glucose fuel cells

A critical aspect of the practical implantation and operation of a glucose fuel cell is the type of body fluid into which the fuel cell would be implanted, because the choice of body fluids defines the amount of other endogenous substances such as proteins, cells, or ions present, which could affect the operation of the glucose fuel cell. Various body fluids have been considered for the implantation and operation of glucose fuel cells, such as interstitial fluid[6], the bloodstream[6], tears[47], or cerebrospinal fluid[29]. These fluids all differ significantly in their composition, and a glucose fuel cell design should consider these physiological conditions for implantation. For implantable bio-electronics, the interstitial fluid is particularly promising as an implantation medium, since it contains significantly less immuno-active species than blood, while containing similar glucose and oxygen saturation levels.

In the design of implantable glucose fuel cells, first *in vitro* characterizations are usually performed in simulated physiological conditions. Here, phosphate-buffered saline solution (PBS) has become the medium of choice to simulate these conditions, since it provides a good replication of the ionic composition of body fluids, while increasing simplicity of operation due to the lack of biological species such as proteins or cells.[6]

1.2 Proton Conductivity in Solids

Proton transport and protonation in ceramic materials define and control the properties of materials that are used in a range of different application, from protonic ceramic fuel cells[48–50] and sensors[51–54] to resistive[55–59] and magnetic switches[60,61].

1.2.1 Overview of Solid-State Proton Conductors

Solid-state proton conductors play a critical role as electrolytes of different classes of fuel cells. Classifying these proton conductors by materials class usually goes hand in hand with characterizing them by the typical temperatures under which functional devices operate that employ these materials as electrolytes. **Figure 1.2** summarizes typical solid-state proton conductors and displays typical ranges of operation temperature, as well as features relevant for glucose fuel cell operation. Each operating temperature and material class comes with its own set of challenges and opportunities with regards to electrode reaction kinetics, proton conductivity, operating and infrastructure requirements, thermal management, and fuel selectivity. At the highest end of the temperature spectrum lie oxides of the perovskite structure, **Figure 1.2 a**, which are employed in protonic ceramic fuel cells (PCFCs). These perovskites, with the general formula of the form ABO_3 have been researched extensively with the goal to reduce the operating temperature of traditional, oxygen-ion conducting solid-oxide fuel cells (SOFCs), which routinely lie in the range of 800 – 1000 °C. Indeed, PCFCs have been successful to reduce the operating temperature of ceramic electrolyte fuel cells to 500 °C or less. The reason for this high proton conductivity at lower operation temperatures is the low activation energy for proton conduction in these proton conducting perovskite systems, which is typically between 0.3 eV and 0.6 eV.[62–65] The highest proton conductivities to date have been reported for doped barium zirconate, barium cerate, and solid solutions thereof.[49,50,63,66] In the context of hydrogen-powered fuel cells, PCFCs have the benefit of lowering the operating temperature significantly compared to traditional SOFCs, which means that gas sealings, enclosures, and all other fuel cell stack components are subject to significantly less rigid thermal conditions. This makes practical application simpler and thus cheaper, while still maintaining a high operating temperature at which the electrode reaction kinetics are sufficiently fast to allow for the use of non-noble metal catalysts.[50] However, these materials cannot be applied as glucose fuel cell electrolytes for implants due to the toxicity of materials such yttria-doped barium zirconate (BZY) and other proton-conducting perovskite oxides.[67]

Solid acids are a class of solid-state proton conductors that have been explored as intermediate-temperature fuel cell electrolytes in recent years, **Figure 1.2 b**.[68–70] An example of such a solid acid electrolyte is CsH_2PO_4, which exhibits anhydrous proton transport at temperatures above 230 °C due to a so-called superprotonic transition.[69] Hydrogen-powered fuel cells using solid acid electrolytes typically operate at

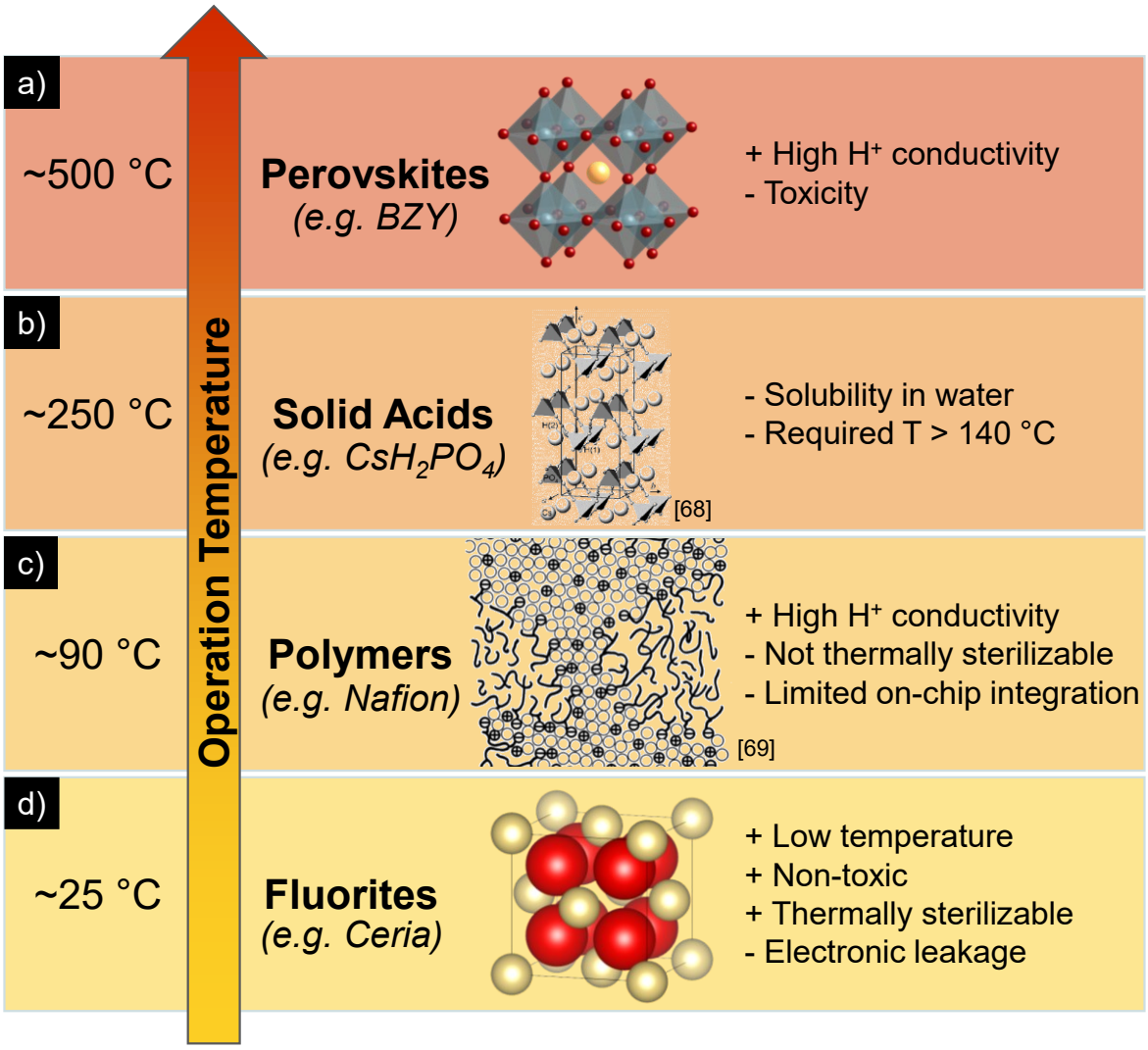

Figure 1.2 Solid-state proton conductors sorted by operating temperature. **a)** Perovskite oxides are frequently employed in protonic-ceramic fuel cells (PCFCs) with operating temperatures of ~500 °C, but their toxicity is prohibitive for implantable applications. **b)** Solid acids can be used as intermediate temperature fuel cell electrolytes, however, they are soluble in water. **c)** Proton exchange membranes such as Nafion are commonly used in fuel cells operating around 90 °C. They have good proton conductivity, but are not thermally sterilizable and limited in their miniaturization potential. d) Fluorites such as ceria conduct protons at temperatures as low as body temperature, and are non-toxic and thermally stable. They form a promising candidate material to be used as a ceramic electrolyte for implantable glucose fuel cells. Structures reproduced from [73,74].

temperatures around 250 °C, which constitutes another significant reduction of operating temperature compared to PCFCs. In addition, operation above the boiling point of water means that exhaust handling is simpler compared to low temperature fuel cells such as hydrogen-powered PEM fuel cells. However, when

considering solid-acid electrolytes for implantable glucose fuel cells, one recognizes that application here is infeasible for two main reasons: First, proton conductivity is too low below the superprotonic transition temperature, making operation at body temperature impossible; and secondly, solid acids are soluble in water, which is prohibitive for applications in aqueous media such as body fluids.

Proton-exchange membranes (PEM) such as Nafion are widely used polymeric proton conductors, that are commercially available in large scale and find applications in hydrogen-powered PEM fuel cells and PEM electrolyzers.[71] As such, PEMs allow for operating temperatures of hydrogen-powered fuel cells around 90 °C, just below the boiling point of water, **Figure 1.2 c**. This makes them the most widely used fuel cell technology to date, with applications in the automotive and stationary sectors. Nafion has a high ionic conductivity of up to 0.1 S cm^{-1} at body temperature[72], which is among the highest proton conductivity for low-temperature proton conductors known. However, despite this good performance, polymeric systems have three main drawbacks for implantation, in the context of implantable glucose fuel cells: Firstly, Nafion has lower limits of miniaturization due to concerns for fuel cross-over below a certain membrane thickness.[75] In particular, the thinnest commercially available type of Nafion, Nafion HP, has a thickness of 25 µm.[76] Secondly, Nafion cannot be easily integrated with semiconductor fabrication techniques, in particular vacuum-based techniques and processing at elevated temperatures, which limits how well it could be directly integrated into bioelectronic devices as the component of a power source. And finally, Nafion undergoes irreversible swelling[74] and conductivity reduction[77] at temperatures of 120 °C or more. This makes thermal sterilization impossible, which is commonly carried out at 121 ° C [78] and critical for implantation of biomedical implants.

Finally, low temperature ceramic proton conductors of the fluorite structure, **Figure 1.2 d**, such as ceria or yttria-stabilized zirconia (YSZ), have recently received increasing attention due to proton transport at temperatures as low as room temperature.[79–87] Such fluorite structure-type metal oxides typically show increasing proton conductivity with decreasing temperatures roughly below the boiling point of water, resulting in an apparent negative activation energy. This is because hydration and water adsorption increase with decreasing temperature, creating a higher charge carrier concentration. While fluorites have not been seriously considered for any hydrogen fuel cells due to the high performance of Nafion, they may offer significant advantages over polymers for implantable glucose fuel cell applications due to their ceramic nature: First, they can be easily thermally sterilized due to high temperature stability. Second, they can be processed using vacuum-based thin film deposition techniques, making them compatible with semi-conductor processing and on-chip integration for implantable bioelectronics. Third, they can be miniaturized to the nanoscale, putting unprecedented degrees of miniaturization in perspective.[88–90] Ceria is particularly promising in this regard, as it has been routinely fabricated as free-standing membranes on

silicon for solid-oxide fuel cells, an architecture that can potentially be expanded for glucose fuel cells. We therefore consider the proton conduction mechanism in ceria more detail in the following section.

1.2.2 Proton Conduction in Ceria – Mechanistic Insights

Ceria offers advantages over state-of-the-art polymeric proton exchange membranes (PEMs) for the integration into glucose fuel cells, due to it being non-toxic, easily thermally sterilizable, processable *via* standard semiconductor manufacturing techniques, mechanically and thermally stable. As a proton-conducting electrolyte, ceria has received interest in recent studies due to attractive levels of proton conduction at temperatures as low as room temperature. However, these investigations have mostly been limited to model systems such as thin films and pellets, and only one study so far has employed fluorites in a simple concentration-cell energy harvesting device.[91] Overall, these previous studies have contributed to understanding the mechanism of proton transport in ceria, but also left contradictions that require to be further elucidated to fully understand the proton conduction mechanism in ceria.

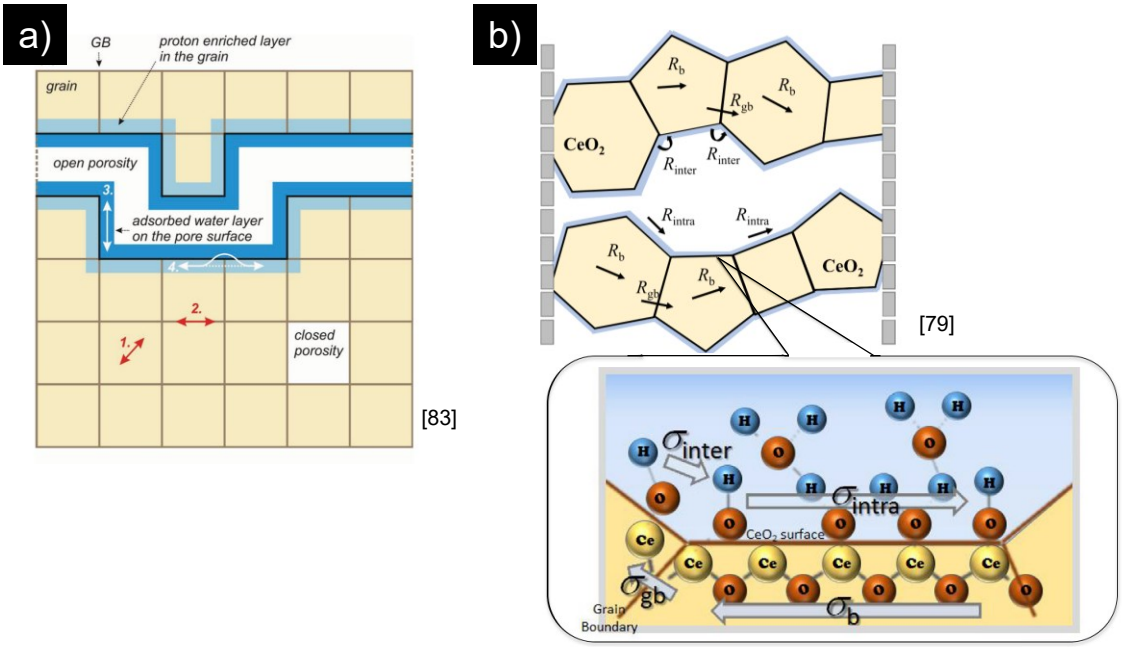

Figure 1.3 Models of proton transport modes in ceria. a) Gregori et al. propose that protons can be transported 1. through the grain, 2. along grain boundaries (denoted as GB) in the interior, 3. along an adsorbed water layer and/or 4. within an enriched water layer just below the surface.[83] b) Manabe et al. describe these same modes of proton transport, and in addition, suggest that the surface above a bulk grain (denoted as intra-grain transport above a single grain) and above a grain boundary (denoted as inter-grain transport between different grains) exhibit different proton transport resistances.[79] Both models suggest that proton transport in ceria is dominated by surface proton conduction.

The highest observed proton conduction in ceria was measured in gadolinia-doped ceria with conductivity of 10^{-3} S cm^{-1} at 25 °C[83], but even pure ceria exhibits a proton conductivity of up to $5 \cdot 10^{-4}$ S cm^{-1} at 25 °C[83]. Previous studies by Gregori et al.[83] in the Maier group and by Manabe et al.[79] in the Norby group have explored various transport pathways of proton transport in ceria at low temperatures, **Figure 1.3**.[79,83] Gregori et al. discuss the contributions of the grain bulk and interior grain boundaries, as well as two different surface water layers. They distinguish between an enriched water layer within grains immediately below the surface, and an adsorbed water layer on the surfaces within pores of the ceramic. This study concludes that surface transport dominates proton conduction, and that the interior contributions, namely grain bulk and interior grain boundaries, do not significantly contribute to proton transport. Importantly, they do not observe any cross-plane proton conductivity through dense ceria samples. Manabe et al. come to similar conclusions, however, they additionally distinguish between two separate regions of the surface-adsorbed water layer. They refer to the *intra grain* and *inter grain* regions of surface-adsorbed water, where *intra grain* refers to the water layer adsorbed above a bulk crystallite surface, and *inter grain* refers to the surface above a grain boundary. The study by Manabe et al. finds, through analysis of the electrochemical impedance of hydrated and dry ceria samples, that the intra and inter grain surface proton transport are predominantly for proton conduction in ceria.

In summary, both of these studies conclude that surface transport dominates the proton conduction of ceria. However, other reports on ceria as well as the very similar YSZ system present evidence that the interior of hydrated fluorites does in fact contribute to proton conduction, most notably reports from the Martin group.[85–87] These studies, carried out on dense pellets of nanocrystalline ceria and YSZ, reported enhanced proton conduction in moist air that showed strong dependence on the grain boundary density in these samples. Importantly, contrary to other studies, they observed bulk transport in YSZ, implying that grain boundaries contribute to proton conductivity in fluorites. Moreover, some experiments were carried out with a polymeric capping layer to prevent the formation of an adsorbed water layer on the YSZ surface.[87] Finally, the team around Martin have demonstrated simple electrochemical concentration cells using YSZ and samaria-doped ceria electrolytes, showing that such electrolytes can indeed be used in low-temperature energy harvesting devices.[91] Here, conduction again happened in a cross-plane configuration, providing further evidence of interior contributions.

Overall, these two contradicting findings show that there is still an ongoing debate on the exact proton conduction mechanism in ceria. In particular, the question remains unanswered why only some studies observed interior contributions to proton transport while other studies fully ruled out these interior contributions.

Besides the mechanistic classification of proton transport by different surface and interior contributions, proton conduction in ceria can also be classified by the mode how protons are transferred in the ceramic. Here, two mechanisms are generally regarded as the dominant proton transport modes: Firstly, a Grotthuss-type mechanism[92] where protons hop between water molecules in the water layer above the surface or between protonic defect sites within the ceramic bulk. Secondly, a vehicular mode where charge is transported through the drift of hydroxyl and hydronium ions.[79] This mode occurs only within a water layer at the surface of the ceramic.

Overall, understanding the mechanism of proton transport in ceria is important for the development of ceramic-electrolyte glucose fuel cells with ceria as the electrolyte material. By understanding the transport processes in the electrolyte, it is possible to engineer better electrolytes, and rationally design the electrolyte on the microscale to optimize overall device performance.

1.3 Open Research Questions

This thesis spans practical device development, electrochemical studies, as well as fundamental proton conductivity studies and materials processing work, with the goal to design, assemble, and understand the operation of first ceramic-electrolyte glucose fuel cells. Specifically, this thesis aims to answer the following open research questions:

- Can ceramic electrolytes be used to fabricate and operate glucose fuel cells for implantable applications?
- What are suitable fabrication routes and designs to produce such ceramic-electrolyte glucose fuel cells?
- What are the electrochemical operation principles of ceramic-electrolyte glucose fuel cells?
- What are suitable materials and design choices with regards to the layout, component material microstructure, electrical contacting, etc., for ceramic-electrolyte glucose fuel cells, and how would one design an electrochemical testing apparatus for such devices?
- Can inexpensive deposition techniques be employed in the fabrication of ceria as a ceramic proton-conducting electrolyte?
- What are the sources for the discrepancies in observed proton conduction mechanisms in ceria in the literature thus far?

- What role do thermal processing and thin film deposition parameters play in defining the structure, crystallinity, and proton conduction properties of ceria, in particular when deposited using wet-chemical synthesis methods?

1.4 Thesis Outline

The body of this thesis contains four main chapters addressing the open research questions outlined above. In **Chapter 2**, the first proof-of-concept of a ceramic-electrolyte glucose fuel cell is presented. Here, we demonstrate the first design, operation, and characterization of such an energy conversion device, including the open circuit voltage and power output. We demonstrate that on-chip ceramic-electrolyte glucose fuel cells exhibit sufficient performance to power miniaturized implantable medical devices, and provide first insights into the electrochemical operation principle of this new device class. After having delivered a proof-of-principle in the prior chapter, in **Chapter 3**, we discuss the design evolution and development of the previously presented ceramic-electrolyte glucose fuel cells in further detail. Here, materials selections, the development of a microfabrication route, and the design of dedicated testing apparatus is presented. **Chapter 4** addresses fundamental proton transport properties of cerium oxide, the proton-conducting electrolyte material studied throughout this thesis. In this chapter, we discuss how slow hydration kinetics affects the observation of apparent proton transport in ceria thin films based on a model system assembled through spray pyrolysis, and discuss present evidence for interior proton transport along grain boundaries within ceria. In **Chapter 5**, we present practical processing studies for the fabrication of ceria proton-conducting electrolytes via spray pyrolysis. In this chapter, deposition and thermal processing parameters of sprayed ceria thin films are systematically studied, with the goal to develop processing guidelines for the successful assembly of ceria electrolyte thin films through cost-effective wet-chemical fabrication methods. Additionally, we observe a so far unrevealed correlation between the Raman signature of ceria and its crystal texture, which could become useful as a cheap technique to explore crystal orientation for glucose fuel cells and other catalysis studies. The thesis closes with concluding remarks and an outlook on future directions, discussing next steps in the development of implantable ceramic-electrolyte micro glucose fuel cells.

2. Chapter 2: Ceramic-Electrolyte Glucose Fuel Cell for Implantable Electronics

Adapted from P. Simons, S. A. Schenk, M. A. Gysel, L. F. Olbrich, J. L. M. Rupp. Ceramic-Electrolyte Glucose Fuel Cell for Implantable Electronics. *Manuscript in revision (2021)*.

Chapter Abstract

Next-generation implantable devices such as sensors, drug delivery systems, and electroceuticals require efficient, reliable, and highly miniaturised power sources. Existing power sources such as the $Li–I_2$ pacemaker battery are limited in their scale-down potential without sacrificing capacity, and therefore, alternatives to power the next generation of implants are needed. In this work, we show that ceramic electrolytes can be employed in potentially implantable glucose fuel cells with unprecedented miniaturisation. Specifically, we demonstrate a ceramic glucose fuel cell based on the proton-conducting electrolyte ceria that is composed of a free-standing membrane of thickness below 400 nm and fully integrated into silicon for easy integration into bio-electronics. In contrast to polymeric proton-exchange membranes or separators, all the materials used are highly temperature stable, making thermal sterilisation for future implantation trivial. We demonstrate a peak power density of 43 $\mu W\ cm^{-2}$ for the ceramic-electrolyte glucose fuel cell as well as an unusually high statistical verification of successful fabrication and electrochemical function across 150 devices for open-circuit voltage and 12 devices for power density, enabled by a specifically designed testing apparatus and protocol. Our findings demonstrate that ceramic-based micro glucose fuel cells constitute the smallest potentially implantable power sources to date and are viable options to power the next generation of highly miniaturised implantable medical devices.

2.1 Introduction

Implantable medicine is undergoing a fundamental paradigm shift from passive to active implants such as electronic devices that sense and augment human health and body functions. These new biomedical implantable devices that are being developed, tested, and deployed range from drug delivery systems and sensors to electroceuticals and bioelectronic devices. In particular, electroceuticals and neurostimulation are a rapidly growing market with an annual growth rate of 8.5% and an estimated expected global market volume of US$ 41 billion in 2027[93], with global medical technology companies as well as start-ups seeking to commercialise technology[94,95]. To drive this revolution in implantable medicine, new power sources are required that can deliver safe and stable energy to implants while enabling the miniaturisation of these devices to an unprecedented scale to minimise the impact of implants on patients. Power requirements for implantable devices typically lie in the range of 100 nW to 1 mW[96–98], and power sources with increased energy and power density beyond current capabilities could enable new functionalities in sensing, electronic stimulation, or drug delivery that are currently unattainable.

To date, implantable devices are primarily powered by batteries such as the Li–I_2 pacemaker battery[10,11] with volumetric and gravimetric energy densities of ~1000 Wh l^{-1} and ~270 Wh kg^{-1} [12], respectively, or through wireless energy transmission such as RF transmission [13,14] or ultrasound[2]. Because of their nature, batteries cannot be easily miniaturised without sacrificing substantial energy storage capacity[99], and because power transferred via induction scales with the area of the antenna, the miniaturisation potential of wireless energy transfer is also limited. In addition, the Li–I_2 pacemaker battery is a non-rechargeable cell, which means that replacement surgery is required once the energy in the battery is depleted, creating a risk for complications. Because of these limitations, alternative implantable energy-harvesting solutions with the prospect of higher energy density and degree of miniaturisation are being researched, bringing glucose fuel cells[6,7,100] as well as thermoelectric[15,16], piezo-electric[19,20], and triboelectric generators[17,18] into focus.

Compared with batteries, glucose fuel cells allow for significant volumetric scale-down because they do not physically store energy in the chemical bonds of active electrode materials but instead directly convert fuel that is readily available inside the body into electrical energy. Considering also the practical implantation, glucose fuel cells can operate and harvest energy essentially anywhere in the body. For instance, polymer-electrolyte glucose fuel cells can utilise a wide range of body fluids such as interstitial fluid[6], the bloodstream[6], tears[47], or cerebrospinal fluid[29]. In contrast, thermoelectric generators require temperature gradients, which are very small inside the body, and piezo-electric and triboelectric generators require kinetic energy, which limits applicability to moving organs or body parts. Therefore, among these

alternative power sources, glucose fuel cells are particularly promising candidates for next-generation implantable power sources.

To put the development of glucose fuel cells into techno-historical context, **Figure 2.1 a** summarises the development of implantable power sources vs. key milestones of implant technology. Implantable power sources and implantable devices have continuously affected each other in their progress toward new treatments and device classes, and power sources have evolved with steady improvement of energy storage/conversion performance metrics and miniaturisation. In 1960, the first pacemaker, powered by a zinc mercuric oxide primary battery, was implanted into a human[21], and in addition to revolutionising the treatment of cardiac diseases, this invention galvanised the development of implant technology across all fields of medicine while also motivating research on new implantable power sources for these implant technologies. Only shortly after, in 1964, the first abiotic[31] and enzymatic[32] polymer-electrolyte glucose fuel cells were invented, which were motivated by the need to power new implant classes such as the pacemaker. However, when the Li–I_2 pacemaker battery was invented in 1971[11], this disruptive power source became the dominant source of energy for implantable devices, causing research into alternative implantable power sources to fall largely dormant for decades. During the 1980s and 90s, new treatments such as implantable drug delivery and neural stimulation evolved, and implant technology continued to follow macro-trends such as interfacing between the human body and electronic devices as well as steady miniaturisation. With the arrival of the 4th industrial revolution, the boundaries between the physical, digital, and biological world began to intersect, fusing new computing, sensing, and treatment capabilities. Here, a generation of new implantable device classes evolved, such as microchip-based drug delivery systems[101], deep-brain stimulators[102], and neural interfaces[103] that even evolved to so-called neural dust[2]. This latest push for miniaturised, integrated bio-electronics has recently reignited the need for new implantable power sources with higher energy density to minimise the space requirements of implants in patients. This includes the invention of new miniaturised power generators such as the piezo-electric nano generator[104] and the tribo-electric nano generator[105] over the last 15 years and has led to a renaissance of research in polymer-electrolyte glucose fuel cells for implantable applications.

For any implantable glucose fuel cell, a high degree of miniaturisation and good electrochemical conversion efficiency are desired. To achieve these objectives, implantable glucose fuel cells commonly employ one of two catalyst classes, namely enzymatic[100] or abiotic[6,8] catalysts. Enzymatic glucose fuel cells utilise enzymes such as glucose oxidase to catalyse the electrode reactions, whereas their abiotic counterparts use

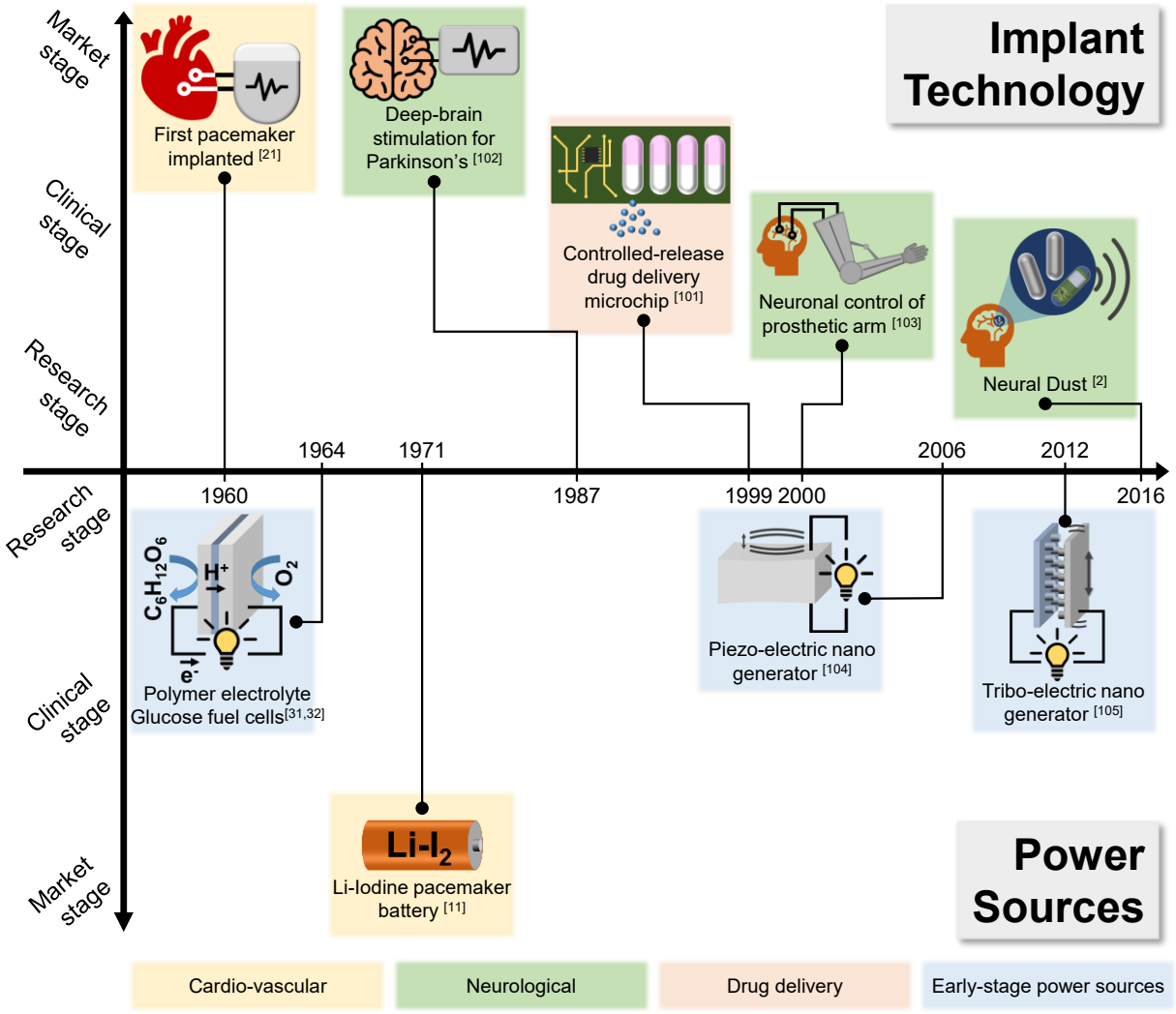

Figure 2.1 Techno-historical timeline of implant technology and implantable power source development. Implantable devices and their power sources have affected each other since the 1960s. The dominant implantable power source for most established, market-stage devices to date is the LiI_2 pacemaker battery, invented in 1971. Recent trends in implant technology include increased miniaturisation and neural interfacing, sparking a new push for highly miniaturised, long-term-stable implantable power sources. New power sources, e.g., tribo-electric and piezo-electric nano generators, aim to combine efficient energy harvesting with on-chip integration to meet the requirements of new, miniaturised implantable devices.[2,11,21,31,32,101–105]

non-biological materials such as noble metals, alloys, carbon, or composites thereof to catalyse the anodic and cathodic reactions. Enzymes exhibit very high catalytic selectivity; however, their lifetime is typically less than 30 days due to enzyme and charge-transfer degradation as well as leaching of enzymes and mediators into aqueous solution.[27,28] Abiotic glucose fuel cells, on the other hand, promise higher long-term stability and faster charge transfer than enzymatic glucose fuel cells because abiotic catalysts do not

face rapid degradation or charge-transfer limitations. To date, glucose fuel cells typically rely on polymer-based proton-exchange membranes as the electrolyte or make use of the electrolytic properties of the medium into which they are implanted (*e.g.*, blood, interstitial fluid, cerebrospinal fluid) in a so-called membraneless configuration. Proton-exchange membranes (*e.g.*, Nafion, PVA–PAA) are well researched polymeric ion conductors with high ionic conductivities of up to 0.1 S cm^{-1} at body temperature for Nafion.[72] Despite this good conductivity, polymer-electrolyte glucose fuel cells exhibit several drawbacks as implantable power sources related to the polymer nature of the electrolyte:

i. Natural limitation for further miniaturisation and increase of energy density: To avoid fuel cross-over[75], commercial Nafion membranes require a minimum thickness of at least 25 μm (exemplified by Nafion HP[76], the thinnest commercially available type), which creates a lower limit for miniaturisation.

ii. Challenge to integrate with silicon-based chip design and microfabrication: Recent developments in integrated electronics for biomedical applications, such as microchip drug delivery systems[101], show that direct on-chip silicon integration of the power source can drive further miniaturisation and efficiency of implantable bio-electronics. The current materials for glucose fuel cells, using polymer-based electrolytes, are not easily integrated with semiconductor manufacturing processes, making on-chip integration for such implant applications difficult.

iii. Inability for thermal sterilisation: A common procedure to sterilise implants during an implantation process is to apply moist heat sterilisation. Although Nafion has a high thermal stability up to 280 °C[106], exposure to temperatures of 120 °C or more causes irreversible damage to the material, including irreversible swelling[74] and conductivity reduction[77], damaging both the mechanical stability and electrochemical performance of the device. These effects make moist heat sterilisation, a critical step for implantation that is commonly performed at 121 °C or 132 °C [78], impossible.

These challenges of miniaturisation, silicon on-chip integration, and thermal sterilisation of current polymer-based glucose fuel-cell types may be overcome by moving away from polymer electrolytes and, instead, developing glucose fuel cells that operate on ceramic proton-conducting electrolytes.

Ceramic materials have a long history of use as electrolytes in solid oxide fuel cells (SOFCs)[107–110] and protonic ceramic fuel cells (PCFCs)[48–50,111,112] operating on hydrogen and exhibit higher thermal, chemical, and mechanical stability than polymer electrolytes such as Nafion. However, although a wide range of proton-conducting ceramics are being researched for hydrogen PCFCs, they have not yet been considered for glucose fuel cells. Consequently, the material selection, electrochemical operation principle, and even basic proof of operation of a ceramic glucose fuel cell all remain unexplored. To select the electrolyte material for such a ceramic glucose fuel cell for implantable applications, the most fundamental criterion

is that the proton-conducting ceramic must be biocompatible. This criterion excludes many of the best-performing proton-conducting ceramics such as yttria-doped barium zirconate (BZY)[49,63,66] and other solid solutions of barium zirconate and barium cerate because of their toxicity[67]. In contrast, low-temperature proton conductors such as ceria[113] or yttria-stabilised zirconia (YSZ)[114] are non-toxic and biocompatible; in addition, they are stable up to temperatures far in excess of 1000 °C, making thermal sterilisation trivial. The proton conductivity of hydrated ceria, CeO_2, reaches up to 10^{-3} S cm^{-1} at room temperature[79,82–84], which is sufficient to enable the operation of energy-conversion devices at body temperature. Furthermore, ceria is known to exhibit enzyme-like properties when structured as nanoparticles and is being actively researched for oncology applications.[113,115]

Ceria as a ceramic proton-conducting electrolyte offers a pathway to miniaturisation that is particularly appealing for implantable micro-devices. Ceria and its solid solutions were among the first materials to be integrated as oxygen-ion-conducting electrolytes into micro-solid oxide fuel cells with electrolyte thicknesses scaled down to hundreds of nanometres and integrated on silicon chips.[90,107] A transfer of this technology towards glucose fuel cells can enable the realisation of glucose fuel-cell devices that are fully integrated on silicon with high volumetric power density given the device thickness of only a few hundreds of nanometres. This miniaturisation, in combination with the thermal and mechanical robustness of ceria, opens scale-down opportunities on the sub-micron scale previously inaccessible to polymer-electrolyte glucose fuel cells.

There have been no reports of ceramic-based glucose fuel cells to date, and therefore, the electrochemistry as well as potential designs, material selection, and operating principles of such devices for future implants are also unexplored. Thus, demonstrating a first design of a ceramic-based abiotic glucose fuel cell not only opens up a potential new class of power sources for future implantable devices but also paves the way to overcome the limitations of existing polymer-based glucose fuel cells through miniaturisation, on-chip integration, and the ability for thermal sterilisation. Ultimately, this is a step toward enabling fully integrated and miniaturised implants, following the fast-paced evolution of microchip devices such as drug delivery systems and neural dust as well as toward future electroceuticals and miniature bio-electronics. In this work, we present a glucose fuel cell that is fabricated entirely from solid-state materials, such as ceramics and noble metals. The use of ceria as the ceramic proton-conducting electrolyte overcomes many of the shortcomings of polymer-based electrolytes, and the entire glucose fuel cell is fabricated on a silicon chip using standard semiconductor microfabrication techniques, which means that the fuel cell can be easily and directly integrated into bio-electronic devices and implants. We demonstrate the principle and operation of the ceramic-based miniaturised glucose fuel cell and explore the operating mechanism and electrochemical processes for glucose conversion. Eventually, our findings could guide efforts towards new

power source alternatives for implants particularly suited for a high degree of miniaturisation and on-chip integration beyond batteries.

2.2 Results and Discussion

A promising strategy to develop glucose fuel cells with on-chip integration is to design a manufacturing route based on thin-film technology. We select CeO_2 as the proton-conducting electrolyte and platinum films as the electrodes, serving both as catalysts and current collectors. The proton-conducting ceria was fabricated as free-standing fuel-cell membranes on a silicon chip, and optimal processing conditions were determined to establish a proof of concept for a ceramic glucose micro-fuel cell and characterise its electrochemistry and performance.

2.2.1 Ceramic-based glucose fuel cell design and electrochemical operational principle

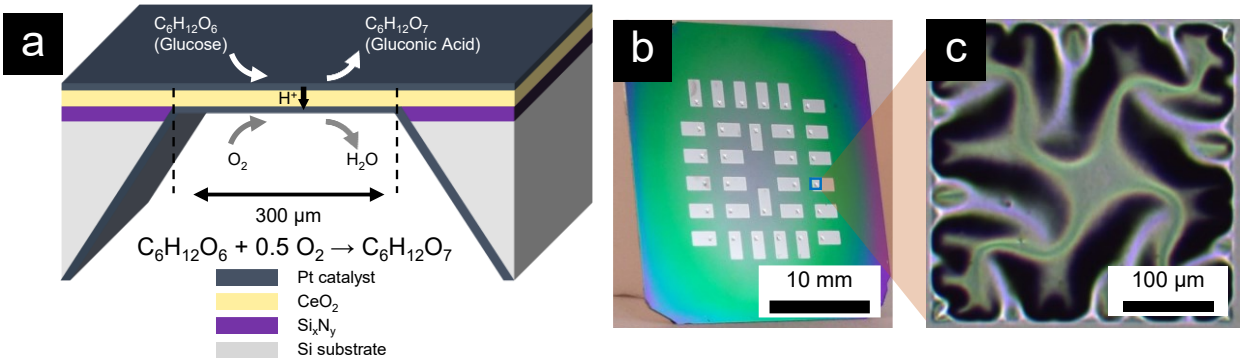

Figure 2.2 Schematic of glucose fuel cell, chip and individual device. a) Schematic of a ceramic glucose fuel cell based on a free-standing membrane of a porous Pt anode / CeO_2 electrolyte / dense Pt cathode. **b)** Optical photograph of fuel-cell chip containing 30 individual glucose fuel-cell devices. **c)** Optical microscopy image of an individual free-standing ceria membrane.

The design of this ceramic-based glucose fuel cell consists of a proton-conducting electrolyte, ceria, and porous platinum electrode films for the conversion of glucose and oxygen, respectively. For the proof-of-concept, we designed the glucose fuel cell in a two-chamber operation architecture, which enabled the separation of glucose and oxygen at the two electrode sides, see **Figure 2.2 a**. This architecture is well suited for the proof-of-concept of the reaction chemistry at both electrodes. A key challenge in the design and fabrication of such micro glucose fuel cells based on ceramics is to create crack-free, self-supported free-standing membrane systems consisting of a Pt anode / CeO_2 electrolyte / Pt cathode at length scales on the order of only a few hundred nanometres. We demonstrate the successful fabrication of 30 individual crack-free glucose fuel cells on a silicon chip, **Figure 2.2 b and 2.2 c**, throughout 5 different glucose fuel cells, resulting in 150 visually intact glucose fuel cells. Each glucose fuel cell was less than 370 ± 40 nm thin and measured 300 µm × 300 µm in area. Given the degree of miniaturisation of the electrolyte, these

ceramic glucose fuel cells were two-orders-of-magnitude thinner than commercial Nafion, directly translating into a smaller device footprint for future patients.

For actual implantation, these glucose fuel cells would operate under physiological levels of glucose concentration, which varies by location and body fluid, ranging from 3.9 to 6.7 mM for blood[44], 3 to 4 mM for interstitial fluid[45], and 2.5 to 4.4 mM for cerebrospinal fluid [46]. The electrochemical operation principle of the ceramic micro glucose fuel cell is such that at the anode, glucose ($C_6H_{12}O_6$) is oxidised to form gluconic acid ($C_6H_{12}O_7$) and thereby releases protons and electrons in the anodic reaction step:

Anode reaction: $$C_6H_{12}O_6 + H_2O \rightarrow C_6H_{12}O_7 + 2H^+ + 2e^- \quad \text{(Eq. 1)}$$

The protons then travel through the proton-conducting electrolyte and reach the cathode, where they react with oxygen and electrons in the cathodic reaction step to form water:

Cathode reaction: $$\frac{1}{2}O_2 + 2H^+ + 2e^- \rightarrow H_2O \quad \text{(Eq. 2)}$$

The overall electrochemical reaction of the glucose fuel cell is given by

Glucose fuel cell reaction: $$C_6H_{12}O_6 + \frac{1}{2}O_2 \rightarrow C_6H_{12}O_7 \quad \text{(Eq. 3)}$$

The electrons travel through an external circuit between the anode and cathode and can thereby power an implantable device. The Gibbs free energy of the overall glucose fuel-cell reaction (Eq. 3), *i.e.,* the reaction of glucose with oxygen to form gluconic acid, is $\Delta G^0 = -2.51 \cdot 10^5$ J/mol, which results in an equilibrium Nernst potential of $U^0 = 1.08$ V[116].

2.2.2 Designing ceramic glucose fuel-cell functional components with high degree of miniaturisation

To successfully assemble the ceramic glucose fuel cell on silicon and operate it in liquid glucose solution, it is necessary to balance a range of properties including high mechanical stability, low chemical cross-talk between electrodes, high proton conductivity of the electrolyte, and high catalytic activity of the electrodes. All these properties need to be optimised to achieve operation under a potential as close as possible to the theoretical Nernst potential of the fuel cell. To balance these requirements at the electrolyte component, we fabricated two different microstructures of the ceria solid proton-conducting electrolyte: a dense, columnar

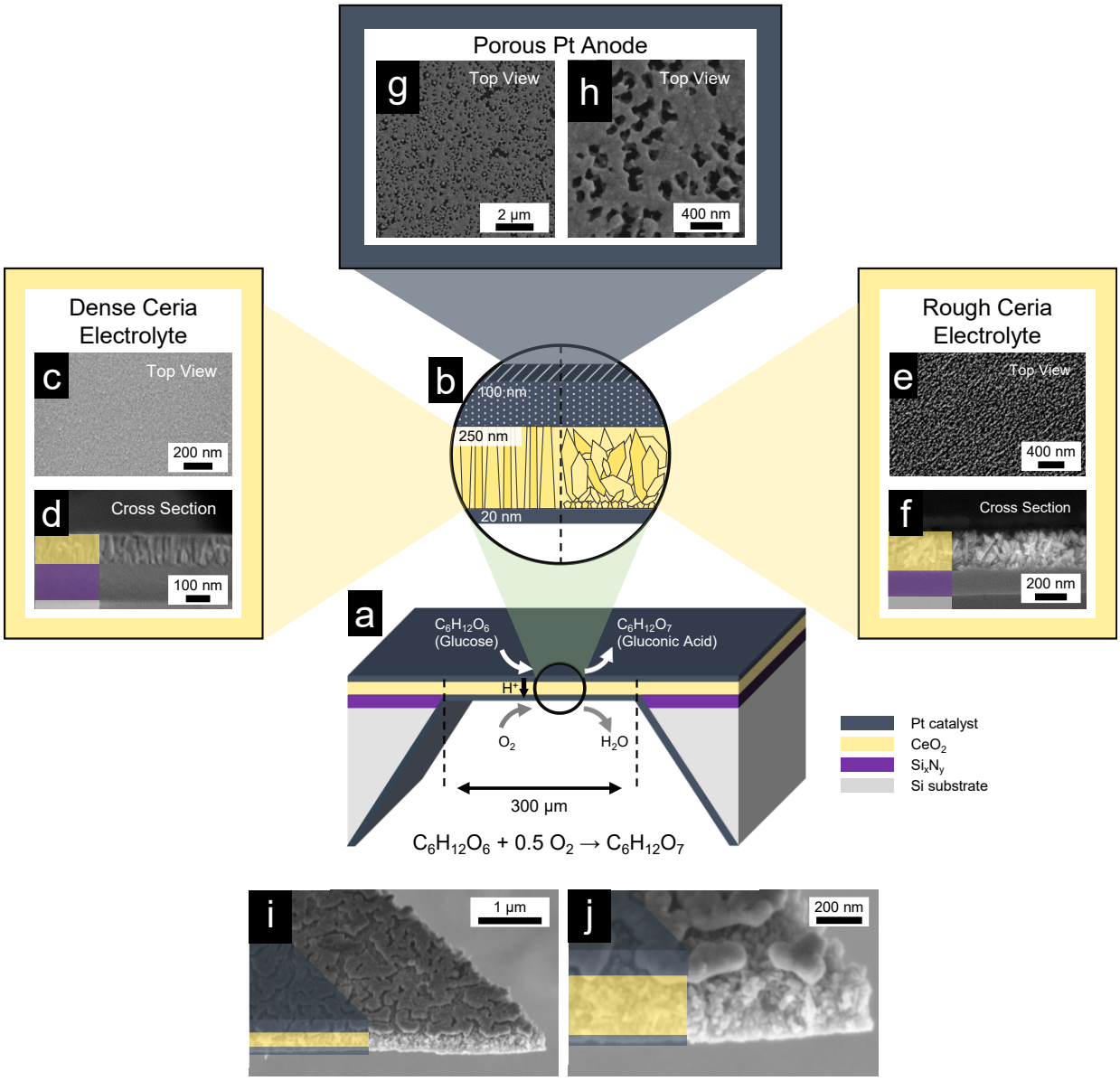

Figure 2.3 Schematic of ceramic glucose fuel cell and SEM analysis of its components. a,b) Schematic of ceramic glucose fuel cell consisting of free-standing ceria membrane as the proton-conducting electrolyte, a porous Pt anode, and a dense Pt cathode. **b)** Two different microstructures of the ceria electrolyte were employed, namely a dense, columnar microstructure (left) and a rough, cauliflower-like microstructure (right). **c, d)** Top-view **(c)** and cross-sectional view **(d)** SEM micrographs of the dense ceria electrolyte microstructure. **e, f)** Top-view **(e)** and cross-sectional view **(f)** SEM micrographs of the rough ceria electrolyte microstructure. **g, h)** SEM images of different magnifications of the porous Pt anode. **i, j)** Cross-sectional SEM images at different magnifications of a full glucose fuel cell, measuring 370 nm in thickness and consisting of a porous Pt anode (top), rough ceria ceramic proton-conducting electrolyte (middle), and dense Pt cathode (bottom).

microstructure, depicted schematically in the left half of **Figure 2.3 b** and in SEM micrographs in **Figure 2.3 c and 2.3 d**, and a cauliflower-like rough microstructure, depicted schematically in the right half of **Figure 2.3 a** and in SEM micrographs in **Figure 2.3 e and 2.3 f**.

The dense, columnar microstructure resembles that typically used in micro SOFCs[90] and prioritizes the blocking of chemical cross-talk between the electrodes. The SEM micrographs confirm the successful growth of dense, columnar ceria, both in the top view, **Figure 2.3 c**, and cross-sectional view, **Figure 2.3 d**. The diameter of these columnar grains lies between 10 and 50 nm, as seen in the SEM micrograph. The rough microstructure serves two main purposes. First, this rough microstructure is designed to enhance the overall proton conductivity of the electrolyte through the rough, high-surface-area configuration of ceria, allowing water to fill the open porosity. This design was based on earlier findings that proton conduction in ceria is enhanced along the surface of hydrated ceria[79]. Second, this rough microstructure reduces the mechanical stress state in the fuel-cell membrane compared with that in fully dense films, increasing the mechanical stability and robustness of the fabrication process (see Supporting Information, S2). The rough microstructure is designed such that at the bottom, the film is dense with a base thickness of approximately 20 nm, and above this fully dense microstructure region, it exhibits a disordered, cauliflower-like microstructure; see schematic and SEM image in **Figure 2.3 b and 2.3 f**. Similar to the fully dense electrolyte configuration, the dense section of the rough-electrolyte configuration serves as a blocking layer for the liquid glucose-containing fuel to avoid any chemical or ionic short-circuiting through water. Overall, the rough ceria electrolyte microstructure has a relatively short dense microstructural cross-section, with the goal being to increase the overall effective proton conductivity as well as to increase the protonic transference number of the electrolyte. The overall rough and disordered microstructure can be seen in both the surface and top-view SEM micrographs, **Figure 2.3 e and f**. The grain size varies strongly throughout the disordered ceria film, with approximate grain sizes between 1 and 50 nm, and the RMS surface roughness was estimated to be 30 nm from the SEM micrographs. To control the microstructure of the ceria electrolyte, we selected suitable pulsed laser deposition (PLD) parameters based on earlier findings that below a critical deposition pressure of ~0.05 mbar, ceria thin films deposited via PLD are fully dense, whereas above this pressure, they exhibit a rough microstructure[117]. The PLD depositions were optimised to achieve the desired microstructures on substrate-supported samples before fabrication of full glucose fuel-cell devices. The cubic fluorite structure of the ceria proton-conducting electrolyte was confirmed by XRD and Raman spectroscopy analyses, as discussed in more detail in the supplementary information, and is in good agreement with the literature[118].

The electrode was designed to achieve high catalytic activity and selectivity. The anode, being the top electrode of the glucose fuel cell, was fabricated as a layer of nano-porous platinum with a thickness of 100

nm. Porous platinum was selected as the anode catalyst because Raney-type nano-porous platinum is known to be a selective catalyst for the oxidation of glucose in the presence of oxygen.[39,40] We developed a reactive-sputtering fabrication route to obtain de-alloyed porous platinum rather than using the Raney-type route used previously for polymeric glucose fuel cells that relies on chemical etching. The reactive sputtering route was selected because it is a mechanically robust process without harsh chemical etchants. This fabrication route was adapted from Jung et al.[119], and it does not require a chemically aggressive wet-etching step, making it compatible with ceria[120,121] and a wide range of other ceramic and CMOS materials and deposition techniques. **Figures 2.3 g** and 2.**3 h** present SEM micrographs of the Pt anode at different magnifications. The Pt electrode was nano-porous, with a typical pore diameter of approximately 100 nm. The anode, *i.e.,* the bottom electrode of the glucose fuel-cell design, consisted of a dense layer of Pt serving as the catalyst for the oxygen reduction reaction (ORR). The ORR is diffusion limited, whereas glucose oxidation is kinetically *i.e.,* surface limited, and thus, the low-surface-area, dense Pt film at the cathode forms a selective ORR catalyst in the presence of glucose[23]. Overall, the microstructures of both electrodes were designed to enable selective catalysis of the electrode reactions, *i.e.,* glucose oxidation and oxygen reduction, respectively.

To further clarify the microstructure and full assembly of the full ceramic glucose fuel-cell system, **Figures 2.3 i and 2.3 j** present post-mortem SEM micrographs of a fractured fuel-cell free-standing membrane with a porous Pt top electrode, rough ceria electrolyte, and dense Pt bottom electrode. The full fuel-cell device with its functional components and a total device thickness of only 370 nm is shown. The full-device microfabrication route for the free-standing glucose fuel-cell membrane devices consisted of a series of microfabrication steps involving photolithography, wet and dry etching, and thin-film deposition techniques. The process is described in detail in the methods section and is schematically summarised in the supplementary information (Supporting Information S3). All the processing steps were optimised to achieve a fabrication yield of 100% over 150 individual glucose fuel-cell membranes, *i.e.,* 30 membranes each on 5 separate silicon chips.

2.2.3 Overall cell resistance and electrolyte conductivity via electrochemical impedance spectroscopy

Next, we analyse the electrochemical impedance of the glucose fuel cell to gain insight into the different contributions to resistance in the glucose fuel-cell system. Electrochemical impedance spectroscopy was used to understand the sources of loss in the ceramic glucose fuel cell. We discuss here the exemplary case of the rough ceria electrolyte; however, the results are representative for both microstructures. **Figure 2.4 a** presents the impedance spectrum of a glucose fuel cell with a rough microstructure taken at 23.5 °C. The

entire chip was exposed to humidified air to hydrate the electrolyte. Measurements under liquid water were not possible because of the large artefacts of the water in the impedance spectra. The impedance spectrum, displayed as a Nyquist plot, contains 2 arcs with peak frequencies of 0.13 and 56 Hz. The two arcs are qualitatively consistent with the behaviour observed for surface-limited proton conduction in porous ceria pellets,[79] which is remarkable because part of the proton transport occurred through the dense lower fraction of the ceria membrane and not along the surfaces of pores. However, the total conductivity of $5.4 \cdot 10^{-10}$ S cm^{-1} is four-orders-of-magnitude lower than that commonly observed in surface-governed proton transport.[79,85] This difference can be explained by two factors that reduce the total conductivity. First, cross-plane proton transport through dense ceria has a higher resistance than the in-plane surface transport described by Manabe et al.[79]; in fact, in some studies, no interior contribution to proton conductivity was observed at all.[83] Second, the conductivity reported is of an entire glucose fuel-cell device, *i.e.,* including the top and bottom electrodes and their interfaces with the ceria electrolyte. A more detailed discussion of the impedance spectrum can be found in the supplementary information. In summary, we view this total device impedance as sufficiently low, and thus the conductivity as sufficiently high, to successfully operate as glucose fuel cells.

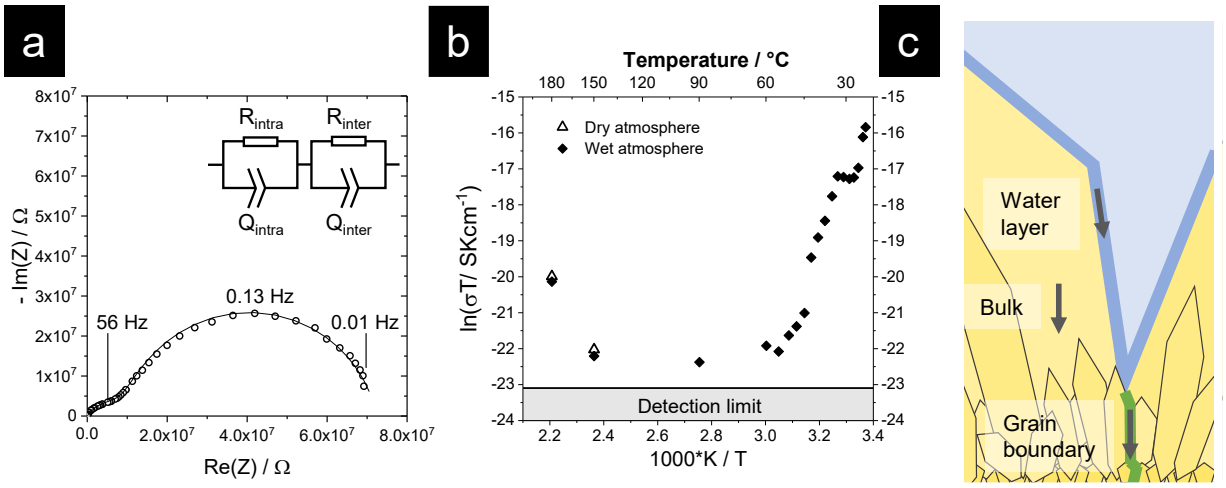

Figure 2.4 Impedance and proton conductivity of glucose fuel-cell devices. a) Impedance spectrum and equivalent circuit for a glucose fuel-cell membrane at 23.5 °C. **b)** Arrhenius-type plot of conductivity of the fuel-cell system extracted from EIS measurements, proving protonic conductivity at low temperatures in the hydrated case. **c)** Mechanism of proton conductivity through the rough ceria electrolyte structure.

To further investigate the mechanism of conductivity and confirm that the observed total conductivity is in fact of protonic nature, we measured the fuel-cell impedance under wet and dry conditions and various temperatures. Conforming proton conduction and determining the device conductivity defines the electrochemical conversion efficiency and, therefore, the total power output of the ceramic glucose fuel cell. **Figure 2.4 b** displays the total conductivity of the glucose fuel-cell system with a rough electrolyte in the form of an Arrhenius-type plot under dry and humidified air. The conductivity was determined from impedance spectra measured between 22 °C and 180 °C for full glucose fuel cells. In the dry case, the conductivity dropped below the detection limit of the instrument below 150 °C. In contrast, for humidified air, an inflection in the conductivity was observed near 100 °C, the boiling point of water, and conductivity increased with decreasing temperature. This behaviour of an apparent negative activation energy at low temperatures is typical for proton conduction in hydrated oxides such as ceria[82,84,122] and stems from the competition of thermally activated ion hopping and higher water coverage at lower temperatures. We thus confirm that proton conduction was observed and, importantly, that this occurs in a cross-plan configuration, *i.e.*, through a dense electrolyte layer of ceria. For the rough electrolyte configuration, the vast majority of the protonic pathway through the electrolyte was governed by rough, high-surface-area ceria, as schematically depicted in **Figure 2.4 c**. The water layer adsorbed to the columnar grain surface serves as a high-proton-conduction channel, with intra- and inter-grain-boundary proton conduction controlling the conductivity behaviour in this region. In the bottom fraction of the electrolyte, with a thickness of roughly 20 nm, conduction occurred through dense, nano-granular ceria. Overall, we confirm proton conduction in both the rough and dense ceria microstructures of the ceria proton-conducting ceramic electrolyte, a necessary condition to operate glucose fuel cells. Based on the demonstrated proton conduction, we turned to further characterising the function of fabricated fuel-cell devices based on both the rough and the dense electrolyte microstructures.

2.2.4 OCV statistics of 150 ceramic glucose fuel cells and power generation performance via IV curves

We now turn to electrochemical metrics of device operation to characterise the operation of glucose fuel cells *in vitro*. To deliver a reliable proof of concept and answer the question with sufficient statistical evidence of whether a glucose fuel cell based on a ceramic proton conductor can operate, we measured the open-circuit voltage (OCV) of a total of 150 micro fuel-cell devices under deaerated 0.5 M glucose solution in phosphate-buffered saline (PBS) solution at the anode and under air at the cathode. Among both polymeric glucose fuel cells and hydrogen-based ceramic micro fuel cells, this number of tested prototypes is among the highest ever reported. This large number of characterised devices was achieved by constructing a dedicated, custom-built testing setup that allows for rapid switching between individual

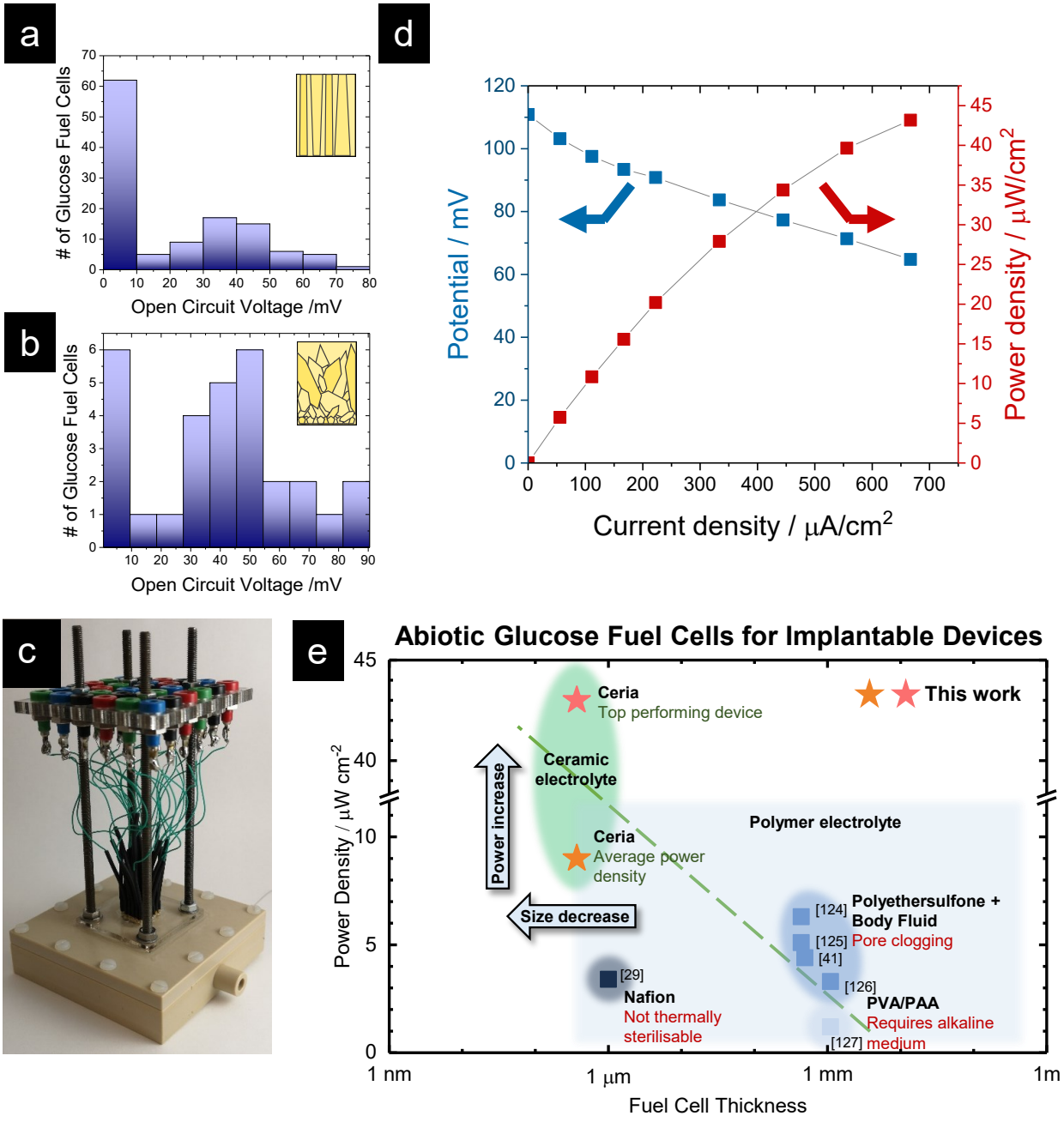

Figure 2.5 Performance and comparison of ceramic glucose fuel cells. a, b) Histograms of the open-circuit potentials of **(a)** 120 ceramic glucose fuel cells with dense ceria electrolyte and **(b)** 30 ceramic glucose fuel cells with porous ceria electrolyte. **c)** Test setup allowing for rapid screening of 30 individual glucose fuel-cell devices through spring-loaded needles and plug board. **d)** Polarisation curve of a ceramic glucose fuel cell, exhibiting a peak power density of 43 µW cm^{-2}. **e)** Comparison of previously reported polymer-electrolyte-based glucose fuel cells with those in this work, *i.e.,* ceramic-electrolyte glucose fuel cells: power density as a function of fuel-cell thickness. The ceramic glucose fuel cells show 3 times higher miniaturisation and higher power densities than existing abiotic glucose fuel cells.[29,41,123–126]

glucose fuel-cell devices placed on silicon chips, which formed an important basis for this work. Among the 150 glucose fuel cells measured, 120 exhibited the dense, columnar ceria electrolyte microstructure and 30 exhibited the rough electrolyte microstructure, in accordance with **Figure 2.3**. **Figure 2.5 a and 2.5 b** present histograms of the OCVs of ceramic glucose fuel-cell devices with dense and porous electrolyte microstructures, respectively. **Figure 2.5 c** displays the apparatus used to measure the OCV of the 30 individual glucose fuel cells in rapid sequence. The mean OCV of all the functioning fuel cells was 38.5 mV, with the rough-microstructure devices exhibiting a higher mean OCV of 44.7 mV, **Figure 2.5 b**, than the dense membranes, which had a mean OCV of 34.5 mV, **Figure 2.5 b**. In addition, the ratio of functioning devices for visually intact fuel-cell membranes was four-times higher for the devices with the rough electrolyte microstructure (24 out of 30 devices functioning) than for the dense ones (60 out of 120 devices functioning). Here, we define a functioning device as a device with a non-zero OCV. These results indicate that the rough microstructure reduces sources of lowered electrochemical potential as well as the total device failure rate. Sources for a reduced OCV can be electronic leakage through the ceria electrolyte, as dry (*i.e.,* unprotonated) ceria with nano-sized grains is a predominantly electronic conductor,[127] and it can be expected that some residual electronic conductivity is present in the hydrated case as well. In addition, the rough microstructure exhibits significantly lower stress (see supplemental information for optical micrographs of buckling patterns), which reduces the chance of crack or pin-hole formation[107] due to stress relief and, thus, the amount of electrode cross-talk. Finally, for the rough microstructure, we expected pin-holes and nanoscale flaws to be more readily closed during the deposition process given the high degree of disorder in the thin film. However, no pin-holes were visible using backlight microscopy in any of the devices with either microstructure tested here, and SEM could not be used for pin-hole analysis given the fragile nature of the glucose fuel cells when drawing a vacuum. In total, 84 out of 150 glucose fuel cells were operational by exhibiting non-zero OCV, and we turn to cell testing of the total power output of a subset of these devices in the next step.

The power output performance of the glucose fuel cells with both rough and dense electrolyte microstructures were then characterised by measuring the current–voltage profiles under 0.5 M glucose solution in PBS at the anode and air at the cathode. In total, 12 separate glucose fuel cells were measured (2 with rough electrolyte microstructure and 10 with dense electrolyte microstructure), with four voltage sweeps performed sequentially, over the course of up to 11 h per fuel cell. **Figure 2.5 d** displays an example of a high-performing glucose fuel cell, which exhibited a peak power density of 43 $\mu W\ cm^{-2}$. We have recently shown that ceria exhibits slow hydration kinetics at room temperature[122]; therefore, careful equilibration is more important for ceria-based glucose fuel cells than for other systems such as Nafion-based glucose fuel cells. To balance the hydration kinetics considerations with surface degradation, measurements were taken after equilibration with pure water and then glucose solution for 12 h each. After

this equilibration, the OCV of the particular device shown in **Figure 2.5 d**, which had a dense ceria electrolyte microstructure, still increased over time despite equilibration over 24 h prior to the first measurement. This slow equilibration is important to consider for future implantation, as it implies that the device must be either pre-conditioned prior to implantation or will exhibit a transient time after initial implantation. Overall, the average peak power of all the measured devices was 9 μW cm^{-2}, indicating that the overall glucose fuel-cell performance is competitive with that of other abiotic glucose fuel cells and that the power density reaches values that are relevant for miniaturised implantable devices, **Figure 2.5 e**.

To use ceramic glucose fuel cells to power implantable biomedical devices, long-term stability is required to power devices such as sensors or neural stimulators. Therefore, it is worth emphasizing that the measurements of the IV curves were obtained over the course of up to 11 h each, and multiple devices on the same chip were measured successfully, meaning that glucose fuel cells were exposed to glucose solution and characterised for up to 140 h. This observation is the first promising indication of the long-term stability of the solid-state micro glucose fuel cells. After the longest measurement campaign of 140 h, we observed the formation of precipitates at the surface of the glucose fuel-cell chip (see supplemental information S5). These precipitates were organic salts, which likely formed from side reactions between glucose and dissolved species from the PBS.

In conclusion, the ceramic glucose fuel cells presented here exhibited stable, high power densities at the highest degree of miniaturisation reported to date. **Figure 2.5 e** compares the power density and thickness of the fuel cells in this work with those of existing, lab-stage polymer-electrolyte glucose fuel cells. It can be seen that to date, there have been no abiotic polymer-electrolyte glucose fuel cells with form factors below the micrometre scale. In addition, such polymer-electrolyte glucose fuel cells exhibit low steady-state power densities below 10 μW cm^{-2}.[6,29,41,123,124,126] In contrast, the ceramic glucose fuel cells reported here achieve competitive power densities, with that of the top-performing device reaching 43 μW cm^{-2}, and the average power density across 12 glucose fuel cells reaching 9 μW cm^{-2}. In addition, the thickness of the ceramic glucose fuel cell is 3 times thinner than the next-thinnest device, and approximately 1000 times thinner than other abiotic glucose fuel cells reported to date. It is important to note that fuel-cell thickness directly translates into volumetric power density, implying that a thickness scale-down would not only reduce the device footprint for the patient but also allow for effective stacking to reach adequate total power levels. This is particularly important for implantable device applications, as it allows for ultra-small power sources that enable the miniaturisation of implants. Given the urgent need for miniaturised power sources for the practical realisation of new biomedical implantable devices, this thickness scale-down has the potential to enable the development of an entire range of previously impossible implantable device technologies.

2.3 Conclusion

We have demonstrated the design and operation of a ceramic glucose fuel cell for implantable applications. Indeed, we were able to demonstrate that at body temperature, ceramic glucose fuel cells with proton-conducting ceria electrolyte films of less than 400 nm can deliver a peak power density of up to 43 μW cm^{-2}, albeit at elevated glucose concentrations. Being able to operate such ultra-small ceramic-electrolyte glucose fuel cells using biocompatible and thermally sterilisable ceramics to harvest energy in the human body can become an enabler for future applications in electroceuticals, implantable sensing, and other bio-electronic devices. This sets ceramic glucose fuel cells apart from polymer-electrolyte glucose fuel cells. We confirmed the reproducible operation of these ceramic glucose fuel cells across 12 devices and presented OCV statistics across 150 different glucose fuel cells. The ceramic-electrolyte glucose fuel cell demonstrated here is fully fabricated on silicon using standard semiconductor microfabrication techniques, facilitating its integration into bioelectronics devices. In addition, its use of ceramic and noble metal materials exclusively enables simple thermal sterilisation prior to implantation and promises long-term stability and overall robustness. Moreover, we have demonstrated that ceria films can be used as the electrolyte of room-temperature energy-conversion devices using through-plane proton conductivity, which could serve as a model for other small-scale low-temperature energy harvesters. Collectively, these ceramic glucose fuel cells constitute the smallest implantable power source to date and put new applications in highly miniaturised implantable devices into perspective.

2.4 Experimental Methods

2.4.1 Overview

Micro-glucose fuel cells in the form of free-standing ceria membranes were designed and fabricated using ceramic thin films, metal sputtering, and a microfabrication route based on standard microfabrication techniques. Free-standing membranes were fabricated in the sequence of first creating free-standing Si_xN_y membranes integrated on silicon as a support for the subsequent deposition of a 250-nm layer of ceria as the proton-conducting electrolyte. The supporting layer of Si_xN_y was then removed, and metal electrodes were applied in a final step *via* magnetron sputtering. Here, a 100-nm nano-porous Pt electrode served as the anode, and a dense 20-nm Pt electrode served as the cathode. The entire fabrication process is schematically depicted in the supplementary information (**Figure 9.1**).

2.4.2 Fuel-cell fabrication

One hundred double-side-polished, <100> oriented 4" silicon wafers with thicknesses of 380 µm (Sil'tronix, France) served as the initial substrates for all the subsequent processing. The wafers were coated by the supplier with 200 nm of Si_xN_y on both sides using low-pressure chemical vapour deposition, resulting in low-stress films, which is a prerequisite for forming the free-standing ceramic membranes. The wafers were cut into square pieces measuring 22.3 mm × 22.3 mm using a dicing saw (DAD-3240, DISCO, Japan). After dicing, free-standing Si_xN_y membranes were fabricated as a support for the subsequent ceria membrane assembly. To create the free-standing Si_xN_y membranes, we employed an etching mask of photoresist (AZ 5214, Merck KGaA, Germany) with 30 open squares as a template for the membranes, patterned *via* photolithography. The silicon nitride was locally removed inside these squares via reactive ion etching (Plasmatherm, USA), opening up square windows of pure silicon. The chips were then submerged into KOH solution (20 wt% in water, 80°C; VWR International, USA) for anisotropic wet etching of silicon. This resulted in free-standing membranes of Si_xN_y, measuring 300 µm × 300 µm.

In the next step, we deposited the proton-conducting electrolyte as 250 ± 25 nm of pure cerium oxide for the fuel cells *via* pulsed laser deposition (PLD) on the silicon chip (PLD system by Surface Systems & Technology, Germany, equipped with a COHERENT COMPex Pro laser, wavelength 248 nm, USA). The ceria target was fabricated from commercial ceria powder (99.5% purity, Sigma Aldrich, USA) and densified using the following procedure. The powder was first pressed uniaxially at 440 bar for 2 min and then pressed isostatically at 22 kbar for 2 min to form a dense pellet. The pellet was then sintered by heating

to 1400 °C at a heating rate 3 °C min^{-1}, holding at 1400 °C for 4 h, and then cooling to room temperature at a cooling rate of 5 °C min^{-1}. The PLD deposition was performed at a distance of 75 mm, with a substrate temperature of 400 °C and a chamber pressure of 0.026 and 0.078 mbar of O_2. Two different microstructures of the ceria proton-conducting electrolyte were deposited via PLD. Dense ceria was deposited with 6100 shots at a laser fluence on the target of 1 J/cm^2 and a laser repetition rate of 1 Hz. Rough ceria was deposited with 3000 shots at a laser fluence on the target of 2.75 J/cm^2 and a laser repetition rate of 1 Hz.

Next, we deposited 100 ± 10 nm of porous Pt as the glucose-facing fuel-cell anode, which was deposited on top of the ceria thin film via reactive magnetron sputtering (Kurt J, Lesker, USA; Pt target: 99.99% purity, ACI Alloys). The deposition procedure for nano-porous Pt was adapted from a fabrication route previously reported by Jung et al.[119] Briefly, PtO_x was sputtered via DC magnetron sputtering under an oxygen-rich atmosphere (70% O_2 and 30% Ar, both ultra-high-purity grade, Airgas; chamber pressure 10 mTorr) and was subsequently thermally reduced via a heat-treatment process (400 °C–600 °C) under Ar or 5% H_2 in Ar for 1–8 h. A shadow mask was used during the sputter deposition of the anode to pattern rectangular individual electrodes for each fuel cell, serving both as the electrodes and the current collectors.

The supporting layer of Si_xN_y was then removed via a second reactive-ion-etching step. Finally, 20 ± 2 nm of dense Pt was deposited on the backside of the chip as the oxygen-facing fuel-cell cathode, covering the entire backside without masking. The dense Pt cathode was deposited via DC magnetron sputtering at 10 mTorr Ar (ultra-high purity grade, Airgas) using the same sputtering system and target as above.

2.4.3 Characterisation and measurements

OCV and current–voltage profiles of the fuel cells were measured using an electrochemical characterisation system and the corresponding data collection software (VSP-300, BioLogic, France). XRD was performed on an X-ray diffractometer equipped with a 2D detector using Co K_α radiation at a voltage of 40 kV and current of 40 mA (D8 GADDS, Bruker, USA), and Raman spectroscopy was performed on a confocal Raman microscope (Alpha 300, WITec, Germany). SEM was performed on a field-emission scanning electron microscope (Ultra Plus, Zeiss, Germany). Electrochemical measurements were performed in a custom-designed case fabricated from PEEK and PMMA. We designed the measurement enclosure to enable the flexible and reproducible characterisation of glucose fuel-cell devices on chips containing 30 devices under controlled fuel supply in a two-chamber configuration. The case measures 80 mm × 80 mm with a thickness of 15 mm and contains a slot of 22.6 mm × 22.6 mm to hold the glucose fuel-cell sample. The measurements were configured such that glucose solution (0.5 M in phosphate buffered saline solution, all from VWR International, USA) flows over the top side of the anode of the fuel-cell chip while the bottom is exposed to air, and both sides are tightly sealed using silicone paste (Baysilone, Bayer, Germany).

Electrochemical measurements were performed using spring-loaded needles, with the case allowing rapid sequential measurement of all 30 glucose fuel-cell devices housed on a single chip. Overall, this design enabled the measurement of the OCV of 150 glucose fuel-cell devices and the current–voltage profiles of 12 fuel cells. Glucose solution was de-aerated by bubbling N_2 (ultra-high purity grade, Airgas, USA) through the solution for 24 h before any measurement. A peristaltic pump (Masterflex C/L 1–6 rpm, Masterflex, USA) was used to flow glucose solution over the glucose fuel-cell chip at a flow rate of 150–300 μL min^{-1}. The glucose fuel cells were exposed to deionised water for 12 h and to deaerated glucose solution for an additional 12 h prior to any characterisation of the OCV or IV profile. All the water was Type 1 ultra-pure water (MilliQ 8, Millipore, USA). Electrochemical impedance spectroscopy measurements were performed using a Zahner IM6 potentiostat (Zahner-elektrik, Germany) in the frequency range of 1 MHz to 100 mHz at a 50-mV amplitude, and the spectra were analysed and fit using the software ZView (Scribner Associates, USA). Impedance measurements were performed in a controlled temperature and atmosphere chamber (Linkam Scientific, UK).

3. Chapter 3: Ceramic-Electrolyte Glucose Fuel Cell Design Evolution and Developing a Glucose Fuel Cell Testing Apparatus

Adapted from P. Simons, S. A. Schenk, M. A. Gysel, J. L. M. Rupp. Design, Microfabrication and Testing Apparatus for Ceramic -Electrolyte Glucose Fuel Cells. *Manuscript in revision (2021)*.

Chapter Abstract

Next-generation implantable devices such as sensors, drug delivery systems or electroceuticals offer new ways to treat diseases, monitor body functions, and augment physiological processes. In particular, these devices are undergoing a rapid trend towards increased miniaturization, in order to minimize the impact these devices have on the patient. We have recently demonstrated a novel ceramic-electrolyte glucose fuel cell which constitutes a promising alternative to power such highly miniaturized implantable medical devices by harvesting energy that is readily available inside the human body. Here, we report on the development of a suitable microfabrication route and characterization apparatus for this new type of glucose fuel cell, and the design choices made to achieve a proof-of-concept. To succeed in the design of functional glucose fuel cells based on ceramic electrolytes we had to develop a microfabrication route specific to the free-standing membrane architecture and new electrochemistry of this ceramic electrolyte fuel cell. In addition, a dedicated characterization apparatus was constructed, consisting of a custom-designed glucose fuel cell chip flow case, a system of electrical contacts for high-throughput characterization, and liquid/gas flow handling. All materials including the substrate, electrolyte, and electrode materials, were selected with biocompatibility and on-chip processing in mind, and the device design and processing was developed to allow for successful device operation. The ceramic electrolyte glucose fuel cell design, microfabrication route, and testing apparatus were improved and enhanced through multiple iterations, leading to the successful proof-of-concept recently reported. This constitutes a blue-print for the successful development of a new glucose fuel cell system and its corresponding peripheral equipment, and can serve to guide the research and development of other electrochemical devices and characterization systems.

3.1 Introduction

Implantable medicine is currently undergoing dramatic changes with implantable devices becoming more capable and more miniaturized than ever before. These devices, shown in **Figure 3.1**, include mature biomedical devices such as the cardiac pacemaker or cochlear implants, and less mature developments such as electroceuticals and implantable sensors, and are evolving rapidly to tackle some of today's most pressing health challenges. Many newly developed implantable devices share two features that will be paramount in their further development: first, they are being increasingly miniaturized in order to minimize the impact they have on patients,[128,129] and second, they require a steady supply of energy, that is usually in the range of 100 nW to 1 mW.[96–98] In order to meet these demands, new power sources are needed since existing implant technologies largely rely on the Li-I_2 pacemaker battery[10,11], a primary cell that needs to be replaced once the energy stored in the battery is depleted.

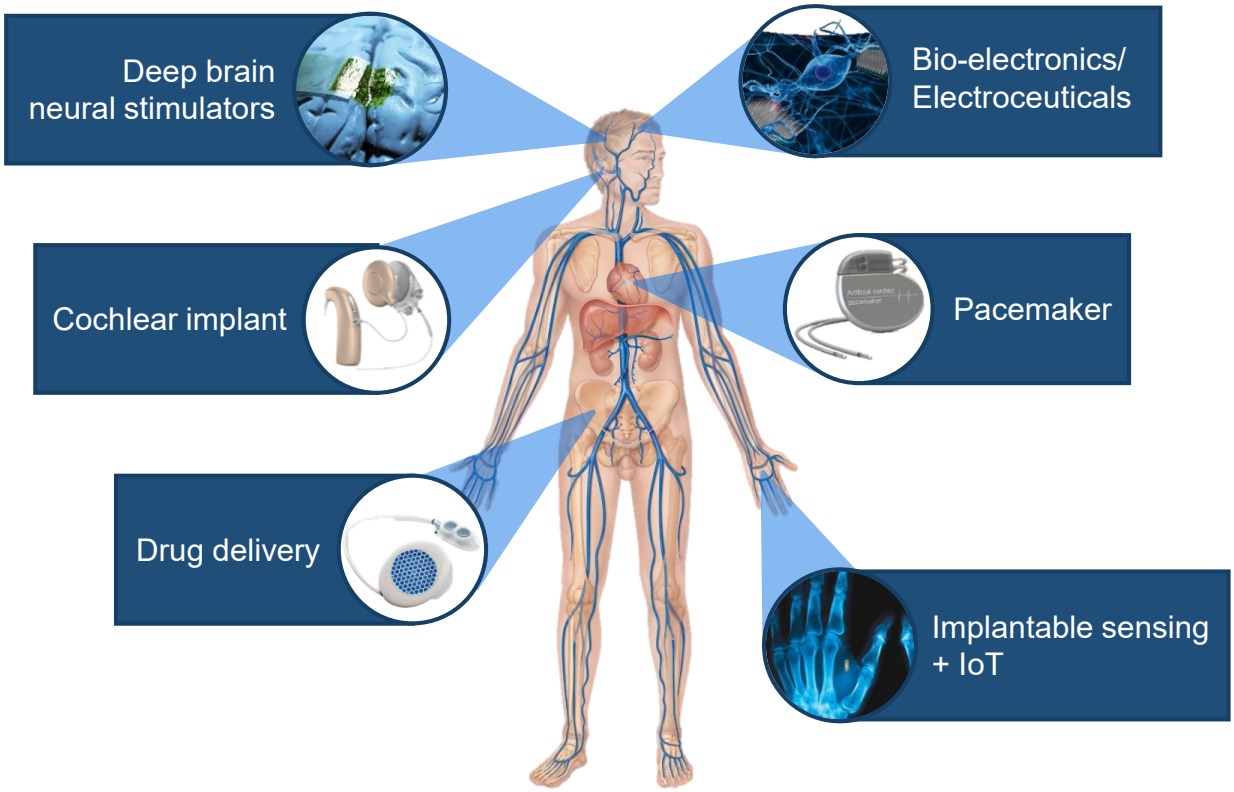

Figure 3.1 Overview over different implantable devices, from mature technologies such as the pacemaker, cochlear implant, or drug delivery systems, to new classes of devices such as deep brain neural stimulators, electroceutical or implantable sensors. Implantable devices follow two trends: they are being increasingly miniaturized in order to minimize their impact on patients and they require a steady supply of energy between100 nW to 1 mW.

In recent years, glucose fuel cells have experienced a renaissance of research efforts, since they promise a reliable long-term power source that harvests energy readily available in the human body.[6,8,100] By harvesting glucose in body fluids and converting it to electricity, glucose fuel cells void the need for batteries and thus replacement surgeries. In addition, they promise to overcome the shortcomings of other potentially implantable power sources such as thermoelectric[15,16], triboelectric[17,18] or piezoelectric[19,20] generators. All these devices are limited by the locations where they can be implanted, since thermoelectric generators require a thermal gradient and triboelectric/piezoelectric generators require kinetic energy to be harvested. In contrast, glucose fuel cells offer greater flexibility in terms of their implantation location within the body, and have been explored to be implanted in various body fluids such interstitial fluid[6], the bloodstream[6], tears[47], or cerebrospinal fluid[29].

We have recently demonstrated a glucose fuel cell based on a ceramic proton-conducting electrolyte, ceria.[130,131] This new type of implantable power source aims to overcome some of the key challenges associated with existing implantable power sources, and also addresses many drawbacks of previous glucose fuel cell concepts in terms of both the electrolyte and electrode catalysis. By using a ceramic proton conducting electrolyte instead of traditionally used polymeric proton exchange membranes, this ceramic glucose fuel cell can achieve a high degree of miniaturization down to the length scale of less than 400 nanometers. In addition, the electrolyte choice of a ceramic proton conducting electrolyte ensures that the glucose fuel cell can be easily thermally sterilized. This overcomes key challenges associated with polymeric proton exchange membranes such as Nafion, for which miniaturization is limited and thermal sterilization is challenging due to irreversible swelling and conductivity loss at temperatures above 120 °C.[74,76,77] At the electrode, the use of abiotic, noble metal catalysis ensures simple integration into electronic devices using conventional semiconductor microfabrication processes. In addition, abiotic catalysts promise long term stability and facile charge transfer, areas which are frequent challenges associated with the enzymatic catalysts that are commonly used in glucose fuel cells to date. [27,28,39,40]

In this paper, we present the rationale of the device and engineering choices made that enabled the recently demonstrated proof-of-concept of a ceramic-electrolyte glucose fuel cell[130] to power implantable medical devices. We first detail the operation principle and materials choices made in designing ceramic-electrolyte glucose fuel cells. We detail the microfabrication route that was developed to enable the fabrication of such ceramic-electrolyte glucose fuel cells on silicon for easy integration into bioelectronic devices, in accordance with the materials selections made. This microfabrication route was carefully engineered to optimize device performance, maximize fabrication yield, and enable reliable device characterization. In addition, we present the development and engineering of dedicated testing apparatus, that was custom-designed to operate and characterize this novel type of glucose fuel cell. Finally, it is summarized how the

evolution of the fuel cell components, device design, and testing apparatus influenced each other and enabled the proof-of-concept of successfully operating these glucose fuel cells across 150 devices as reported.[130] This present work constitutes a blue-print for the successful design and development of a new glucose fuel cell system and its corresponding peripheral equipment, and serves to guide the research and development of other electrochemical devices and characterization systems.

3.2 Operational principle of glucose fuel cells

Glucose fuel cells generate electricity by electro-oxidation of glucose with oxygen. A complete oxidation of glucose, $C_6H_{12}O_6$, to water and carbon dioxide constitutes a 24-electron process. The electrode reactions and overall reaction of this complete oxidation are shown in equations (Eq. 4) - (Eq. 6).

Anode reaction: $$C_6H_{12}O_6 + 6\,H_2O \rightarrow 6\,CO_2 + 24\,H^+ + 24\,e^-$$ (Eq. 4)

Cathode reaction: $$6\,O_2 + 24\,H^+ + 24\,e^- \rightarrow 12\,H_2O$$ (Eq. 5)

Overall reaction: $$C_6H_{12}O_6 + 6\,O_2 \rightarrow 6\,CO_2 + 6\,H_2O$$ (Eq. 6)

The complete oxidation of glucose with oxygen has a thermodynamic Gibbs free energy of $\Delta G^0 = -2.87 \cdot 10^6$ J mol^{-1}, which corresponds to an electrochemical potential of $U^0 = 1.24$ V.[6]

However, it was found in early studies on abiotic glucose fuel cells,[132] and confirmed on later manifestations of the same, that glucose is commonly only partially oxidized in such fuel cell systems. It was observed that glucose oxidation only completes the first intermediate oxidation reaction, namely the formation of gluconic acid. This reaction is a 2-electron process, described by equations (Eq. 7) - (Eq. 9).

Anode reaction: $$C_6H_{12}O_6 + H_2O \rightarrow C_6H_{12}O_7 + 2H^+ + 2e^-$$ (Eq. 7)

Cathode reaction: $$\frac{1}{2}O_2 + 2H^+ + 2e^- \rightarrow H_2O$$ (Eq. 8)

Overall reaction: $$C_6H_{12}O_6 + \frac{1}{2}O_2 \rightarrow C_6H_{12}O_7$$ (Eq. 9)

This reaction has a significantly lower Gibbs free energy than the complete oxidation, namely $\Delta G^0 = -2.51 \cdot 10^5$ J/mol, and an electrochemical potential of $U^0 = 1.08$ V.[116]

Figure 3.2 schematically depicts the operational principle of a glucose fuel cell. At the anode, glucose is oxidized under the presence of water to form gluconic acid, which releases two protons and two electrons, (Eq. 7). The protons travel through the electrolyte to the cathode, where they react with oxygen and electrons to form water (Eq. 5). The electrons travel from the current collectors through an external circuit, closing the circuit and powering external equipment, such as an implantable device.

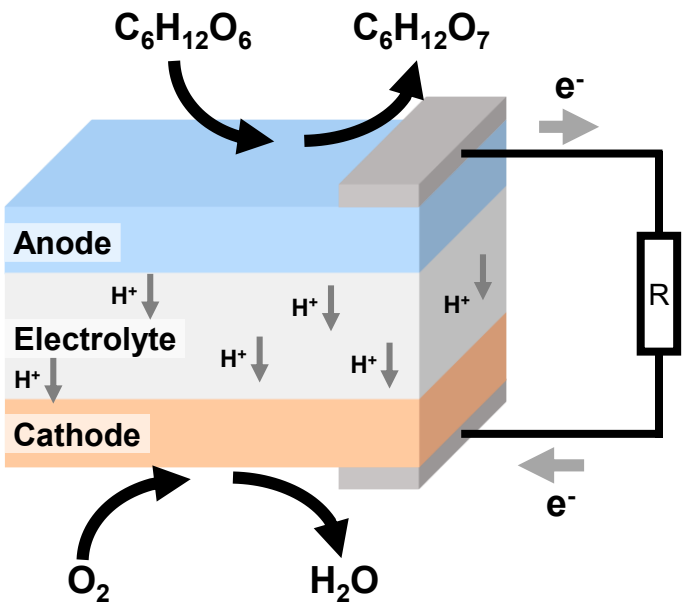

Figure 3.2 Operation principle of a glucose fuel cell. At the anode, glucose is oxidized to form gluconic acid, which releases two protons and two electrons. The protons travel through the electrolyte to the cathode, where they react with oxygen and electrons to form water. The electrons travel from the current collectors through an external circuit powering a load.

3.3 Materials Selection

3.3.1 Functional Considerations of Ceria as the Proton-Conducting Electrolyte

In a previous study, we have carefully laid out the motivation to develop glucose fuel cells based on the ceramic proton-conducting electrolyte ceria.[130] In short, both, existing polymer-electrolytes such as Nafion, and state-of-the-art proton conducting perovskites such as yttria-doped barium zirconate (BZY) exhibit prohibitive drawbacks for implantation. Polymeric membranes are limited in their potential to be miniaturized and ability to be thermally sterilized, while BZY is a known toxin. When used as the proton-conducting electrolyte in a glucose fuel cell, ceria can overcome many of the challenges associated with these electrolyte material types. Hydrated ceria is a proton conductor at low temperatures, with increasing proton conductivity for decreasing temperatures due to increased water uptake at lower temperatures.[79,82–84] Ceria is thermally stable up to well above 1000 °C, meaning that thermal sterilization is trivial. In addition, ceria is non-toxic and actively researched in cancer treatment.[113] Importantly, it shows enzyme-like behavior when structured as nanoparticles, which makes it particularly interesting for glucose fuel cell applications.[115] Here, the rationale is the ability to explore whether nanostructured ceria or ceramic-metallic compounds based on ceria can emulate some of the properties of enzymes such as glucose oxidase, which are commonly employed in glucose fuel cells. One drawback of using ceria as the proton-conducting

electrolyte is its residual electron conductivity[127,133] which can cause electronic leakage, and thus lower the operating voltage and power of a glucose fuel cell. However, given the relatively low power requirements of implantable medical devices, and the other benefits of the ceria system as the electrolyte, this drawback does not seem prohibitive for the technology. In addition, microstructural engineering as well as extrinsic doping can be explored in order to suppress electronic conductivity in favor of a high protonic transference number, and thus enhance overall fuel cell performance.

3.3.2 Functional Considerations of Platinum Electrodes for Selective Catalysis and Microfabrication

To develop abiotic glucose fuel cells with high performance in a single chamber configuration, highly selective abiotic catalysts are required for both the anodic and cathodic reaction. Besides high selectivity, additional requirements for implantable glucose fuel cell catalysts are biocompatibility and long-term stability. Finally, for easy integration with bio-electronics, it is desirable that catalyst materials can be processed using standard semiconductor manufacturing techniques. Through this, it will be possible to integrate such materials into highly miniaturized, long-term-stable power sources which are required for new implantable technologies such as bio-electronics.

Catalyst materials for glucose fuel cells can be separated by the electrode reaction which they catalyze, i.e. for the anode/glucose oxidation reaction and for the cathode/oxygen reduction reaction.

Anode side (selective glucose oxidation)

Kerzenmacher et al. and Kloke et al. have used Raney-type platinum/zinc anodes for selective glucose oxidation[40,42], and Oncescu et al. have used Raney-type platinum/nickel for the same reaction[27]. In addition, Fishman et al. have demonstrated a system of selective catalysts consisting of noble metal alloys such as Au/Pd and Au/Pt in combination with lead acetate.[36] However, in the cases of Oncescu et al. and Fishman et al, the biocompatibility of the catalyst systems is highly questionable due to the use of toxic metals, namely nickel and lead.

The publication series by Kerzenmacher et al. gives an interesting starting point for anode catalyst materials, however, more rigorous studies are required to determine the selectivity as well as the underlying mechanism of the catalytic anode reaction. Kerzenmacher, Kloke and co-workers explain the selectivity of porous, Raney-type Pt toward glucose oxidation with the observation that the glucose oxidation reaction on platinum is kinetically limited, i.e. scales with active surface area.[23] In contrast, the oxygen reduction reaction on Pt under the presence of glucose is diffusion-limited, and thus does not scale with area.

Therefore, Pt electrodes with high specific surface area are selective towards the glucose oxidation reaction in this model. However, this model is likely incomplete, since it does not take into the consideration the effects of residual sacrificial metals that remain after etching an alloyed Pt-containing film such as PtCu or PtAl. It is known that alloying metals in Pt modify the surface electronic structure of the system, which in turn modifies the overall catalytic properties of the surface.[134] Therefore, further investigations into the mechanism of catalytic selectivity of such de-alloyed Pt systems are required. Nevertheless, rational microstructural design of porous Pt is a highly promising starting point to develop selective catalysts for the glucose oxidation reaction. Jung et al. have demonstrated a system of nano-porous Pt deposited via a reactive sputtering pathway and subsequent thermal reduction.[119] This material system could be used as a basis for a rigorous study of the catalytic behavior of nanoporous Pt systems, and of the catalytic activity of pure Pt compared to de-alloyed Pt. For these reasons, we chose nanoporous Pt as the anode electrode catalyst system.

Cathode side (selective oxygen reduction)

The depletion layout device introduced by Rapoport et al. is based on the selective catalysis of the oxygen reduction reaction using carbon nanotubes (CNTs).[29] Similar to this, Kerzenmacher et al. have used activated carbon as the cathode catalyst, which shows good selectivity towards the cathode reaction under the presence of glucose.[6] Do et al. have suggested a selective cathode made up of Pd thin films deposited on nanoporous aluminum oxide.[135] In the paper series presented by Kerzenmacher et al, Raney-type Pt with Al as sacrificial alloy is used.[39,41] In addition, it has been suggested that silver is a catalyst for the selective reduction of oxygen under the presence of glucose, however the activity is lower than for systems such as Pt or carbon.[6] The Pt system introduced by Kerzenmacher et al. again relies on the different rate-limiting steps of the oxygen reduction and glucose oxidation reactions on Pt. To function as a selective catalyst for the oxygen reduction reaction, they choose low specific surface area Pt, since the oxygen reduction reaction is diffusion limited. They combine this property with a depletion design, in which the oxygen concentration in the fuel is depleted at the cathode, and thus fuel with a depleted oxygen concentration but physiological glucose concentration reaches the anode. Given the diffusion limited nature of the ORR on Pt, we chose a dense Pt thin film with a thickness of 20 nm as the cathode catalyst.

Overall, of the examples from literature above, we see particular promise in the use of noble metal catalysts such as Pt for integration into ceramic-based glucose fuel cells. Pt can be easily processed using thin film deposition techniques such as magnetron sputtering, which makes it compatible with silicon-based microfabrication, and allows it to be scaled down to the nanoscale for high degrees of miniaturization. Furthermore, the literature indicates that catalytic selectivity can be tuned via controlling the diffusion pathway and specific surface area of Pt, which means the system lends itself to rational microstructural

engineering in a thin film configuration. Pt with controlled microstructural design therefore shows particular promise for device development, in addition to the ability to be directly integrated with silicon-based electronics. We thus select nanoporous Pt as the anode catalyst, and dense Pt as the cathode catalyst, both deposited as thin films with thicknesses of 100 nm or less for our glucose fuel cell designs.

3.4 Device Geometry

Glucose fuel cells are fabricated on Si chips as free-standing membranes, **Figure 3.3 a**, which serve as a proof-of-concept model system defining a two-chamber configuration with the purpose to verify the electrochemical operation principle of the novel ceramic electrolyte glucose fuel cell system. The substrate Si chips measure 22.3 mm × 22.3 mm and were cut from 4" / 100 mm Si wafers. Two iterations of arrangements of glucose fuel cell devices on Si chips were explored and developed throughout this work. The initial proof-of-concept design contained 36 individual free-standing ceria membrane glucose fuel cells arranged in a square pattern, **Figure 3.3 b**, while a second design was made up of only 30 devices, **Figure 3.3 c**. In both designs iterations, each individual glucose fuel cell consists of a free-standing membrane of a Pt-anode / CeO_2-electrolyte / Pt-cathode. Each glucose fuel cell is ~370 nm thin and measures 300 µm × 300 µm in area.

In the initial *alpha* design, **Figure 3.3 b**, the top and bottom of the chip were fully covered with platinum as the electrode catalyst and current collector of both, the anode and the cathode, respectively. Since all glucose fuel cells shared one common top and bottom electrode, respectively, all devices were connected simultaneously, *i.e.* glucose fuel cells could not be contacted individually. This design served as an initial proof-of-concept design, with which the first basic electrochemical probing experiments could be performed for micro-glucose fuel cells. In these first experiments, the aim was to probe whether any electromotive force (i.e., OCV) could be detected between the cathode and anode, without the goal of a refined electrochemical analysis. These first OCV tests of the glucose fuel cells served to answer the question whether the glucose fuel cell microfabrication was successful, and if a basic two-chamber design could be feasible.

In order to be able to contact individual glucose fuel cells and perform electrochemical characterization measurements, a second more advanced *beta* design was developed with individual contact pads at the top electrodes, being the anodes, **Figure 3.3 c**. This step adds significant complexity to the practical characterization as each individual glucose fuel cell is made up of a 300 µm × 300 µm free standing membrane, which is challenging to contact and perform electrochemical measurements on. These

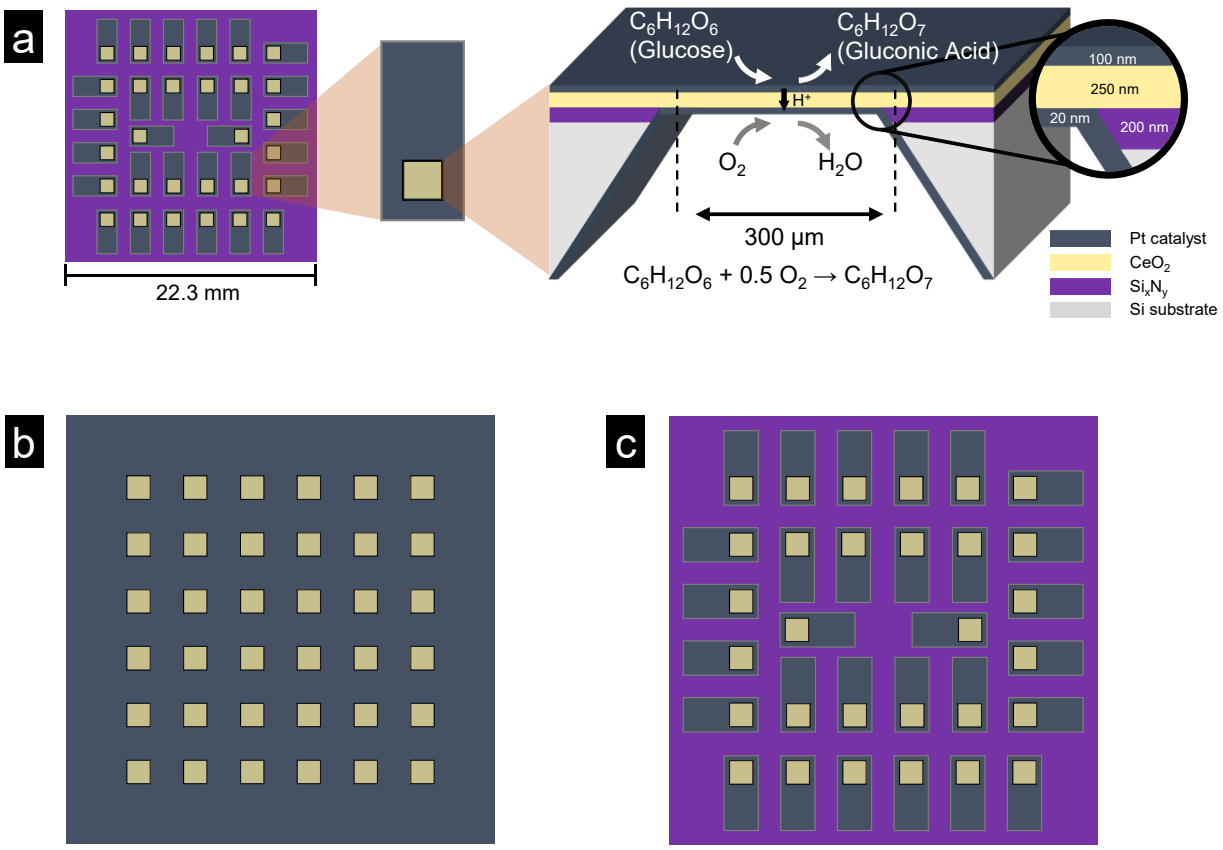

Figure 3.3 Schematic of the geometric layout of the ceramic on-chip glucose fuel cell. **a)** Glucose fuel chip with 30 membranes consisting of a ceria solid electrolyte and top/bottom Pt electrodes, and cross-sectional schematic of an individual glucose fuel cell membrane, measuring a total thickness of 370 nm. **b)** *Alpha* design stage: First iteration of the glucose fuel cell design, with the top and bottom of the device fully covered with Pt, such that all 36 glucose fuel cells are connected simultaneously. **c)** *Beta* design stage: Second iteration of the geometric layout, where each glucose fuel cell has an individual contact pad such that devices could be probed individually. Because of space requirements, the number of devices was reduced to 30 in this layout.

membranes are fragile and easily ruptured by nature in contacting. It was confirmed that the free-standing membrane devices are indeed electrochemically active by means of detecting an OCV signal. Based on that assessment efforts were directed to perform more controlled measurements of individual devices instead of earlier cumulative measurements of all glucose fuel cells on a chip from the earlier chip design. It was found that decoupling the characterization of each individual fuel cell from other devices adds robustness to the entire fabrication process since microscopic pinholes that could lead to a short circuit of one device would not affect the operation of other membranes on the same chip. Since individual contacting pads require additional space and lead lengths should be kept to a minimum, the geometric arrangement of fuel cell devices was adapted such that platinum contact pads could be deposited. This required that the amount

of fuel cells was reduced from 36 to 30 devices between the *alpha* and *beta* design stages. To fabricate these nanoscale devices, a series of micro-fabrication steps was developed, and a key challenge in developing this fabrication route is to ensure fabrication of free-standing membranes without cracks or failures. The microfabrication route is discussed in detail in the following section.

3.5 Fabrication Process

3.5.1 Microfabrication route

A critical feature of the ceramic-electrolyte glucose fuel cell presented earlier is that it is fully integrated into silicon and is fabricated using standard semiconductor fabrication techniques. This enables the fuel cells to be directly integrated into bioelectronic devices, which would reduce the need for interconnects or additional packaging associated with an implant's power source. To achieve this on-chip integration, a microfabrication route suited to assemble glucose micro fuel cells had to be developed, which was further refined between a fabrication *Route 1*, **Figure 3.4 a**, and an improved *Route 2*, **Figure 3.4 b**.

The overall microfabrication route used to fabricate glucose fuel cells based on free-standing ceria membranes is depicted in **Figure 3.4**, and consists of the following steps: (1) <100> oriented 4'' Si wafers of 380 µm thickness with 200 nm of low stress Si_xN_y coated on both sides were purchased from Sil'tronix, France. (2) The back side is patterned via photo-lithography, to template a square etching profile of squares measuring 840 µm × 840 µm. (3) Subsequently, Si_xN_y is etched via reactive ion etching, to open up square shaped windows and create an etching mask for (4) the subsequent wet etching process using KOH. Anisotropic KOH etching of <100>-oriented Si forms a characteristic angle of 54.7° with the surface, due to the orders of magnitude slower etch in the <111> direction. Given this geometry and the etch mask dimensions, the bottom of the trough forms a square silicon opening of 300 µm × 300 µm, with free-standing membranes of Si_xN_y which serve as the substrate for subsequent ceria deposition. The geometric configuration of the anisotropic KOH silicon etching and the remaining free-standing Si_xN_y membranes is displayed schematically in **Figure 3.5**. (5) Next, ceria is deposited via pulsed laser deposition (PLD) with a thickness of 250 nm. The details of the PLD deposition are discussed in the following section. After the electrolyte deposition, two variants of the final steps of assembling glucose fuel cells are performed, i.e.

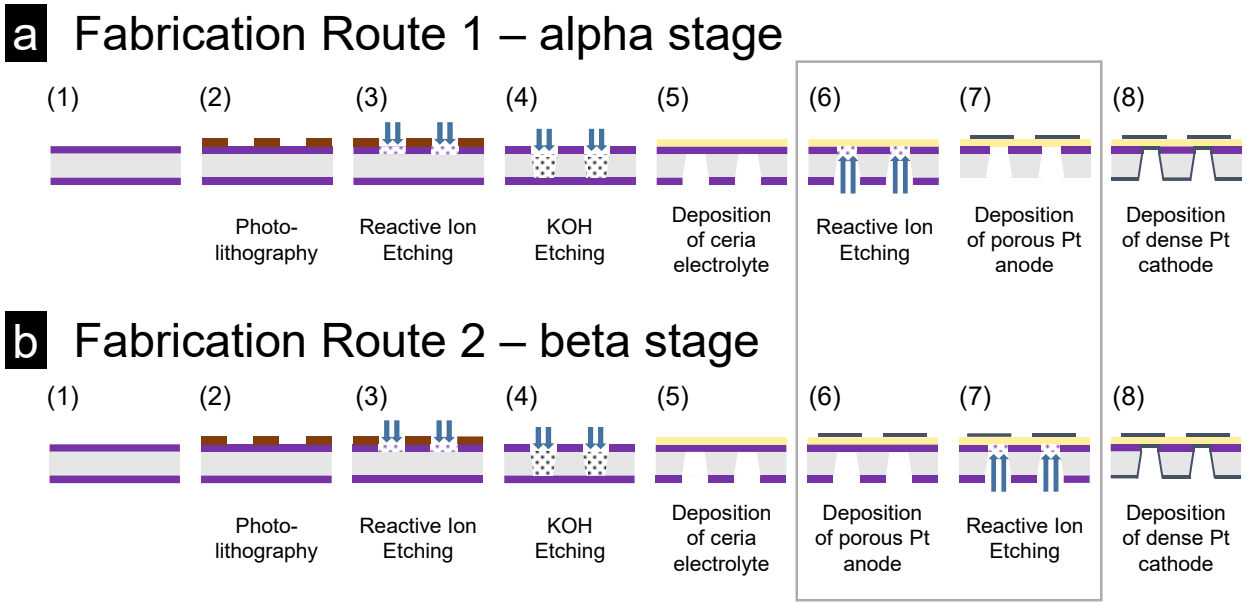

Figure 3.4 Microfabrication route to fabricate ceramic-electrolyte glucose fuel cells. The microfabrication route is based on standard semiconductor fabrication processes for easy on-chip silicon integration of the glucose fuel cell device. A combination of photo-lithography, reactive ion etching, wet etching, magnetron sputtering, and pulsed laser deposition is employed. Two different fabrication routes were explored. **a)** In *Route 1*, the Si_xN_y support layer is removed via reactive ion etching immediately after the ceria electrolyte deposition. **b)** In *Route 2*, the porous Pt anode is deposited first as an additional mechanical support, before removal or the Si_xN_y support layer.

Fabrication *Route 1* and *Route 2* in **Figure 3.4**. In fabrication *Route 1*, after the deposition of the CeO_2 thin film, the supporting layer of Si_xN_y is etched away via (6) a second reactive ion etching step, creating free-standing cerium oxide membranes. (7) Next, 100 nm of porous Pt is deposited via a reactive sputtering and subsequent post-annealing: similar to the method described by Jung et al.[119], PtO_x is deposited via DC magnetron sputtering under an oxygen-rich atmosphere (70% O_2 balanced with Ar). Subsequently, the PtO_x film is reduced via thermal annealing at 400 °C-600°C under 5% H_2 in Ar, resulting in a nanoporous film of pure Pt. In the second variant of the microfabrication route, *Route 2*, (6) the top electrode deposition is carried out prior to (7) the removal of the Si_xN_y support underneath the ceria electrolyte. This serves to increase the mechanical stability of the free-standing membrane system, prior to the removal of Si_xN_y *via* reactive ion etching, a relatively aggressive process. (8) The final step in the glucose fuel cell fabrication in both *Route 1* and *Route 2* is the deposition of a continuous, dense film of 20 nm of Pt on the back side of the silicon chip.

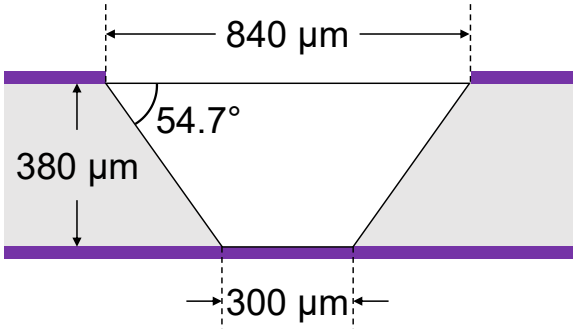

Figure 3.5 Geometric configuration of free-standing membranes fabricated via anisotropic silicon etching with KOH. A square opening measuring 840 µm × 840 µm is etched into Si_xN_y using photolithography and reactive ion etching. The anisotropic etch of silicon with KOH creates a characteristic angle of 54.7° by etching along the (111) plane, which results in a free-standing membrane of Si_xN_y measuring 300 µm × 300 µm.

It was observed that in the initial microfabrication route, *i.e., Route 1*, fabrication yield was in some instances below 10% due to cracking of membranes during Si_xN_y removal, step (6) and annealing of the Pt film, which is part of step (7). For this reason, the second variant of the fabrication route, *Route 2*, where the top electrode is deposited prior to the removal of the Si_xN_y support layer instead of afterwards, was designed in order to increase fabrication yield and reproducibility. First depositing platinum on top of the ceria / Si_xN_y free-standing stack of thin films, prior to removing the Si_xN_y adds a mechanically stabilizing layer to support the ceria ceramic membrane during the reactive ion etching step that follows.

Overall, we selected fabrication Route 2 for further investigations and device characterization, as reported in Ref. [130], due to the higher fabrication yield and overall processing robustness. In addition to the order of processing steps, the fabrication route was adapted multiple times in order to improve fabrication yield, mechanical stability, and electrochemical device performance. Here, the key processing parameters that were adapted were the deposition of the Pt electrodes, and the electrolyte configuration. The details and evolution of these two steps are discussed in more detail in the following.

3.5.2 Pt Electrode Deposition and Optimization for the Glucose Fuel Cell

Pt electrodes serve as the catalysts and current collectors of both the anode and the cathode of the ceramic-electrolyte glucose micro fuel cell. We selected to deposit Pt via magnetron sputtering, a thin film deposition technique that is common in semiconductor manufacturing and commercially available in large scale. By selecting this technique, the fabrication process is ensured to be compatible with microfabrication routes that are employed for the fabrication of micro / nano-electronics, such that the glucose fuel cell system can be fabricated in a fully integrated fashion on-chip with a future bio-electronic device. In the initial, most

basic proof-of-concept ceramic glucose fuel cell prototypes assembled to probe the basic electrochemical operation, both the anode and the cathode were composed of dense Pt with a thickness of 20 nm. In this symmetric cell configuration, one electrode would be exposed to glucose solution, and the other electrode to air, and the goal was to probe whether an electromotive force was present in such a system of Pt thin film / ceria electrolyte / Pt thin film. Due to the symmetric nature of this configuration, no catalytic selectivity was to be expected, and in addition, the low specific surface area of dense Pt films further implied low catalytic fuel conversion on the surface-limited glucose-facing anode, which means the overall power output of such a system operated as a fuel cell is expected to be low. However, the system was already well-suited for basic measurements of an open circuit voltage, a necessary requirement for any future operation as glucose fuel cell.

For the reasons mentioned before, the next development step was to move closer to a system with higher activity and catalytic selectivity. One class of catalyst materials for the selective catalysis of the glucose oxidation reaction is nanoporous Pt. In previous polymer-electrolyte glucose fuel cells, porous Pt has been deposited mainly via a Raney-type de-alloying fabrication route.[40] In this de-alloying route, Pt is first alloyed with a sacrificial metal such as Al, Ni, or Cu, followed by thermal treatment to control the size of Pt clusters. The less noble sacrificial metal is then etched out of the alloy with a chemical etchant, resulting in a highly porous structure of Pt. Depending on the etching time and thermal treatment, the pore size and residual sacrificial metal content can be controlled. However, the use of chemical etching with strong acids or bases is a chemically harsh process, which makes it challenging to integrate with the ultra-thin free-standing membrane design employed in this work. Therefore, a more compatible fabrication route that does not employ chemical etching was developed for the deposition of nanoporous Pt. The fabrication route for porous Pt developed here employs reactive sputtering and subsequent thermal annealing. This fabrication route was adapted from Jung et al.[119], and it does not require a chemically aggressive wet-etching step, making it compatible with ceria[120,121] and a wide range of other ceramic and CMOS materials and deposition techniques. In this process, PtO_x was sputtered via DC magnetron sputtering under an oxygen-rich atmosphere (70% O_2 mixed with 30% Ar). The PtO_x film was subsequently thermally reduced to form porous, metallic Pt via a heat treatment process at 400 °C – 600 °C under reducing conditions such as pure Ar or 5% H_2 in Ar, for 1 – 8 hrs.

3.5.3 Ceria Electrolyte Thin Film Deposition Optimization for the Glucose Fuel Cell

To successfully assemble the ceramic glucose fuel cell on silicon and to operate in liquid glucose solution, it is necessary to balance high mechanical stability of the fuel cell membrane with low chemical cross-talk between electrodes and high proton conductivity of the electrolyte. To balance these requirements for the

ceria electrolyte, two different microstructures of the ceria solid proton-conducting electrolyte were utilized, as detailed in our previous report[130]: a dense, columnar microstructure, and a rough cauliflower-like rough microstructure, both of which are schematically depicted in **Figure 3.6**. Here, we expand on the analysis of these chosen microstructures in our previous proof-of-concept, and detail the microstructural and mechanical implications of the engineered processing route.

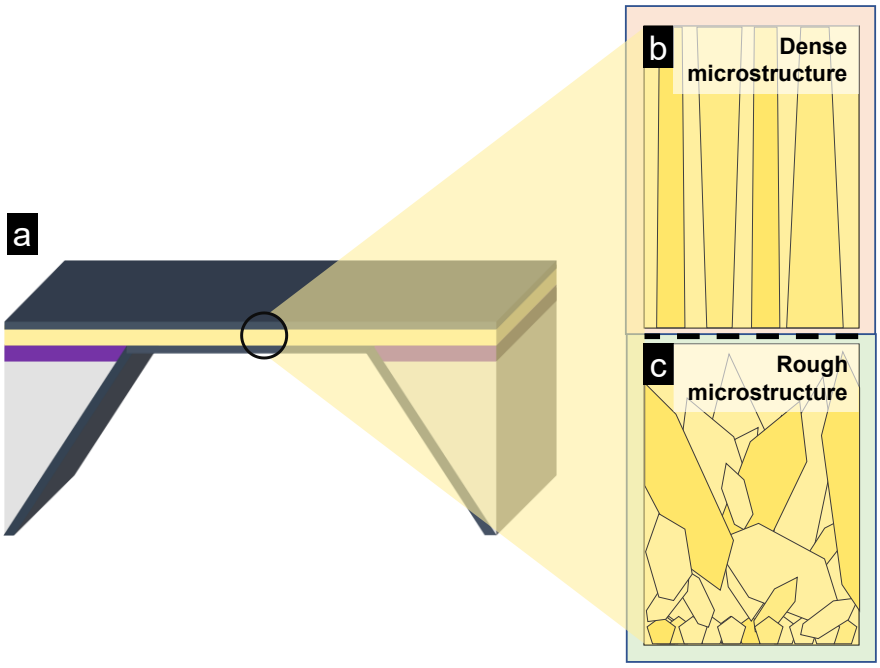

Figure 3.6 Schematic of ceria electrolyte microstructures. **a)** Schematic of the glucose fuel cell free-standing membrane configuration. **b)** Schematic of a dense, columnar ceria microstructure assembled via a low PLD oxygen background pressure of 0.026 mbar. **c)** Schematic of a rough, disordered, cauliflower-type microstructure obtained via a high PLD oxygen background pressure of 0.078 mbar.

Control over the microstructure was achieved by selecting suitable pulsed laser deposition (PLD) parameters for the deposition of ceria. The parameter calibration was carried out based on the known relationship between PLD chamber pressure, temperature, and resulting microstructure, as described in Ref. [117]. There, it was confirmed that below a critical deposition pressure of ~0.05 mbar, ceria thin films deposited via PLD are fully dense, and above, exhibit a rough microstructure.

The dense, columnar microstructure resembles that typically used in micro SOFCs.[90] This microstructure was obtained by performing PLD depositions at a chamber oxygen pressure of 0.026 mbar. A microfabrication route employing this microstructure was explored initially, by adapting fabrication routes for free-standing SOFC membranes. In the dense microstructure, blocking of chemical cross-talk between the two electrodes is prioritized. **Figure 3.6 b** shows this microstructure schematically, and top view,

Figure 3.7 a and cross-sectional view, **Figure 3.7 c**, SEM images confirm the successful growth of a dense, columnar microstructure with a typical grain diameter between 10 and 50 nm.

The rough microstructure, schematically depicted in **Figure 3.6 c**, was developed with two main objectives: increasing proton conductivity and thus fuel cell performance, and reducing stress in the free-standing membrane for higher mechanical robustness. PLD Depositions of this microstructure were performed at a chamber oxygen pressure of 0.078 mbar. The disordered, cauliflower-like microstructure was confirmed through SEM, **Figure 3.7 b and d**. It can be seen from both top view SEM, **Figure 3.7 b**, and cross-sectional SEM, **Figure 3.7 d**, that grains are highly disordered, with porosity near the top of the thin film, and a large fluctuation of grain size between a few nanometers and ~200 nm. In addition, the grain size and disorder increase from the bottom of the film, near the substrate, to the top. In particular, near the substrate the film is fully dense with a grain size at the order of only a few nanometers.

This microstructural design was purposefully chosen to enhance the glucose fuel cell performance. It is known that proton conduction in ceria is dominated by transport at or near the surface.[79,81–83] Therefore, the rough microstructure defines a high-surface area configuration of ceria, and allows water to fill the open porosity from the top of the electrolyte thin film down to the dense region near the substrate, a region that spans ~230 nm in the electrolyte assembly. Only the bottom ~20 nm of the ceria ceramic electrolyte are fully dense, and thus the pathway where proton transport occurs through a fully dense layer of ceria is kept significantly shorter, compared to the fully dense electrolyte configuration described before. This microstructural configuration was developed to increase the overall effective proton conductivity, as well as increase the electrolyte's protonic transference number.

The second important feature of the rough ceria microstructure is that due to the disordered nature of growth, the thin film releases stress during the deposition process, which both increases the mechanical robustness of the resulting free-standing once fabricated and decreases the fracture rate during deposition. Thus, this microstructure is particularly well-suited for further fuel cell development from a practical standpoint, as fabrication, processing, and experimentation are less likely to break the fragile free-standing membrane system.

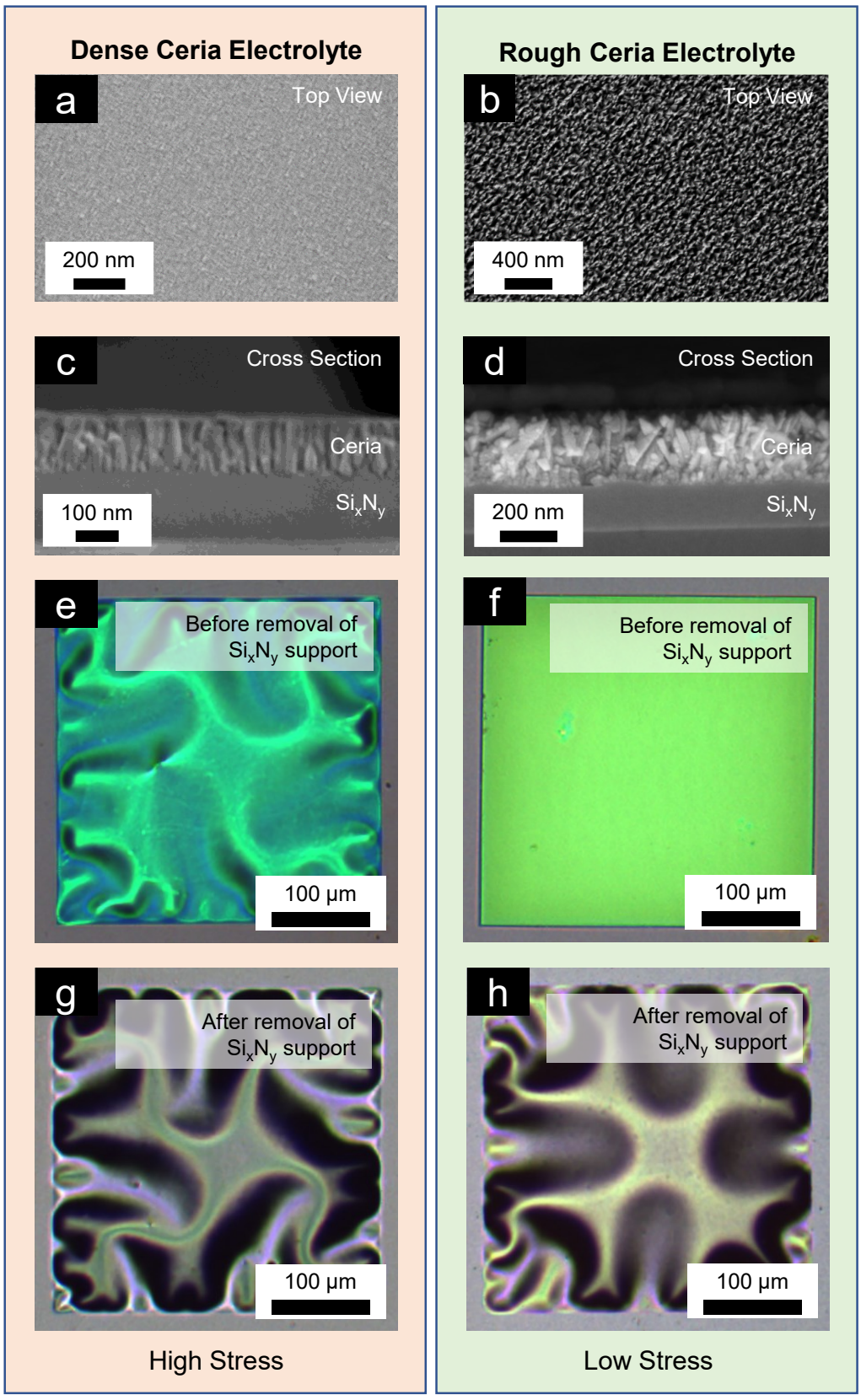
Dense Ceria Electrolyte
Rough Ceria Electrolyte
a
Top View
200 nm
b
Top View
400 nm
c
Cross Section
Ceria
Si_xN_y
100 nm
d
Cross Section
Ceria
Si_xN_y
200 nm
e
Before removal of Si_xN_y support
100 µm
f
Before removal of Si_xN_y support
100 µm
g
After removal of Si_xN_y support
100 µm
h
After removal of Si_xN_y support
100 µm
High Stress
Low Stress

Figure 3.7 Overview of the different ceria electrolyte microstructure designs. **a-d)** SEM micrographs of **a,c)** dense and **b,d)** rough ceria electrolyte. **a)** Top view and **c)** cross-sectional SEM micrograph of dense ceria, showing a dense, columnar microstructure. **b)** Top view and **d)** cross-sectional SEM micrograph of rough ceria, showing a disordered, cauliflower like microstructure. **e-h)** Optical micrographs of free-standing ceria membranes, **e,f)** prior to and **g,h)** after the removal of the Si_xN_y support layer below the ceria electrolyte. e) Dense ceria shows significant buckling before Si_xN_y removal, whereas **f)** rough ceria does not show any visible buckling prior to Si_xN_y removal. **g,h)** After removal **g)** dense ceria shows stronger buckling with narrower ridges compared to **h)** rough ceria. These images before and after Si_xN_y removal indicate significantly lower stress in rough ceria membranes than in dense ones.

The stress state in the free-standing membrane due to the different electrolyte microstructure can be observed in the buckling pattern of the free-standing membranes as observed under optical microscopy, both before and after the removal of the Si_xN_y support layer, **Figure 3.7 e - h**. **Figures 3.7 e and f** show the buckling pattern of ceria thin films that are supported by a Si_xN_y support layer, and it can be seen that the dense ceria electrolyte film, **Figure 3.7 e** shows significant buckling, while the rough ceria film, **Figure 3.7 f**, does not exhibit visible buckling under optical microscopy. Once the Si_xN_y support layer is removed, **Figure 3.7 g and h**, both the dense and rough films show visible buckling. However, the buckling pattern is significantly altered between the two electrolyte microstructures. The rough microstructure, **Figure 3.7 h**, shows a smoother pattern with broader ridges, compared to the dense microstructure, **Figure 3.7 g**. Together, the buckling patterns before and after the removal of the Si_xN_y support layer show that free-standing ceria membranes with the rough microstructure exhibit significantly lower strain than their dense counterparts. This enhances the mechanical stability of the free-standing membrane, and increases fabrication yield.

3.5.4 Overall Fabrication Yield

Achieving a high fabrication yield for the free-standing-membrane-based, full glucose fuel cell device including the ceria electrolyte, as well as the top and bottom Pt electrodes, posed a significant challenge during the device development. At the onset of the device development, fabrication yield was low at less than 10%, with only 2 or 3 successful devices fabricated out of the 30 devices on a single chip. The most challenging processing steps were the removal of the Si_xN_y support layer below the ceria electrolyte via reactive ion etching, and the thermal annealing of the glucose fuel cell in order to re-reduce PtO_x to form nanoporous Pt at the anode. Both of these processing steps occur under harsh conditions, and without careful tuning, can easily damage the fragile free-standing membrane system.

Multiple steps were taken to enhance mechanical robustness and thus yield of the microfabrication. In particular, the ceria electrolyte thin film deposition process was carefully adapted to minimize the strain in

the resulting membrane. As discussed above, a rough, disordered microstructure can significantly reduce the stress in free-standing membranes, and thus improve mechanical robustness under the following processing steps. In addition, PLD depositions were carried out at a low laser repetition rate of only 1 Hz and at a moderate temperature of 400 °C, with the goal to maximize the system's relaxation during deposition, and to minimize problems of thermal expansion coefficient mismatch. Secondly, the order of processing steps was adjusted such that the mechanical stability of the system was maximized. For example, we found that a frequent cause of membrane breakage was the thermal annealing step of the fuel cell membrane, which creates porous Pt from PtO_x. If this step is performed after the Si_xN_y support layer is removed, membranes frequently break during the annealing process. Thus, we reversed the order of the deposition of the top electrode and removal of the Si_xN_y support layer (described above as microfabrication routes 1 and 2). Through this, the Si_xN_y support layer was still present during the annealing step, resulting in near-perfect yield of this step due to the additional mechanical support of the Si_xN_y layer. In addition, this reversal of processing steps had the benefit of creating an additional mechanical support for the free-standing membrane in the form of the Pt layer for the harsh reactive ion etching step which removed the Si_xN_y layer. Overall, these steps increased microfabrication yield to near 100 %, and in particular, the processing order also allowed for successful membrane fabrication even with dense, stressed free-standing electrolyte membranes. These yield improvements do not only mean that fabrication is more robust, a necessary prerequisite for the successful scaling of glucose fuel cell fabrication, but also were beneficial for the electrochemical testing of glucose fuel cells. Every broken glucose fuel cell membrane poses the risk of creating an electrical short when the top and bottom electrodes are deposited, even for neighboring devices. Therefore, fully intact glucose fuel cell devices ensured that electrochemical testing of all devices could be performed with higher reproducibility and reliability.

3.6 Designing a Glucose Fuel Cell Test Setup for Electrochemical Characterization

The first attempts to measure the electrochemical performance of ceramic-electrolyte glucose fuel cell microchips and their membranes required that a new, custom designed characterization set-up was developed, and suitable measurement conditions for ceramic proton-conducting membranes were defined. Unlike other fuel cell types such as solid oxide fuel cells or protonic ceramic fuel cells which operate under gas fuels, the ceramic glucose fuel cell would operate under liquid flow. In addition, the fragile and highly miniaturized nature of the free-standing glucose fuel cell membrane required designing a suitable testing platform that can address individual glucose fuel cell devices on a chip without rupturing membranes. Due

to the new architecture of the ceramic-electrolyte glucose fuel cell, previous polymer-electrolyte glucose fuel cell designs were also unsuitable for characterization. Hence, it was a critical and essential part of this present study to enable the electrochemical characterization of novel ceramic-electrolyte glucose fuel cells by conceptualizing and constructing a new, dedicated fuel cell test rig and testing procedures as detailed in the following.

In all experiments performed to characterize the present glucose fuel cells, devices were operated in a two-chamber configuration, with a liquid glucose-containing fuel at the anode side, and air as the oxygen source at the cathode side. The glucose solution feeding the cathodic reaction was composed of glucose at a concentration of 0.1 M – 1 M, dissolved in aqueous phosphate-buffered saline (PBS) solution, that was de-aerated by flowing nitrogen (Airgas, ultra-high purity grade) through the fuel stock solution. The increased glucose concentration served to prove the general operating principle of the glucose fuel cells, and will be reduced to physiological levels (3-7 mM) in subsequent studies. Similarly, the glucose stock solution was de-aerated to avoid an electrochemical overpotential due to the presence of dissolved oxygen at the anode side, which would reduce the overall cell potential of the fuel cell. In future single-chamber configurations, dissolved oxygen will be present in the fuel mixture. Phosphate-buffered saline (PBS) solution was used to simulate the ionic composition and pH of body fluids such as blood. PBS tablets were used to prepare the stock solution, with a composition of 137 mM sodium chloride, 2.7 mM potassium chloride and 10 mM phosphate buffer, resulting in a pH of 7.4. PBS is a common means to simulate physiological conditions for the characterization of glucose fuel cells, before moving to simulated body fluids that would contain additional species such as proteins or blood cells. It simulates the chemical composition of dissolved species contained in body fluids, and thus forms an appropriate medium for the proof-of-concept of the operation chemistry of a glucose fuel cell. In all measurements presented here, the cathode was exposed to ambient air as the oxygen source, in a so-called air-breathing cathode configuration. This configuration voids the need for complex gas supply systems, and reflects that in the basic two-chamber operation mode of the ceramic glucose fuel cells, no specific needs for the oxygen source are present. In future embodiments, the air-breathing cathode will be replaced by a cathode exposed to liquid fuel containing dissolved oxygen.

3.6.1 Measurement Enclosure: Liquid Flow Case

In order to experimentally characterize this new type of glucose fuel cell, a new dedicated measurement setup was required, as depicted in **Figure 3.8**. The case measures 80 mm × 80 mm with a thickness of 15 mm and is fabricated from PEEK to ensure chemical and thermal stability, in particular for measurements under elevated temperatures. It features a slot measuring 22.6 mm × 22.6 mm to hold the glucose fuel-cell

chip, and which can be sealed for water-tightness using silicone paste. While basic operation of the ceramic glucose fuel cell occurs under body temperature, the enclosure was designed such that higher temperatures can be sustained to allow for temperature-dependent performance measurements. Such measurements will be useful in the future to disseminate the operation principle and rate-limiting step of the ceramic glucose fuel cell. The flow case was designed such that liquid fuel flows over the top side of the chip containing glucose fuel cells, while the bottom of the chip was exposed to air. As such, the fuel cell is operated in a two-chamber layout with the glucose-containing liquid in contact with the anode, and oxygen in contact with the cathode.

In the first iteration of this setup, electrical contacting was only possible with one contacting needle connected to the top side and one needle to bottom side of the glucose fuel cell chip. This measurement configuration, which is shown in the CAD drawings of **Figure 3.8 a and b** corresponds to the first geometric layout of glucose fuel cell chips discussed above, and depicted in **Figure 3.3 b**. In this design stage, all fuel cell devices were probed in parallel, *i.e.,* it was impossible to connect the 36 glucose fuel cells individually. This had the benefit that the voltage of all functioning devices would be summed in operation, increasing the measurement signal, but requiring careful sealing of defective devices prior to any measurement. To allow for more targeted experiments, the setup was upgraded along with a new geometric layout of the measurement specimen (see also **Figure 3.3 c** for the layout of the chip). In the new configuration, boreholes were added to directly contact each individual glucose fuel cell. In this iteration, it was possible to contact each glucose fuel cell individually, which means that a potential short-circuit in one device would not affect the characterization of another device. This allowed for more targeted screening, and comparing the performance of individual devices to each other. However, in this stage only one device could be connected at a given point in time using a gold contacting needle, making screening slow, and devices were usually characterized for multiple days before moving to the next glucose fuel cell membrane. In the third enhancement of the characterization enclosure, spring-loaded needles were attached to the lid of the flow case, which provide reproducible electrical contact with controlled mechanical force to each individual fuel cell device. The spring-loaded needles were wired to a plug board that allowed for facile contacting with glucose fuel cells and helped rapidly measure all 30 glucose fuel cells. This configuration is depicted in **Figure 3.8 c and d**, with the spring-loaded needles shown in **Figure 3.8 e**. Through the combination of a plug board and spring-loaded needles, it was now possible to switch between individual glucose fuel cell devices within seconds, and measure electrochemical performance metrics such as the OCV of 30 individual devices within 15 minutes. By performing such rapid screening, it was possible to obtain statistics on electrochemical performance metrics of the glucose fuel cell chips across 150 different fuel cell membrane devices.

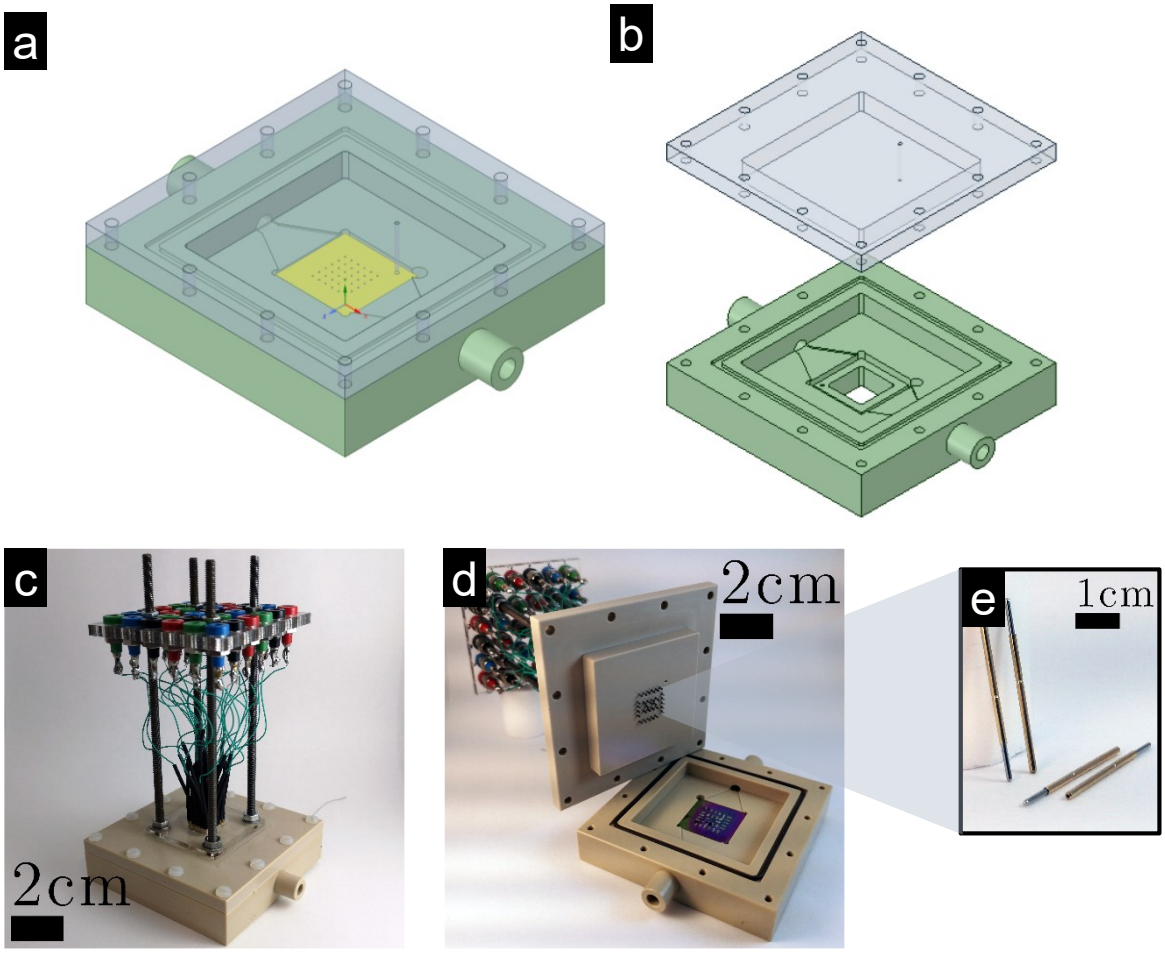

Figure 3.8 Liquid flow case as measurement enclosure, and rapid-screening contacts. **a, b)** CAD drawing of the custom-designed liquid flow case, in **a)** closed and **b)** open form. The glucose fuel cell chip is placed in a tightly fitted slot, and liquid sealing is achieved with silicone paste. Glucose solution flows over the top side or anode of the chip, whereas the bottom side or cathode is exposed to ambient air as the oxygen source. **c-e)** Enhanced characterization setup with the ability to perform rapid screening and contact all 30 individual glucose fuel cells in a reproducible and controlled fashion. This is enabled through a plugboard for electrical contact and **e)** spring loaded needles for reliable contacting.

3.6.2 Characterization Setup: Periphery

It is important to note, that beyond the construction of the flow case housing the glucose fuel cell chips, it was necessary to construct the entire measurement periphery to perform successful glucose fuel cell characterizations. A dedicated setup was constructed, consisting of liquid handling, nitrogen gas supply, a

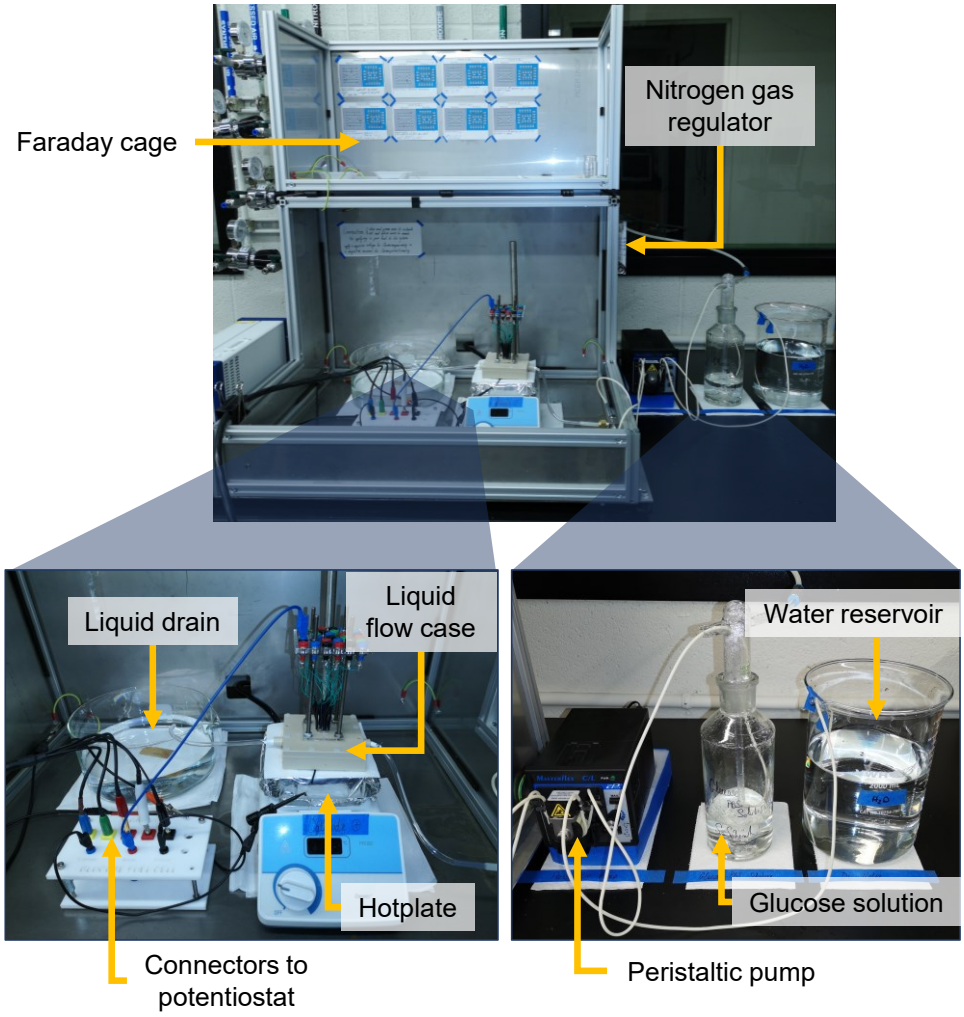

Figure 3.9 Photographs of the full characterization setup including the liquid flow case, as well as gas and liquid handling, and electrical connections. A peristaltic pump was used to pump glucose solution from a water bubbler for deaeration to the glucose fuel cell flow case. The setup was placed inside a metallic Faraday cage for shielding during measurements, and the flow case was placed on a hot plate for electrochemical characterization at elevated temperature.

Faraday cage, and electrical wiring, **Figure 3.9**. The glucose solution was stored in a gas bubbler and was deaerated by bubbling nitrogen gas through the glucose solution. From the bubbler, glucose solution was pumped to the glucose fuel cell flow case using a peristaltic pump, which has the key benefit that the pump is never in direct contact with the liquid, and instead is pumped by periodically compressing the tubing which contains the liquid. This ensures that fuel transport occurs free of contamination. A second reservoir, containing pure water, was installed, which was used to purge the glucose fuel cells with water to equilibrate the system, and to purge the piping from glucose solution after any measurement. The glucose fuel cell flow case was placed on a hot plate for measurements at elevated temperature, and the whole assembly was

placed inside a metal cage for electro-magnetic shielding during electrochemical characterization. Overall, this setup enabled the controlled and reproducible characterization of ceramic glucose fuel cell samples.

3.7 Glucose Fuel Cell Design Stages

To summarize the different design stages of both the ceramic-electrolyte glucose fuel cells and the dedicated characterization setup that was developed concurrently, we provide an overview over the different development stages:

1) *Initial, preliminary tests.* Here silicon wafer pieces are manually broken into sets of glucose fuel cell membranes. Both sides of the chip were fully covered with dense Pt, and contact is made using simple gold needles. Glucose solution is supplied via a syringe in the form of droplets.
2) *Diced samples and membrane flow case.* Silicon chips were now cut using a dicing saw to achieve a controlled and consistent sample geometry. The membrane flow case was designed such that a two-chamber glucose fuel cell operation could be easily achieved, with glucose solution flowing over the top of the sample.
3) *Individually contacted samples and porous Pt anode.* The glucose fuel cell chip layout was modified such that individual glucose fuel cells could be contacted, be creating individual contact pads per glucose fuel cell instead of depositing a continuous layer of Pt covering the entire chip surface. In addition, instead of dense Pt, nanoporous Pt was employed as the glucose-facing anode, to improve catalytic activity, and transition from a symmetric device to a fuel cell with dedicated cathode and anode designs.
4) *Reversal of deposition and etching steps.* The order between porous Pt anode deposition and the removal of the Si_xN_y support layer was reversed, such that in this next iteration, the support layer was removed after the anode was deposited. This achieved higher mechanical stability and increased fabrication yield.
5) *Modified electrolyte microstructure.* In the next step, the ceria electrolyte microstructure and deposition conditions were investigated. Two electrolyte configurations were explored, namely the

original dense, columnar microstructure, and a rough, disordered, cauliflower-type microstructure. The rough microstructure improved fabrication yield, lowered membrane stress, showed higher OCV values, and was designed to improve proton conductivity and the protonic transference number.

6) *Modified testing setup for high-throughput screening.* The next iteration improved the performance characterization apparatus, by moving from individually placed contact needles to a system of spring-loaded needles contacted to a plug-board. With this new apparatus, fast device screening was possible, and measurement reproducibility between individual glucose fuel cell devices was greatly enhanced.

3.8 First Experiments

The recently demonstrated ceramic-electrolyte glucose fuel cells were developed incrementally from basic initial tests such as measuring the open circuit voltage under stagnant conditions, to rapid screening and full IV-curve characterization of multiple devices. Here, we present the first preliminary experiments that led up to the recently reported fuel cell operation through I-V-curves and the screening. These preliminary experiments were constituted of first OCV measurements to probe the basic fabrication success of glucose fuel cell devices, and verify the electrochemical characterization setup and procedures established here.

3.8.1 Initial Tests: OCV Under Stagnant Conditions

One of the basic preliminary verification measurements was defined on the initial, un-optimized design of the ceramic glucose fuel cell: a free-standing membrane consisting of a dense layer of cerium oxide as the proton-conducting electrolyte, with dense Pt electrodes on both sides. In this symmetric configuration, the ceria electrolyte had a thickness of 250 nm, and the Pt electrodes each were 20 nm thick. The top and bottom electrodes were made up of a dense, continuous layer of Pt, meaning that all devices were probed simultaneously. Electrical contact to the top and bottom was made with gold needles. An optical photograph and micrograph of this initial prototype are displayed in **Figure 3.10 a and b**. To verify the basic electrochemical functionality of this system, droplets of glucose solution in PBS were dripped on the top surface of the fuel cell chip, using a syringe. **Figure 3.10 c** shows a successful test of a glucose solid state fuel cell chip: The plot displays the open circuit voltage (OCV) of the glucose fuel cell over time when droplets of glucose solution are dripped on the surface of the fuel cell. Each sharp peak of the potential

occurs at an instance when a droplet of glucose solution is placed on the top electrode of the fuel cell chip. A maximum in OCV of 140 mV is detected upon injection of glucose to the fuel cell. This first test demonstrated that the novel fuel cell type is indeed electrochemically active and that further development and improvement of the device toward an implantable power source is warranted.

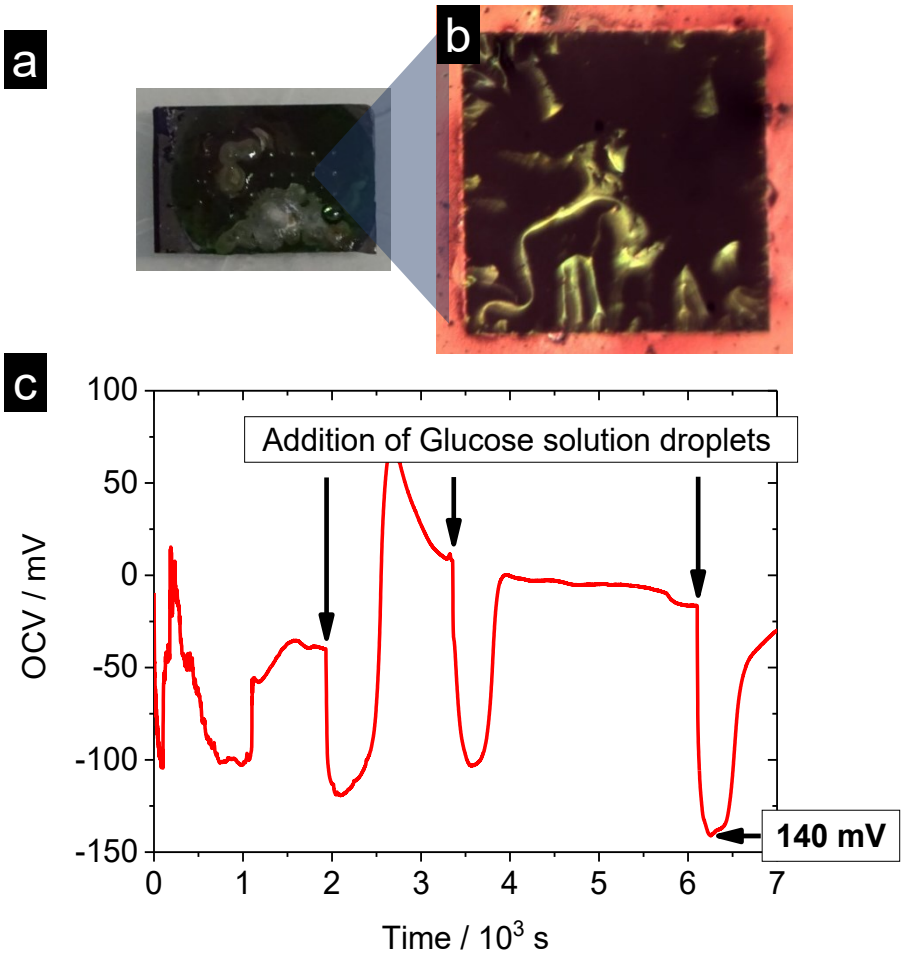

Figure 3.10 Pictures and OCV of a preliminary ceramic-electrolyte glucose fuel cell. a) Post-mortem optical photograph of the first successfully assembled glucose fuel cell chip with free-standing glucose fuel cell membranes. b) Optical micrograph of an individual free-standing membrane device functioning as a ceramic glucose fuel cell. c) OCV profile of the glucose fuel cell, where each sharp peak in the voltage corresponds to the addition of a droplet of glucose solution to the surface of the fuel cell device. OCV peaks are negative due to the polarization of the measurement. A peak OCV of 140 mV was observed, verifying the electrochemical activity of the ceramic glucose fuel cell chip.

3.8.2 OCV Measured in Liquid Flow Case

After verifying that the ceramic-electrolyte glucose fuel cells exhibit an appreciable OCV when glucose is supplied to the top electrode, and the bottom electrode is exposed to air, more controlled and systematic studies were performed. A next step along this incremental process was to perform OCV measurements of glucose fuel cells in the custom designed flow case, and to use more controlled sample geometry to allow for proper sealing. In this campaign, glucose solution with a glucose concentration of 1 M was flown over the top surface of the glucose fuel cell chip, which was placed inside the enclosure depicted in **Figure 3.8 a and b**, and the glucose fuel cell chip featured fully dense Pt electrodes that covered the entirety of the top and bottom sides of the chip, respectively. The OCV of the fuel cell chip was tracked using a source measurement unit (SMU). The OCV signal as a function of time of such a measurement is displayed in **Figure 3.11**. During the first 2 minutes, marked in blue, pure water was flown over the glucose fuel cell chip, and no significant OCV was detected. Then, the liquid supply flow was switched to glucose solution, marked in yellow, and a jump in the observed cell voltage can be observed. The OCV reached a peak value of 57 mV, indicating electrochemical activity of the fuel cell system. Subsequently, the liquid flow was returned to pure water, marked in blue. After an initial rapid decay of the OCV, the voltage signal oscillated widely, which we attribute to electromagnetic noise interfering with the wiring. Overall, the voltage decayed to -10 mV, likely due to a lack of reference, but the trend shows that after removal of the glucose solution, the fuel cell's activity ceased. This verifies that the glucose solution was in fact the source for the observed OCV. After about 5 minutes of measurement, and after crossing the 0 V line, the signal suddenly dropped and oscillated rapidly, indicating that the fuel cell failed at this point due do a membrane breakage. However, despite this eventual device failure, this experiment successfully verified the glucose fuel cell activity and further verified that the observed activity stemmed from the supplied glucose-containing fuel.

3.9 Conclusion

After recently demonstrating the successful proof-of-concept of the ceramic-electrolyte glucose fuel cell, we here detail the design choices and development steps that enabled this successful demonstration. To achieve this proof-of-concept, various methods, including a device fabrication pathway and electrochemical characterization protocols, as well as dedicated testing equipment were developed. We successfully developed a dedicated microfabrication route and optimized the processing of all glucose fuel cell components, i.e., both electrodes and the electrolyte, achieving a very high overall fabrication yield of 99 % across 180 devices. This is particularly remarkable given the fragile nature of the ceramic free-standing membrane system with a thickness of less than 400 nm.

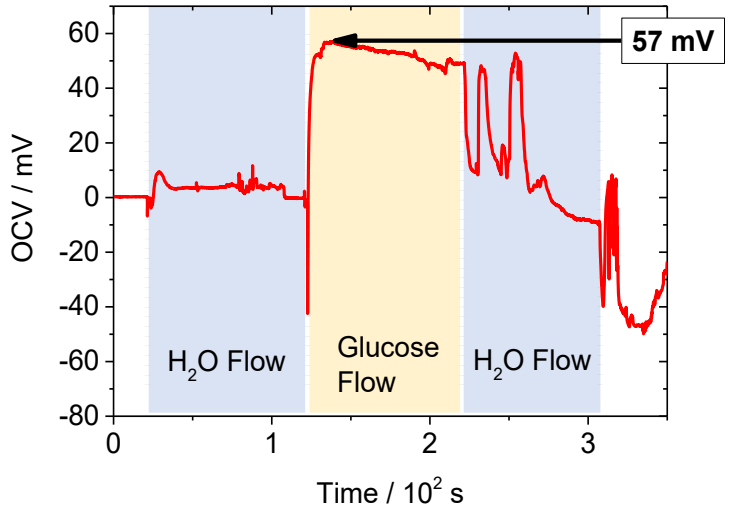

Figure 3.11 OCV measurement of a preliminary glucose fuel cell placed inside the custom-made flow case. Blue regions correspond to the flow of pure water, and the yellow region corresponds to the flow of glucose solution in PBS. The OCV reached a peak value of 57 mV after the fuel supply was switched to glucose solution, and decays to -10 mV after switching back to pure water. This verifies that the glucose solution is the source of the observed OCV. The device failed after 5 minutes.

Two chip layouts are presented, the *alpha* and *beta* designs, which served the purpose to first contact 36 glucose fuel cells simultaneously in the *alpha* design, and then contact individual membranes in the updated *beta* version. Contacting individual membranes posed a significant challenge given the high degree of miniaturization of devices with an area of 300 µm × 300, as well as the risk to rupture the thin membranes through the contact needles. A custom characterization setup needed to be designed to perform electrochemical performance characterization measurements on the ceramic-electrolyte glucose fuel cell. This included the design and manufacturing of both a flow case housing the fuel cell during operation under liquid fuel supply, as well as the peripheral test rig including liquid and gas handling, heating, and electrical wiring. The flow case was enhanced in a way such that 30 individual glucose fuel cells could be rapidly characterized within minutes for electrochemical characterization, which also constitutes a significant advancement in testing capabilities compared to earlier micro solid oxide fuel cell characterization setups. This setup was instrumental in enabling the collection of performance statistics over 150 individual ceramic-electrolyte glucose fuel cell devices as previously reported. Collectively, this work demonstrates the significant progress made from the first initial assembled devices and design contacting an array of glucose micro fuel cells on chip, up to testing individual functioning glucose fuel cells. This founded the basis for a high statistical electrochemical fuel cell evaluation that led to the first report on the successful operation of novel ceramic electrolyte glucose fuel cells with a peak power density of 43 µW cm^{-2} as

recently reported.[130] More broadly, this work can serve as a blueprint for the successful development of glucose fuel cells and the design of corresponding testing apparatus, beyond the specific ceramic-electrolyte glucose fuel cells discussed here.

4. Chapter 4: Careful Choices in Low Temperature Ceramic Processing and Slow Hydration Kinetics Can Affect Proton Conduction in Ceria

Adapted from P. Simons*, K. P. Torres*, J. L. M. Rupp. Careful Choices in Low Temperature Ceramic Processing and Slow Hydration Kinetics Can Affect Proton Conduction in Ceria. *Advanced Functional Materials* **2021** *(accepted)*.

*) The authors contributed equally to this work

Chapter Abstract

Low-temperature ceramic proton conductors such as ceria are important for applications ranging from sensors and resistive switches to new devices like implantable solid-oxide glucose fuel cells. Spray pyrolysis offers a promising fabrication route for proton-conducting ceria, with direct liquid-to-solid synthesis and control over crystallinity and grain size. To date, there are conflicting reports on ceria's proton conduction mechanism, particularly whether the interior contributes to proton conduction or transport occurs exclusively along a surface water layer. In this work, proton conductivity is observed in sprayed ceria thin films at 125 °C and below. Post-annealed films exhibit higher conductivity than as-deposited films of $3.3 \cdot 10^{-5}$ S/cm at 25 °C, which is comparable to previous reports and ascribed to the increase in crystallinity and grain size by post-annealing. This indicates that the interior of ceria in fact contributes to proton conduction. Remarkably slow hydration kinetics of ceria are observed, with time-dependent conductivity equilibrating to $9.53 \cdot 10^{-6}$ S/cm after up to 76 hours. This implies kinetics may have suppressed proton conduction in previous studies, explaining the strong fluctuations in reports to date. Slow protonation kinetics must be considered when designing functional ceria ceramics e.g. in electrochemical bio-energy conversion, sensing or neuromorphic computing.

4.1 Introduction

Proton conducting ceramics define a plethora of functionalities for today's electrochemical devices in energy and information processing, ranging from protonic ceramic fuel cells (PCFCs),[48,50] sensors,[51–54] or memristors[55–59][55,136–139] to magnetic switches[60,61] for memories and neuromorphic computing. In particular, hydrated fluorite-structured oxides such as ceria or YSZ show promising proton conductivity at low temperatures, with the potential to be used in new types of low-temperature energy harvesting devices.[91] Recently, we have developed a new type of implantable glucose fuel cell based on free-standing ceria membranes as the proton-conducting electrolyte, demonstrating that this bio-compatible material class can open up new avenues to biomedical applications unattainable for other proton-conducting ceramics.[131] Hydration plays a key role in defining the electronic and ionic properties of many ceramics, and strongly impacts device performance parameters such as low-temperature proton conductivity in fluorites[62,79,81–83,87], as well as resistive switching behavior in $SrTiO_3$,[55–57], HfO_2[59] and Ta_2O_5[59], or magneto-ionic switching in a Gd_2O_3/CoO_x system[61]. To understand and guide the further development of proton-conducting ceramics, mechanistic insights are needed. Two aspects of proton conduction in low temperature ceramic proton conductors have been largely unexplored so far: First, the initial choices made for processing and the degree of intrinsic hydration and respective protonation level. And second, the kinetics of hydration from interaction with the ambience (or device operation environment), which largely control the proton uptake and the corresponding material equilibration times. Sensors and resistive switches rely on stable and reproducible behavior, so that only the switching pulse or sensing species affects the device response and not an uncontrolled conductivity change due to slow or poorly controlled hydration. Similarly, stable and long-term operation of fuel cells requires a stable, high electrolyte conductivity. Slow hydration kinetics can be prohibitive to these performance requirements, through high device-to-device and cycle-to-cycle variability due to the reliance on transient states instead of equilibria.

To give an overview over the wide range of ionic conductors used in the aforementioned applications, we summarize different classes of ionic conductors in **Figure 4.1 a**.[48,70,140–142] Displayed are typical ionic conductivity ranges as a function of device operating temperature for various materials, including intermediate temperature proton-conducting ceramics such as $BaZrO_3$ and low-temperature proton conductors such CeO_2 and YSZ. These low-temperature proton conductors offer advantages over state-of-the-art polymeric proton exchange membranes (PEMs), in particular for the integration into glucose fuel cells: ceria is non-toxic, can be easily thermally sterilized, can be processed *via* standard semiconductor manufacturing techniques, and offers greater mechanical and thermal stability than PEMs.[131] There has been a spur in research of low-temperature proton-conducting oxides such as CeO_2,[79,82–84]

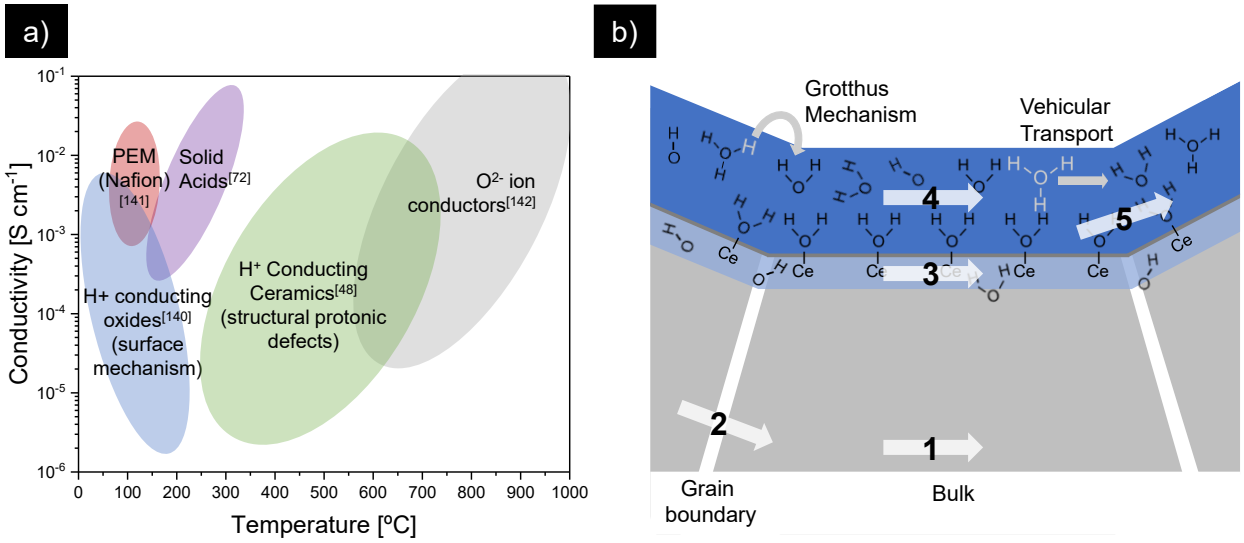

Figure 4.1 a) Ionic conductivity of various ionic conductors as a function of temperature.[48,72,140-142] **b)** Schematic of a hydrated ceramic showing the two types of proton transport mechanisms: the vehicular mechanism in which hydroxyl or hydronium ions carry charge along the surface water layer and the Grotthus mechanism where protons hop between water molecules. Regions where proton transport occurs in the hydrated ceramic are shown as 1) bulk 2) grain boundary 3) proton enriched layer in the grain 4) surface of bulk 5) surface of grain boundary.

YSZ,[81,86,87,143,144] and TiO_2[145] in recent years, driven by the drive toward new low-temperature fuel cells, as well as effective resistive switches and sensors. The measured proton conductivity of these materials ranges from 10^{-3} S/cm for gadolinia-doped CeO_2 at 25 °C[83] to $9 \cdot 10^{-6}$ S/cm at 25 °C for YSZ[81] and 10^{-3} S/cm at 30 °C for TiO_2[145]. In these materials, various modes of proton transport can contribute to the overall conductivity in this low temperature range, see schematic in **Figure 4.1 b** and Refs. [79,83] for further details. In general, the transport of protons can be classified by either *i)* the *regions where proton transport occurs* of the ceramic and its microstructure (e.g. surface, grain boundary, etc.) or *ii)* by the *mechanism by which protons are transferred* spatially within and between these regions.

i) Classification by regions where proton transport occurs: Proton conduction has been proposed to occur *via* the grain or grain boundary in the interior of the ceramic (modes 1 and 2 in **Figure 4.1 b**, respectively) or within either an enriched water layer near (mode 3) or an adsorbed water layer above its surface (modes 4-5, **Figure 4.1 b**). Within this water layer, one can in turn separate the contributions from the surface above the bulk (mode 4) and the surface above the grain boundary (mode 5).

ii) Classification through mechanism by which protons are transferred: Here, two mechanisms have been shown to dominate proton transport: Firstly, a Grotthuss-type mechanism[92] where protons hop from water molecule to water molecule along the surface or from protonic defect site to protonic defect site within the ceramic interior. Secondly, a vehicular mode where hydroxyl and hydronium ions move and thereby transport charge, within a water layer at the surface of the ceramic.

Dependent on the ceramic and its structure, different contributions may be dominant to the H^+-conduction. Specifically, for fluorite structure-type oxides such as pure and doped variants of ceria and zirconia, there is a debate whether the water layer adsorbed to the surface dominates or whether grain boundary transport through the ceramic interior also plays a role in the observed proton conductivity at low temperature: *i)* it has been proposed that proton conduction exclusively occurs *via* the surface water layer along pores and cracks in the surface.[79,81,83] In particular, Gregori *et al.*[83] observed that an enhancement in conductivity under moist air only occurred in porous films and not in dense films, concluding that low temperature proton conduction occurs along adsorbed water in the residual pores and cracks in the film. *ii)* On the contrary, other reports in thin films as well as pellets demonstrate that the interior, predominantly grain boundaries, contributes to proton conduction in fluorites.[84–87] This includes a study by Oh *et al.* that demonstrates orientation dependence of proton conductivity,[84] contradicting conduction in an isotropic water layer, as well as studies on dense YSZ pellets with a polymeric capping layer, preventing the formation of a conducting surface layer.[87] These reports demonstrate the contribution of grain boundaries to proton conduction and contradict the model *i)* where only the surface contributes to proton conduction in ceria and YSZ. In summary, it remains unclear which mechanism of proton conduction dominates under which exact conditions, and the literature indicates that a solely surface-dominated description fails to fully explain enhanced low-temperature proton conductivity in fluorite-type oxides.

A second challenge in the field of proton-conducting oxides is the uncertainty of how the processing and fabrication routes of the ceramics affect the degree of protonation, and thereby effectively the proton conductivity. For instance, fabrication routes of ceria vary widely throughout reports on proton conduction to date, ranging from solution-based processing and sol-gel methods to vacuum based techniques, and frequently involve thermal annealing or sintering steps. Here, processing techniques that would allow to control and possibly increase the initial protonation level of ceramics during the manufacturing process would be beneficial. However, this discussion has yet to start. The potential benefit of such studies can be exemplified by considering the effect of processing temperature and densification on the protonic defect density. For instance, ceria pellets require sintering temperatures upwards of 1200 °C to densify the ceramic from pre-made powders. At this temperature organic residues, hydration and protonic defects are effectively removed. In contrast, thin films deposited *via* spray pyrolysis are deposited at much lower temperatures,

between 200 °C and 500 °C, resulting in residues from the organic precursor as well as control over the degree of crystallinity and grain size. Thus, the question arises whether it is possible to use rational ceramic processing techniques during the synthesis to enhance the overall proton conductivity.

There are some first indications in literature that initial processing choices may indeed affect the degree of protonation and resulting proton conductivity. Gregori *et al.*[83] employed spin coating, through use of cerium nitrate dissolved in an organic precursor, to deposit porous ceria films, and these films were compared to thin films deposited *via* pulsed laser deposition. A difference of conductivity between the PLD-deposited and spin coated samples was attributed to the difference in porosity, however, differences in film processing chemistry and the resulting impact on protonation were not further discussed. Scherrer *et al.* similarly found that in YSZ, differences in protonic conductivity can be attributed to differences in the porosity of the samples, when comparing a variety of differently processed films ranging from spray pyrolysis and PLD to aerosol-assisted chemical vapor deposition, as well as pressed and sintered pellets and commercial tapes.[144] In addition, the data indicates a trend that samples prepared at lower temperatures and with smaller crystallite size show a higher protonic conductivity, which was also observed by Shirpour *et al.*[82] Remarkably, Scherrer *et al.* describe that some residual precursor solution from the spray pyrolysis deposition is still present in some films and affects the conductivity. Also, they observe that biphasic amorphous-crystalline films tend to have a higher protonic conductivity than their fully crystalline counterparts and a fully amorphous sample shows a protonic conductivity that lies along the average of all their presented data.[144] All this indicates that the sample fabrication route, processing temperature, sample crystallinity, and synthesis chemistry may affect proton conductivities. Despite these singular reports, it remains unresolved whether low temperature manufactured amorphous phases of ceria or zirconia exhibit significant proton conductivity. This motivates this present study to explore low temperature processing routes, specifically spray pyrolysis, and understand the relationship between structure and protonic transport behavior in the model ceria system. Ultimately, we see the perspective that by understanding these fundamental transport properties better, this may contribute to an effort of designing proton-conducting ceramics towards novel energy conversion devices, sensors or resistive switches. By investigating the in-plane conductivity of ceria thin films deposited *via* spray pyrolysis as a model system, we explore the hydration kinetics of ceria and the impact of the processing route and microstructure on proton transport behavior. This work does not aim to reproduce previous in-depth structure and crystallinity studies of sprayed ceria,[146–150] but rather aims to shed new light into how thermal processing, microstructure, and extremely slow hydration kinetics impact proton conductivity in ceria thin films. It provides new insights towards the open questions on the mechanism of proton conduction in ceria and how it can be controlled through processing and experimental design.

4.2 Results and Interpretation

4.2.1 Microstructure and Phase Analysis

Ceria thin films were deposited at 305 °C by spray pyrolysis and we compare an as-deposited film and another after post-annealing at 500 °C to investigate the effect of thermal processing and microstructural evolution on proton conductivity. We turn to microscopy to examine the film deposition for ceria *via* spray pyrolysis. **Figure 4.2 a** shows a top view optical micrograph of the as-deposited thin film. The observed color pattern with droplet feature sizes on the scale of microns stems from the droplet-by-droplet type deposition of the spray pyrolysis process itself, and are in agreement with other reports.[151] The SEM top view micrographs and optical microscope images in **Figure 4.2** confirm that smooth, on the scale of microns, ceria thin films were deposited with the spray pyrolysis technique independent of the post annealing. The thickness of the films as measured *via* profilometry was 490 ± 60 nm, immediately after deposition. The as-deposited film is crack free, and the post-annealed film showed a very low crack-density (see S.I.), stemming from bubbles of precursor evaporating during the post-annealing process. Judging by the small size, local nature and low overall occurrence of cracks, they do not affect the electrochemical results presented here. **Figure 4.2 d** shows the X-ray diffraction (XRD) patterns of ceria films as-deposited and after being post-annealed at 500 °C, respectively. Peaks corresponding to the (111), (200), and (220) Miller indices are present, confirming the fluorite crystal structure of ceria, and a sharp silicon substrate peak is observed at $2\theta = 33°$. No preferred orientation can be determined and there are no detectable changes in peak position between the post-annealed and as-deposited films. Using the Scherrer equation on the (111) peak, grain sizes are estimated to be on average 3.8 nm and 2.4 nm for the post-annealed and as-deposited sample, respectively. Small grain sizes obtained from XRD analysis explain why distinguishable grains were not visible in SEM micrographs. Significant peak broadening of the ceria peaks can be observed, with full width half maximum peak values for the (111) peak of 2.13° for the post-annealed film and 3.39° for the as-deposited film, in addition to a weak overall signal. Data extrapolated from Ref. [146] indicates that the post-annealed film is more crystallized: the Johnson-Mehl-Avrami-Kolmogorov (JMAK) analysis[152,153] from the reference determines that a 5 h post-anneal at 500 °C fully crystallizes amorphous ceria thin films, if dispersed seed crystallites are present. The dispersed seed grains do exist as can be seen from the presence of ceria peaks in the XRD pattern. According to the same analysis, the as-deposited film remains largely amorphous with small, dispersed crystallites. This is confirmed qualitatively by XRD since the post-annealed film shows narrower and more intense peaks than the as-deposited film. However, the XRD data obtained remains inconclusive in quantitatively confirming the fraction of crystallized material, as the overall peak areas are suppressed too strongly for a quantitative analysis of active X-ray scattering

volume. Overall, we conclude that thermal post-annealing increased the crystallized fraction as well as the grain size compared to the as-deposited film, and the influence of these properties on the ionic conductivity will be probed in the following.

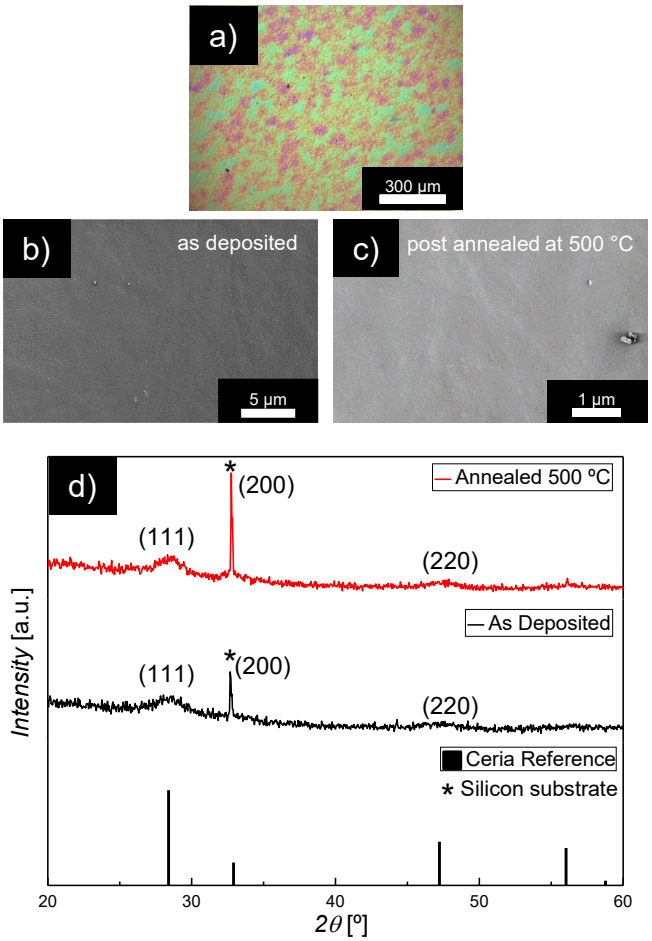

Figure 4.2 a) Optical micrograph of the as-deposited film, deposited via spray pyrolysis. **b-c)** Top view scanning electron micrograph of the as-deposited **(b)** and the post-annealed film **(c)**, confirming that smooth, dense, thin films were deposited. **d)** X-ray diffraction patterns of the as-deposited (black) and post-annealed (red) films with fluorite structure ceria reference for comparison (black). As films are annealed, peak width decreases, and intensity increases as a result of increasing grain size and crystallinity.

4.2.2 Temperature-dependent Impedance under Dry and Moist Air

Impedance measurements of the biphasic, as-deposited ceria film were taken from 25 °C and 400 °C in both, dry and moist atmospheres. The film was heated at a rate of 10 °C/min with a 90 second stabilization time at each temperature prior to each impedance measurement. To assure equilibration, films were held

under moist air for 21 hours at 25 °C (P_{H2O} = 0.027 atm) prior to temperature dependent moist air impedance measurements. Impedance data was fit using an equivalent circuit composed of three parallel RC circuits in series, representing bulk, interface, specifically grain boundary and amorphous-to-crystalline interfaces, and electrode impedance contributions. **Figure 4.3 a** shows the Arrhenius plot of the extracted conductivities from impedance measurements, and **Figures 4.3 b and 4.3 c** show exemplary impedance spectra at 25 °C and 50 °C, and at 400 °C, respectively.

Conductivity measured in dry air and moist air follow Arrhenius type behavior above approximately 150 °C, and in dry air, is only measurable above this temperature; in contrast, we clearly observe increasing conductivity with decreasing temperature below 150 °C under moist air. At 25 °C under moist air, total conductivity (σ) was $7.95 \cdot 10^{-6}$ S/cm and a single compressed impedance arc with a peak frequency of 2.00 Hz and a low frequency tail is observed, as shown in **Figure 4.3 b**. This arc indicates one dominating transport mechanism, however, there are conflicting reports on the exact interpretation, which we mostly extract from sparse reports on the case of doped zirconia: For example, a study on the impedance of YSZ showed that in moist air proton conductivity takes place along grain boundaries, bypassing the bulk, yielding a single arc, while at higher temperatures oxygen ions are conducted through the bulk and grain boundaries resulting in two arcs.[86] Another report on the conductivity of dense nanocrystalline YSZ films concluded that the single semicircle arc in moist air correlates to surface proton conductivity.[143] From these impedance results alone, we cannot distinguish whether the single arc is a result of proton conduction within ceria or a surface conductivity mechanism, however we can conclude that protons are the dominating conducting species based on the moisture dependence in this temperature region. At temperatures from 300 °C to 400 °C in both dry and moist air, two distinct arcs are observed, corresponding to grain bulk and transport across interfaces within the ceria film, namely interfaces between the crystallites and the amorphous matrix, and where developed, grain boundaries (**Figure 4.3 c**).

After impedance contributions are assigned, we now analyze the evolution of conductivity over the different temperature regions for the as-deposited film measured in dry and moist atmospheres. **Figure 4.3 a** shows two distinct regions of different conduction behavior, referred to as Regions I and II as specified in **Figure 4.3 a**. In Region I, within the temperature range of roughly 150 °C to 400 °C, we observe an Arrhenius-type behavior of thermally activated conductivity, with activation energies of 0.96±0.06 eV and 0.91±0.17 eV in dry and moist air, respectively, and a maximum conductivity of $1.64 \cdot 10^{-4}$ S/cm at 400 °C in dry air.

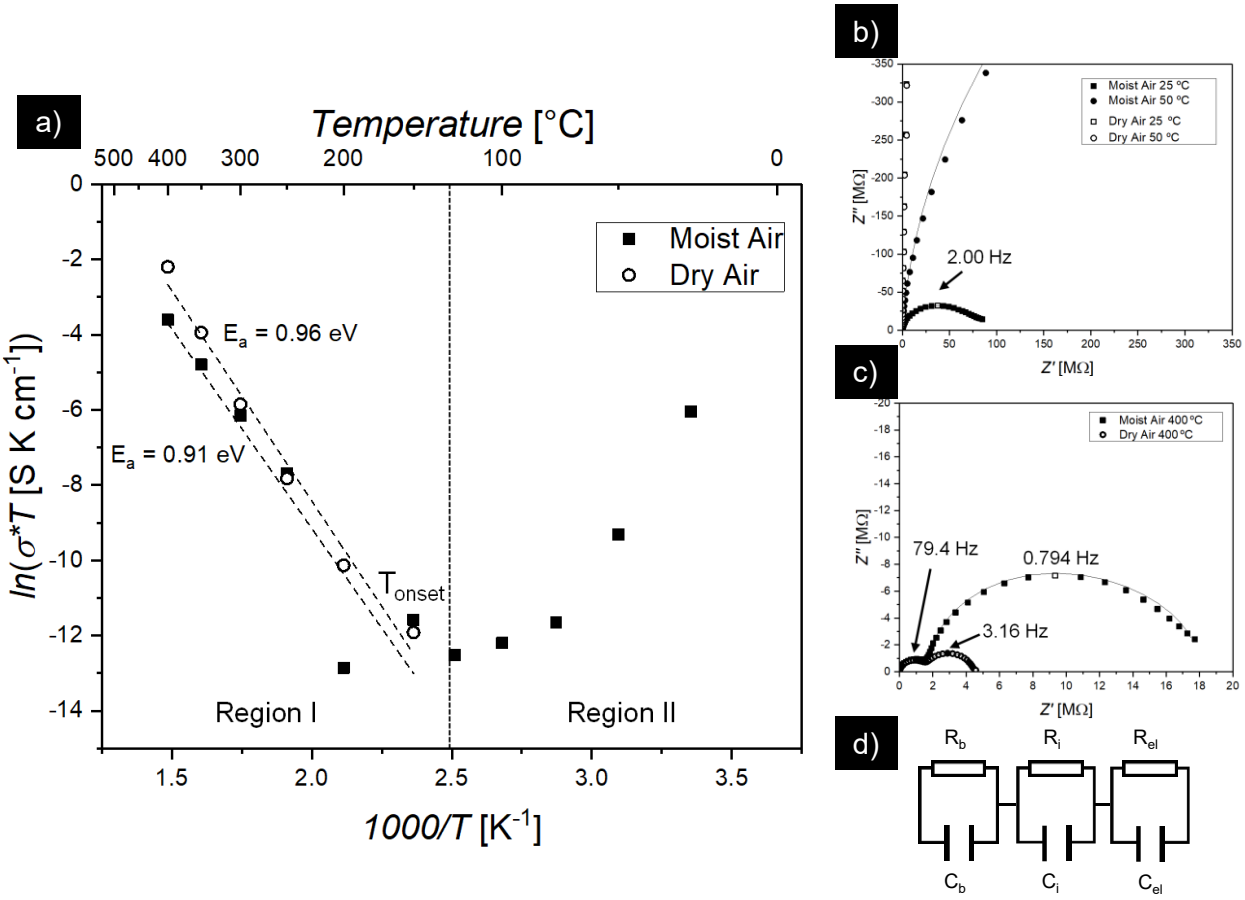

Figure 4.3 a) Arrhenius plot of extracted conductivities from impedance measurements taken in dry and moist atmospheres for the as-deposited film. Two temperature regions are shown: Region I with Arrhenius-like conduction behavior indicating oxygen ion conduction, and Region II with increasing conduction for decreasing temperature indicating proton conduction. In Region II, dry air conductivity was below the detection limit of the impedance bridge used and hence not seen in the plot. **b-c)** Exemplary impedance spectra under moist and dry air at low (25 °C and 50 °C) and high (400 °C) temperatures, respectively, with peak frequencies labeled. **b)** At low temperatures under moist air, a compressed impedance arc is observed, attributed to proton conductivity. **c)** At higher temperatures under both dry and moist air, two arcs are observed, with the low frequency arc attributed to oxygen ion conduction along the interfaces within the film and the high frequency arc to oxygen ion conduction through the grain bulk. **d)** Equivalent circuit used for fitting impedance spectra, representing grain bulk, interface (grain boundary and amorphous-to-crystalline interfaces), and electrode impedance contributions.

Reported activation energy errors correspond to the linear fit error of the Arrhenius trend in Region I. These values of the activation energy are in good agreement with those of the total apparent conductivity of ceria observed in literature[154], indicating that oxygen ionic transport is the dominant conduction mechanism in

this temperature range. However, inspection of the high temperature impedance spectra leads to interesting observation: In **Figure 4.3 a** it can be seen that the conductivity at the highest temperatures at and above 300 °C differ significantly between the moist and dry case, with a difference of over an order of magnitude at 400 °C. Turning to the underlying impedance data in **Figure 4.3 c**, it is found that the lower frequency arc of the measurement under dry air at 400 °C is significantly smaller than under moist air. Specifically, the extracted resistance of the low frequency arc in the dry case is 2.8 MΩ and in the moist case is 16 MΩ. This arc can be assigned to the contribution of conduction of oxygen ions across interfaces within ceria.[86] In the case of the ceria thin films presented here, these interfaces are both grain boundaries and amorphous-to-crystalline interfaces. This difference in cross-interface conductivity is remarkable, as it shows that moisture is suppressing the oxygen ion conductivity across grain boundaries. This is in agreement with a study by Chueh *et al.*,[155] where it was found that the oxygen ion conductivity across grain boundaries in samarium doped ceria decreased under moisture, over the temperature range of 250 °C to 450 °C. Chueh *et al*. argue that hydration causes an increase in space charge potential within grain boundaries, resulting in the depletion of oxygen ions in grain boundaries and therefore lower ionic conductivity.

In Region II, at temperatures below 150 °C and only in moist air, the conductivity increased with decreasing temperature, indicating protonic conductivity due to hydration of the ceria film. This behavior, with an apparent negative activation energy of the ionic conductivity, is similar to what was observed in previous studies in literature on polycrystalline ceria thin films,[83,84] ceria pellets,[79,82] and YSZ pellets[81]. The negative activation energy of this process can be interpreted by two competing kinetic processes occurring simultaneously: thermally activated ionic conductivity, yielding lower conductivities at lower temperatures, competes with increasing water adsorption at lower temperatures, which increases the amount of water in the system and thereby the amount of available charge carriers. In dry air and within Region II, the ionic conductivity was below the detection limit of the impedance bridge used, as exemplified by the impedance spectra at 25 °C and 50 °C in dry air, shown in **Figure 4.3 b**.

Interestingly, the onset temperature T_{onset} of proton conductivity observed here differs from other studies, which we exemplify for the fluorite structured oxides ceria and YSZ to have enough data points of comparison. In this work, moist air conductivity begins to diverge from the dry air values at 125 °C, indicating the transition to proton conductivity. As summarized in **Table 4.1**, for porous and polycrystalline films and porous pellets of ceria and YSZ, moisture dependent proton conductivity was observed at T_{onset} as high as 300 °C[83] and 400 °C[79] respectively and for dense films, low temperature proton conductivity under moist air has been reported with T_{onset} below 50 °C.[83,143] We consider this as an important observation since the unusual onset temperature of 125 °C when compared to other studies may be a result of the amorphous-crystalline biphasic nature of films synthesized in this work. Proton conduction mechanisms

for a film with an amorphous phase fraction likely differ from a fully crystalline film or pellet, due to two main reasons: first, there are by processing nature more organic residues and OH groups present as space fillers in the local network arrangement of the ceria bonding units. Second, the formation of a local bonding unit network of the amorphous state may be able to accommodate more OH-groups due to increased available volume when compared to any crystalline state, increasing the effective protonation. Third, we also attribute this strong fluctuation of proton conductivity onset temperatures to the microstructure: proton conductivity is influenced by the degree of porosity and the grain boundary density. Here, we characterized mostly dense films in the SEM micrographs (**Figure 4.1**), however since it has been suggested that low temperature proton conduction occurs along water adsorbed through open pores and cracks, the proton conduction temperature range likely depends on the degree of porosity. The onset temperature of proton conduction was lower than previous reports of more porous samples and higher than fully dense samples. It is worth noting that an explanation for the low onset temperature in dense samples so far was that only liquid water on the surface contributes to this conductivity. The findings here contradict this, and a reason for not seeing protonic conductivity in the bulk at higher temperatures could lie in slow hydration kinetics: samples simply take too long to fully hydrate and show appreciable conductivity within the measurement times of previous studies.

T_{onset}	Material and Synthesis Method	Highest Processing Temperature	Microstructure	Reference
300 ºC	Spin coated CeO_2 film	600 ºC	Porous	[83]
400 ºC	Calcinated CeO_2 pellet	1000 ºC	Porous	[79]
<350 ºC	Chemical vapor deposition CeO_2 film	500 ºC	Columnar, porous	[84]
~400 ºC	Sintered CeO_2	800 ºC	93% Dense	[82]
<50 ºC	Pulsed laser deposition CeO_2 film	720 ºC	Dense	[83]
<50 ºC	Spark plasma sintered YSZ film	1050 ºC	Dense	[143]
125 ºC	Spray pyrolysis CeO_2 films	305 ºC	Dense	*This work*

Table 4.1 Proton conductivity onset temperatures reported from literature for fluorite-structured oxides with varying synthesis methods, processing temperatures, and microstructures. The onset temperature in this work varies from previous studies due to differences in microstructure, crystallinity, and processing conditions.

4.2.3 Time-dependent Proton Conductivity

To further explore this hypothesis, we analyzed the low temperature conductivity of sprayed ceria films over time. Time-dependent impedance measurements were taken at 25 °C for the as-deposited sample to determine the equilibration time of the protonic conductivity of ceria thin films under moist air. **Figure 4.4 a** displays the impedance reported as Nyquist plots: one measurement was taken in dry air, and immediately afterwards, the atmosphere was switched to moist air. Under moist air, the impedance was monitored over a period of 5.5 hours. We observed that the conductivity continuously increased over the first 5 hours of this measurement campaign, and then stabilized between 5 and 5.5 hours to $\sigma = 4.8 \cdot 10^{-7}$ S/cm with impedance yielding a half semicircle. Subsequently, over the next 23 hours, the sample was subject to two heating and cooling cycles, where the sample was heated to 400 °C and then cooled back to 25 °C, all under moist air. This heating program served to simulate the Arrhenius-type measurement campaign. The sample was then held again at 25 °C with $\sigma = 4.03 \cdot 10^{-6}$ S/cm immediately after heating, and **Figure 4.4 b** shows the electrochemical impedance over 74 hours after heating. Remarkably, it took 47.5 hours after the heating cycle for the sample to stabilize to around $9 \cdot 10^{-6}$ S/cm indicating extremely slow hydration kinetics of the ceria films. To better visualize the time scale, we are reporting the total conductivity as a function of time in **Figure 4.5**, as extracted from the impedance measurements. **Figure 4.5 a** shows the entire measurement campaign, and **Figure 4.5 b** is a magnification of the period before the sample was exposed to heating. We have fitted an exponential profile to visualize the conductivity relaxation behavior over the reported time and that the equilibration is only reached at over 76 hours of exposure to moist air with a maximum conductivity of $9.53 \cdot 10^{-6}$ S/cm. To the best of our knowledge, such long equilibration times have not previously been reported and should guide further experimentation and interpretation of conductivity data of ceria.

The long equilibration time observed to reach steady-state proton conductivity may also explain the differences in our reported proton conductivity temperature range from literature (**Figure 4.3** & **Table 4.1**). As we show in **Figure 4.5 a**, equilibration of apparent conductivity can take up to three days, which means that the measurement protocol of the temperature-dependent impedance heavily influences the observed impedance, and data may not reflect true steady-state values. In addition, we want to point out that much of literature relies on reporting proton conductivity under constant “relative humidity”. Reporting relative humidity instead of water partial pressure leads to the following complication: relative humidity is a derived quantity that contains both the water partial pressure and the temperature. Relative humidity can be changed by changing water concentration, temperature, or both. In order to differentiate between the two competing thermodynamic driving forces of temperature and water vapor concentration (i.e., the water chemical potential), it is paramount to report those two values, instead of relative humidity. In particular, from

literature it is unclear whether measurements carried out at constant relative humidity and varying temperature mean that relative humidity was fixed at a reference temperature (which would mean that the water vapor concentration was in fact constant) or whether the actual relative humidity was kept constant, which means that both the temperature and the water vapor concentration were changed at the same time. The latter would make it impossible to separate the effects of temperature and water chemical potential, two competing driving forces which, as we indicated before, both strongly contribute to the total ionic conductivity in hydrated oxides.

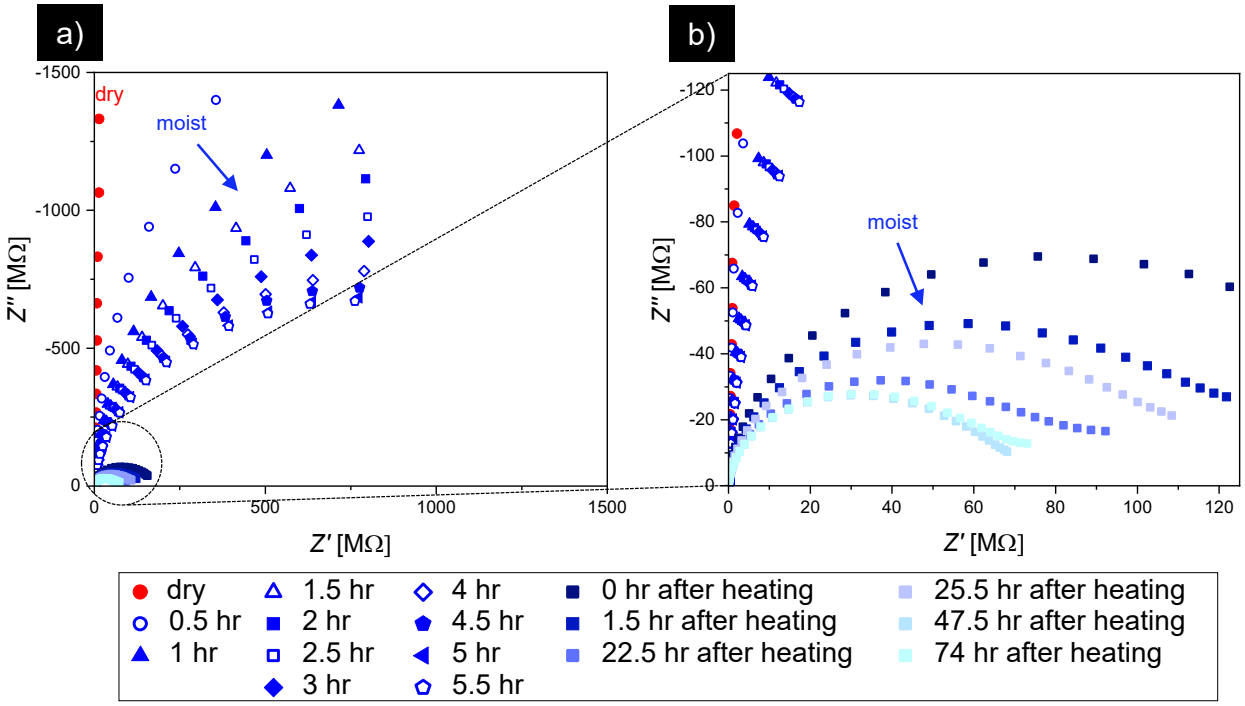

Figure 4.4 Nyquist plot of the as-deposited film starting under dry air (red) **a)** over 5.5 hours under moist air (blue) and **b)** over 74 hours after thermal cycling to 400 ºC under moist air (blue), revealing the long equilibration times and slow hydration kinetics: Proton conductivity initially stabilized after 5 hours under moist air, however after thermal cycling to 400 ºC, conductivity significantly increased and took an additional 47.5 hours to reach steady state.

4.2.4 The Influence of Thermal Annealing on Conductivity

We now turn to investigate more deeply the effect that thermal annealing has on the observed proton conductivity. From the data reported in **Figures 4.4 and 4.5**, it appears that the electrochemical impedance of as-deposited films stabilized after 5 hours of exposure to moist air at 25 °C, prior to the thermal treatment

of the sample. However, these data at least qualitatively also agree with the trend observed after the heat treatment, implying an equilibration time of up to 100 hours. This yields the question whether the total equilibration time was in fact that long, and the observed apparent equilibration after 5 hours was only an artifact of measurement noise, or whether the heat treatment affected the sample response by increasing total conductivity through microstructural changes and the measurement observing the relaxation into this higher conductivity state.

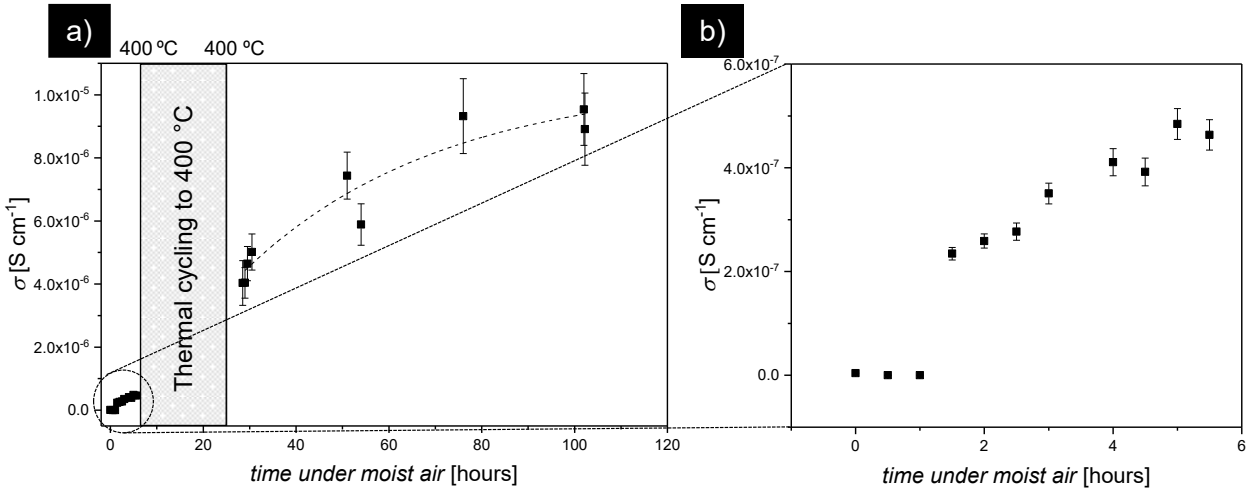

Figure 4.5 Conductivity of the as-deposited film as a function of time at 25 ºC **a)** over >100 hours under moist air and **b)** magnification of the first 6 hours under moist air, before thermal cycling to 400 ºC. After 76 hours of exposure to moist air (47.5 hours after thermal cycling) conductivity stabilized to a value of $9 \cdot 10^{-6}$ S/cm, showing the extremely slow kinetics of the equilibration process. An exponential relaxation was fitted to guide the eye.

To further elucidate this, we compared the electrochemical impedance data of the sample as it was deposited to a film that was deposited simultaneously, but subsequently post-annealed at 500 °C. This was motivated by previous studies of the crystallization and grain growth kinetics of sprayed ceria thin films: Given the deposition temperature of 305 °C, the heating step to 400 °C likely led to further crystallization in the film, modifying the microstructure. However, this was impossible to verify on the same sample *via* XRD, since electrodes were already deposited on the sample for the electrochemical impedance study. Thus, a more controlled model experiment with a post-annealed sample was carried out to further investigate this.

Figure 4.6 compares the Nyquist plots of the post-annealed and as-deposited films under moist air, at 25 °C (**Figure 4.6 a**) and at 400 °C (**Figure 4.6 b**), respectively. We find that the total conductivity is about one order of magnitude higher for the post-annealed film, when compared to the as-deposited one ($\sigma_{annealed}$ = $3.3 \cdot 10^{-5}$ S/cm and $\sigma_{deposited} = 9.5 \cdot 10^{-6}$ S/cm at 25 °C, $\sigma_{annealed} = 1.1 \cdot 10^{-4}$ S/cm and $\sigma_{deposited} = 4.0 \cdot 10^{-5}$ S/cm at 400 °C).

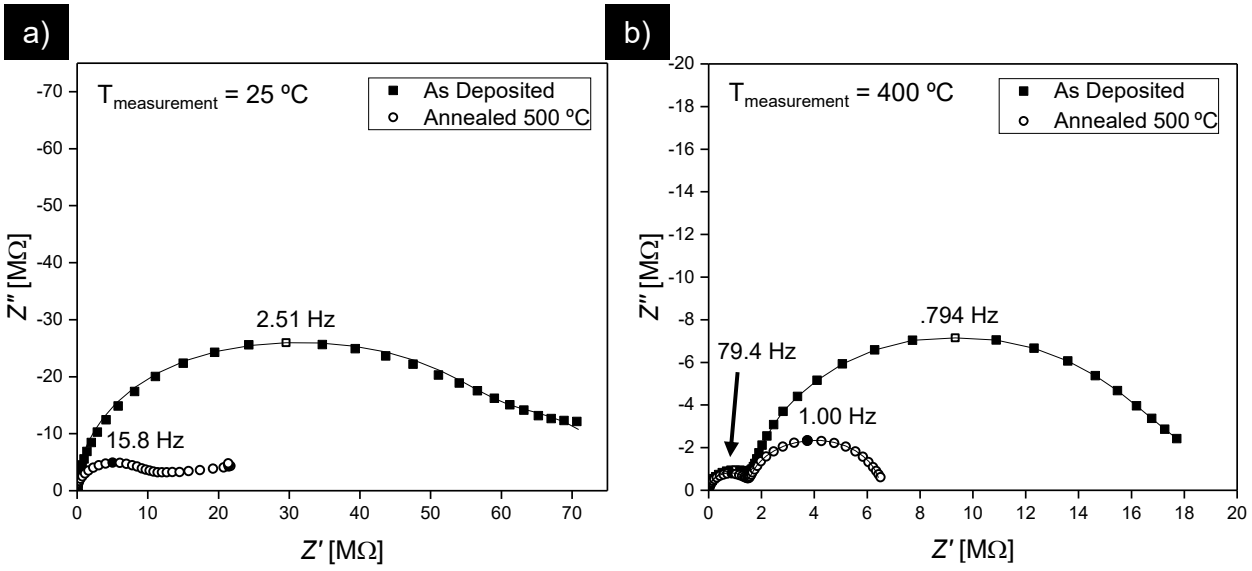

Figure 4.6 Nyquist plot with maximum frequencies of as-deposited and post-annealed films at **a)** 25 ºC under moist air and **b)** at 400 ºC under moist air with peak frequencies labeled. Annealing increases both the proton conductivity at low temperatures and the overall oxygen ion conductivity at high temperatures by approximately one order of magnitude which is explained by a change in interface density and amorphous-to-crystalline ratio caused by annealing the film.

We ascribe this stark difference in protonic conductivity at 25 °C, **Figure 4.6 a**, to the difference in amorphous-to-crystalline ratio between the as-deposited and post-annealed films, which was observed by XRD in this study and has been extensively studied in the past. Importantly, the discussion presented here does not serve to recreate previous thorough crystallinity studies on ceria deposited *via* spray pyrolysis[146–150], but rather to investigate the impact of the known structural properties of sprayed ceria films and of processing parameters in general on proton conduction. This model is schematically depicted in **Figure 4.7** and explained in the following. The amorphous phase of ceria is expected to generally have a lower overall conductivity than the crystalline phase, as in the free-volume model of amorphous solids, deep potential wells trap secondary charge carriers such as protons.[156,157] On the other hand, in crystalline fluorites, grain boundaries have been observed as the dominant transport pathway for proton conduction,[86,87] and in a similar fashion, the interface between crystalline grains and amorphous ceria is expected to have an

increased protonic conductivity. In **Figure 4.7**, the red paths exemplify low-conductivity pathways through the amorphous fraction, and the green paths exemplify the higher conductivity paths along grain edges and grain boundaries. The as-deposited film is largely amorphous and therefore has a low fraction of crystalline material, as well as a low and disconnected fraction of grain boundaries and amorphous-crystalline interface, **Figure 4.7 a**. In contrast, the annealed film is mostly crystalline, with larger nano-sized grains. Both higher crystallinity and larger grain size enhance the density of developed grain boundaries and amorphous-crystalline interfaces, **Figure 4.7 b**. From this, it can be inferred that for the post-annealed film, the higher fraction of crystalline material, with larger grains, increases the fraction of highly-conducting paths of the overall system, and therefore increases the total protonic conductivity of the ceria. If proton conductivity were purely dominated by a water film on the surface, and conduction within ceria were to play no role, we would not expect to see a significant difference in conductivity between the post-annealed and as-deposited films: the water film formation on the surface should remain unaltered by the annealing process. Therefore, enhanced conductivity along grain boundaries and similarly, along the interfaces of amorphous-crystalline ceria explains the enhanced conductivity in the post annealed film and supports previous reports that assign proton conductivity not just to a surface effect, but also to highly conducting grain boundaries within fluorites.

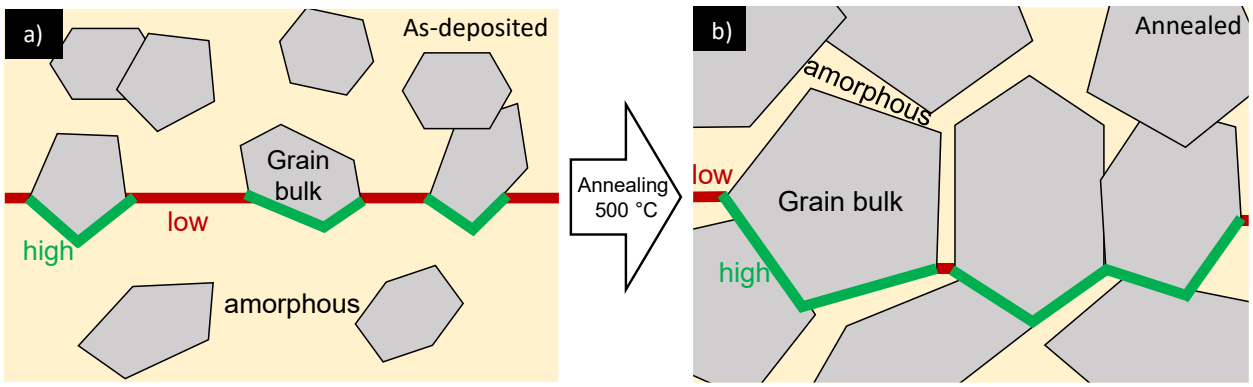

Figure 4.7 Room temperature proton conduction pathways for biphasic films **a)** as-deposited and **b)** annealed at 500 ºC. The lower conductivity pathway is through the amorphous phase (red) and the higher conductivity is along the amorphous-crystalline interface and grain boundaries (green). As films are annealed, grain size increases and the amorphous phase fraction decreases, increasing the amount of high conductivity paths and explaining the increase in the overall proton conductivity of annealed films.

Furthermore, the high temperature behavior in **Figure 4.6 b** supports this explanation: the two samples show largely identical behavior in the high frequency regime of the impedance spectrum. In contrast, the low frequency component of the as-deposited film has about a four-fold higher resistance. This data is in very good agreement with previous studies from Avila-Paredes *et al.*[87] and Kim *et al.*[86] In those studies,

the high frequency arc is assigned to bulk transport and the low frequency component is assigned to transport across grain boundaries. The noteworthy difference to these previous studies is that samples investigated here contain a significant fraction of amorphous ceria, whereas previous studies investigated fully crystalline samples. However, a largely analogous explanation can be employed: The high frequency arc is associated with oxygen ion conductivity through the bulk, and the low frequency arc is associated with oxygen diffusion across grain boundaries, or more generally interfaces. The post-annealed film has a larger crystalline-to-amorphous ratio as well as larger grains than the as-deposited film. Interestingly, the ratio of crystalline to amorphous ceria does not influence the bulk contribution of the conductivity. On the other hand, this ratio largely affects the low frequency regime, i.e. interface-governed conductivity. Here, the post-annealed film shows much higher conductivity, which is due to a lower density of interfaces (grain boundaries and amorphous-crystalline interfaces) across any given cross-section. Assuming that no new grains are nucleated, which is in agreement with previous JMAK analyses,[146] grain growth reduces the number of interfaces through which a charge carrier would need to pass. For fully isolated grains in an amorphous matrix, which can be expected for the as-deposited sample, each grain contributes two amorphous-to-crystalline interfaces. For connected grains such as in the post-annealed sample, two adjacent grains share an interface, and therefore, each grain contributes only one interface. This means that for the post-annealed film the total grain boundary resistance, i.e. the sum of all grain boundary resistances encountered by a charge carrier, is reduced. Lastly, we reason that the lower overall conductivity compared to literature can be attributed to the at least partially amorphous nature of the ceria thin films characterized here.

Collectively, we show that ceria films processed *via* a wet-chemical processing route such as spray pyrolysis at low temperatures exhibit proton conductivity under moist air at temperatures of 150 °C and below. This proton conductivity occurs along interfaces (grain boundaries and amorphous-to-crystalline interfaces) within the ceramic as well as along the surface, and we have successfully manipulated the conduction pathway through thermal annealing. In addition, the overall equilibration times observed in this study are much longer than previously reported, indicating that slow kinetics may have suppressed the observation of grain boundary conductivity in previous studies.

4.3 Conclusions

This work presents new insights into the proton conductivity of ceria, deposited *via* the wet chemical route spray pyrolysis. Our results shed new light onto the large fluctuation of observed proton conductivities in ceria and the role of a biphasic amorphous and crystalline configuration. This discrepancy of proton conductivities reported in literature may be explained by long stabilization times and slow sample evolution, since we observe equilibration times of up to three days. This can explain why some previous studies did not observe interior or cross-plane proton conductivity, while others did: proton conduction may have been kinetically suppressed due to the slow hydration kinetics uncovered here. In addition, our data shows that low temperature proton conductivity is dependent on crystallinity and grain size. This demonstrates that proton conductivity at low temperatures does not solely rely on a water layer adsorbed to the surface but includes grain boundary and amorphous-to-crystalline interface contributions.

Ceria served as the model system due to its single-phase nature and unusually high proton conductivity at low temperatures, in addition to the ability to control its microstructure through rational processing. Thin films of ceria were successfully deposited by spray pyrolysis as model systems to investigate the influence of hydration kinetics on proton conductivity in ceria. We purposefully selected a wet-chemical processing route to design the ceramics, being spray pyrolysis, in an effort to reach high hydration levels compared to more traditional processing techniques such as sintering of pellets or pulsed laser deposition. Through electrochemical impedance spectroscopy we detect increasing proton conductivity at decreasing temperatures of 125 °C and below in moist atmospheres, agreeing with what has been presented in literature on hydrated ceria.

An important finding is that film conductivity equilibration times under moist air at room temperature are up to three days long, indicating extremely slow hydration kinetics. This is even more surprising since ceria was present here in thin film form and one may even expect longer hydration equilibration times for bulk processed sintered pellets. To our knowledge, such results have not been reported, and we recommend future studies on the protonation of ceria and other metal oxides to consider the long equilibration times to ensure steady-state measurements.

Our work additionally demonstrates that thermal history plays a major role in sample conductivity. After heating films to 400 °C under moist air, conductivity significantly increased, which may be a result of the long equilibration times previously discussed or of microstructural changes in the sample caused by heating. To further study the effect of thermal treatment on conductivity, impedance measurements were taken for a 500 °C post-annealed and as-deposited film. The conductivity for the post-annealed film was higher than

the as-deposited and likely can be explained by the increase in degree of crystallinity and grain size with annealing.

One interesting observation from studies so far is that there are conflicting reports on the cross-plane conductivity of protons through dense ceria. Some studies have detected such conductivity, and even used it for concentration cells,[91] while in others, no proton conductivity through dense ceria was observed.[83] Our results can help explain this inconsistency in literature so far: hydration of ceria is a slow process, that can take days even for thin films, as we show here. In contrast, surface adsorption is a fast process which allows protonic conductivity along surfaces and through porous samples to occur quickly. This implies that cross-plane conductivity through sufficiently thick dense samples may be kinetically suppressed, explaining why some studies did not observe such conductivity through thick samples. Besides the slow kinetics observed in our measurements, this hypothesis is supported by a second observation: We observe that proton conductivity is significantly increased by the post-annealing process, meaning that modifications to the film itself (grain size, degree of crystallinity) in fact modified the proton conductivity. If proton conductivity were purely dominated by a water film on top of the ceria surface, and conduction within ceria were to play no role, we would not expect to see a significant difference in conductivity between the post-annealed and not annealed films: the water film formation on the surface should remain largely unaltered by annealing process. Since this is not the case, we conclude that we observe protonic conductivity through the film itself, which is dominated by grain boundary and amorphous-crystalline interface conductivity.

By showing that both thermal history and the slow kinetics of hydration play a significant role in the low temperature protonic conductivity of ceria, we have shed some light in the large scatter among conductivity data of ceria existent among earlier reports in literature. We have shown that equilibration even for thin films can be extremely slow, beyond reported experimental durations thus far and that the thermal history of the sample has to be taken into account when interpreting conductivity data. This expanded understanding is of relevance for the further development of technology based on the proton conductivity in ceria, such as implantable glucose fuel cells, and also adds to the understanding of systems where fast response and controlled behavior is key, such as sensors or resistive switching memory.

4.4 Experimental Methods

4.4.1 Sample Preparation

Cerium oxide thin films were prepared *via* spray pyrolysis with a precursor solution made up of 0.01 mol/l cerium nitrate (III) hexahydrate (99.9% purity, VWR international, USA) dissolved in 33:33:33 volume percent diethylene glycol monobutyl ether, 1- methoxy 2-propanol, and ethanol (all reagent grade chemicals with >98% purity from Sigma Aldrich, USA). The precursor solution was then fed into a spray gun (AG361, DeVILBISS, USA) at a 5.4 mL/hr flow rate and atomized into droplets with a 0.6 bar air pressure. Droplets were sprayed onto a heated Si_3N_4 coated (100) silicon substrate (1cm x 1 cm, supplier: Sil'tronix, France) for 287 minutes at a working distance of 30 cm between the spray gun nozzle and the substrate. The substrate was placed on a steel plate heated by a hotplate (VWR, USA) set to 350 °C. The surface temperature immediately before spraying, measured by a thermocouple placed on the substrate surface, was 305 °C. Where indicated, samples were post-annealed at 500 °C for 6 hours with a 10 °C/min heating rate (Nabertherm box furnace, Germany). Platinum electrodes with 0.5 mm x 7 mm dimensions spaced 0.25 mm apart were deposited via magnetron sputtering using a shadow mask (Kurt J, Lesker, USA; Pt target: 99.99% purity, ACI Alloys, USA).

4.4.2 Characterization

Electrochemical impedance spectroscopy measurements were taken with a Zahner IM6 potentiostat (Zahner-elektrik, Germany) at a frequency range of 1 MHz to 100 mHz at a 50 mV amplitude. Measurements were carried out in a temperature controlled Linkam heating stage (Linkam Scientific, UK) from 25 °C to 400 °C under either dry air (Ultra Zero grade, Airgas, USA) or moist air. Moist air measurements were executed by bubbling dry air through deionized water at room temperature to obtain a water partial pressure of 0.027 atm. Impedance data was subsequently analyzed and fit using an equivalent circuit model with 3 RC circuits in serial configuration, using the software ZView (Scribner Associates, USA). The cerium oxide film microstructure and thickness were analyzed by SEM (Zeiss Supra55VP Field Emission SEM). XRD measurements were carried out on ceria films using the Rigaku SmartLab diffractometer with Cu K_α radiation at a 40 mA current and 40 kV voltage to characterize the microstructure and determine cerium oxide grain size. The film thickness was determined via profilometry (Dektak 150, Veeco, USA).

5. Chapter 5: Deposition Parameters and Raman Crystal Orientation Measurements of Ceria Thin Films Deposited by Spray Pyrolysis

Adapted from P. Simons*, K. P. Torres*, J. L. M. Rupp. Deposition Parameters and Raman Crystal Orientation Measurements of Ceria Thin Films Deposited by Spray Pyrolysis. *Manuscript in revision (2021)*.

*) The authors contributed equally to this work

Chapter Abstract

Spray pyrolysis offers excellent control over microstructure and cost-effective processing of ceria ceramic thin films for many applications such as catalysis, solid oxide fuel cells, solar-to-fuel conversion, and resistive switching. To control the properties of ceria thin films that are relevant for such applications, such as crystal orientation, grain size, crystallinity, and to achieve crack-free deposition, systematic processing guidelines for sprayed ceria are needed. In particular, the crystal orientation of ceria plays a significant role in the catalytic activity of ceria, and therefore controlling and measuring crystallite texture for catalytic applications is highly relevant for catalysis. In this work, we systematically scan the parameter space of deposition and post-annealing parameters to control various mechanical and structural properties that impact film functionality. We identify a critical film thickness of ceria during wet-chemical deposition of 300 nm in the initial amorphous phase, due to the interplay of ceria crystallization, solvent evaporation, and thermal expansion. Through XRD, the transition from amorphous to the cubic crystalline phases and grain growth with annealing is observed. Furthermore, a thermally induced, prominent shift in texture from the [111] to [200] direction is detected, which corresponds to the {100} ceria facet of high catalytic activity. Interestingly, we observe that the peak position of the Raman F_{2g} stretching mode correlates with the measured texture coefficient and exceeds the bulk value of 465 cm^{-1} for highly textured films. While it has been previously observed that thermal annealing can induce stark texture in ceria thin films, we contribute with the new insight that Raman spectroscopy can be used to detect such texture. Overall, this offers a combination of cheap processing and simple characterization of the ceria crystal orientation.

5.1 Introduction

Ceria and its solid solutions have been researched extensively because of their wide variety of applications ranging from catalysis[158–160], solid oxide fuel cells[90,161] and thermochemical solar-to-fuel conversion[162–164], to resistive switching systems.[165,166] In order to engineer and improve the ceria system for these applications, ceria has been widely studied to obtain insights into its defect-chemical, mixed ionic-electronic transport, mechanical, and catalytic properties.[154,167,168] Ceria and its solid solutions have been studied in the form of thin films as defect model systems of mixed ionic-electronic conductors, as well as functional ceramic entities in energy and information devices.

Thin films have been demonstrated to differ in their electro-chemo-mechanics[169] from their bulk counterparts, exhibiting higher amounts of strain ascribed to interactions with the substrate[170,171], and chemical strain from changes in the lattice and their defect chemistry.[118] Also, it was reported that strain can impact their ionic and electronic conductivities, defect formation and association.[171,172] For example, free-standing ceria membranes have been investigated as a model system for micro solid oxide fuel cell membranes and the impact of local stress-strain fields on the oxygen ionic conductivity of ceria solid solutions was confirmed for device integration.[89,90] Other examples for electro-chemo-mechanic interactions have been demonstrated for gadolinia-doped ceria (GDC) with giant electrostriction[173,174], and their suitability as electrochemical actuators[175].

Besides strain affecting the defect chemistry, also the microstructure of ceria such as the grain size and grain boundary density, as well as crystal orientation play a critical role in controlling properties such as catalytic activity or conductivity. For example, nanocrystalline ceria exhibits dramatically higher electronic conductivity than bulk or microcrystalline ceria, due to size dependent grain boundary segregation of impurities.[176] Ceria surfaces with different orientations show different levels of catalytic activity, with (100) planes showing higher catalytic activity than (111) planes,[177] due to the more favorable energetics for oxygen vacancy formation on the open (100) surface when compared to the closed-packed (111) surface.[178] However, computational and experimental results so far largely indicate that the (111) plane is the lowest energy state, and therefore the preferred termination in randomly oriented powders as well as thin films.[179,180] Given the different catalytic activity of the different crystal terminations, it is important to be able to control the orientation of ceria during synthesis, and particularly to be able to do so at scale for commercial applications. There have been demonstrations of assembling ceria nanocrystals with controlled surface exposure, using hydrothermal synthesis.[181] Interestingly, multiple studies have furthermore shown that upon thermal annealing or deposition under relatively high temperature, texture can be induced into previously randomly oriented ceria, with a preference for the development of the higher energy (100)

plane.[182–186] These findings indicate that the thermodynamic description of the relative order of stability of the different ceria planes is incomplete. Ultimately, the ability to control the preferred ceria crystal orientation in a simple and scalable way is important in engineering ceria thin films for catalytic applications.

Given their relatively low cost and scalability, wet-chemical thin film deposition techniques for ceria and its solid solutions such as spray pyrolysis are advantageous in comparison with vacuum based techniques which often require more expensive and complex equipment.[88] Additionally, wet-chemical synthesis techniques typically require significantly lower processing temperatures often at one fifth to one sixth of the melting temperature (between 300 °C and 500 °C for ceria), and do not require sintering to densify as is common for pellet processing from powders. The ceramic wet-chemical synthesis method of spray pyrolysis offers good control over the microstructure[187] and a low-cost option to coat large areas with thin films at low temperatures. Unlike ceramic manufacturing routes that involve sintering of powder green bodies, it is a characteristic feature of spray pyrolysis that the as-deposited films are typically amorphous or biphasic amorphous-crystalline, which can be transformed to their crystalline phase by thermal annealing.[187–189] In spray pyrolysis, metal salt is dissolved in an organic solvent, and this precursor is sprayed on a heated substrate. Upon impact on the heated substrate, the organic solvent evaporates and the metal salt simultaneously crystallizes, forming a ceramic oxide thin film. An interesting feature of wet-chemical synthesis techniques is their use of organic precursors, which have been shown to control the amorphous-to-crystalline structure through their chain length, and to incorporate into the film structure and act as space fillers during the metal-salt-to-oxide pyrolysis reaction.[147] In addition, the choice of organic precursor is critical in controlling the thin film deposition because the temperatures of solvent evaporation and metal salt crystallization need to be tuned such that both reactions occur simultaneously. Consequently, the choice of solvent greatly affected the film's short-range order and crystallization kinetics. In summary, amorphous films deposited *via* wet-chemical techniques have fundamental structural deviations from classic crystalline ceria synthesized at high temperatures of up to two thirds of the melting temperature, *via* particle densification.

Despite previous work on the crystallinity and grain growth of ceria thin films deposited by spray pyrolysis,[147,183,187] systematic studies on the critical film thickness, and crystal texture evolution as a function of deposition and annealing temperature are still missing to date. In order to fully harness the potential of spray pyrolysis, it is necessary to understand how the different processing parameters affect the material structure, and subsequently, relevant properties such as ionic conductivity. Clear guidelines are needed on how processing parameters affect the mechanical stability, as well as critical thresholds that lead to processing failures such as cracking. In particular, the rational engineering of ceria catalyst materials

requires good control over the crystal orientation, and it is desired to achieve cheap and scalable pathways to assemble high catalytic activity ceria with <100> orientation, and to characterize the structure of such materials quickly and easily. With singular reports that thermal annealing can induce a preferred <100> orientation – which was assumed thermodynamically unfavorable in ceria – we see promise in systematically studying thermal processing parameters of sprayed ceria to induce texture evolution in a controlled fashion. This would provide a new, simple, and cheap tool for the rational design of catalytic materials.

In this work, we systematically study the impact of deposition parameters and thermal treatment on the mechanical and lattice vibrational properties of cerium oxide. For this, we select ceria thin films deposited *via* spray pyrolysis, a wet-chemical precipitation-based deposition technique, and subject thin films to various thermal annealing to vary crystallinity and study thin film orientation. We determine critical film thicknesses to provide guidelines for practical thin film deposition. Moreover, we complement crystal structure analyses through X-ray diffraction with Raman spectroscopy to study how vibrational properties correlate with the crystal orientation and texture of thin films. Through this, we collectively combine the low-cost fabrication method of spray pyrolysis with accessible Raman spectroscopy, and demonstrate how these methods can be used to fabricate and characterize ceria thin films with controlled crystal orientation for catalytic and electrochemical applications.

5.2 Experimental Methods

Sample Preparation: To deposit cerium oxide thin films, a precursor solution, composed of 0.01 mol/l cerium nitrate (III) hexahydrate (99.9% purity, VWR international, USA) dissolved in 33:33:33 volume percent bis-2 ethyl hexyl phthalate, 1- methoxy 2-propanol, and ethanol (all reagent grade chemicals with >98% purity from Sigma Aldrich, USA), was fed into a spray gun (AG361, DeVILBISS, USA) at a flow rate of 6 mL/hr. The precursor was atomized into droplets at an air pressure of 1 bar and sprayed for 2 hours onto a heated substrate that was at a distance of 20 cm from the spray gun. Parameters listed above were determined to be optimal for film homogeneity and quality after several tested depositions, see SI. Substrates used are as follows: Si_3N_4 coated (100) silicon wafers (100 mm diameter, Cemat Silicon, Poland) for critical thickness measurements, Si_3N_4 coated (100) silicon substrate (1cm x 1 cm, Sil'tronix, France) for XRD measurements, and MgO substrates (1cm x 1cm, (001) oriented, single side polished, MTI Corp, USA) for Raman measurements. Since silicon shows a strong Raman mode that dominates the Raman signal of ceria thin films, Raman measurements were performed on thin films simultaneously deposited on MgO substrates at identical conditions to films deposited on silicon/silicon nitride for XRD measurements. For each deposition, substrates were placed on a steel plate which was heated by a hotplate (VWR, USA). A slot was milled from the edge to the center at the bottom of the steel plate where a thermocouple was placed to record the temperature before and throughout the deposition. Prior to the deposition, the hotplate set temperature was adjusted such that once stabilized, the thermocouple temperature read the temperature listed in the text (*e.g.,* samples listed 'as-deposited 400 °C' were deposited with the thermocouple in the steel plate reading 400 °C). Reproducing the read thermocouple temperature of the steel plate, rather than the set temperature of the hotplate yields more accurate and reproducible results, and most closely approximates the true surface temperature at deposition. During spraying, the recorded temperature decreased significantly, due to cooling by the air and precursor from the spraying. It is important to note that the temperature being recorded is of the center the of steel plate and not measured at the substrate surface. This causes slight deviations between the measured temperature and true surface temperature due to the different thermal properties and exposure to fluids between the substrate and the steel plate. However, due to convective cooling effects, accurate measurement of the substrate surface temperature was impossible, and it was determined that the thermocouple placed under the substrate most closely reflects the substrate temperature during deposition. Both MgO and Si substrates were deposited concurrently, such that comparisons between XRD and Raman measurements at each deposition temperature were of samples deposited simultaneously. Deposited films were broken into halves, for Si substrate samples, or quarters, for MgO substrate samples, and individual pieces were annealed at their specified temperature (500 °C, 650

°C, or 800 °C) for 6 hours at a 10 °C/min heating rate under stagnant air in a box furnace (Nabertherm, Germany).

Characterization: Grazing incidence X-ray diffraction (XRD) was performed on thin films with a SmartLab diffractometer (Rigaku, Japan) using Cu K_α radiation at a 40mA current and 40 kV voltage. XRD data was fit using the HighScorePlus software (Malvern Panalytical, United Kingdom) and full width half maximum values from fitted peaks were used to calculate grain size by the Scherrer equation. Raman spectroscopy measurements were performed using an alpha300R confocal Raman microscope (WITec, Germany), with a 532 nm Nd:YAG laser and an analysis grating of 600 g/mm. Samples were measured through a 50x objective, with 10 accumulations of 5 s each, and at three different positions per sample. Surface profilometry (Dektak 150, Veeco, USA) was used to determine the thickness of films deposited on the silicon wafer at 1 cm spaced out points from the center of the wafer.

5.3 Results and Interpretation

5.3.1 Film Critical Thickness

A basic requirement for successful thin film deposition *via* any wet chemical ceramic processing method like spray pyrolysis is achieving dense and crack-free films. Often this is challenged by controlling parameters of pyrolysis reactions, drying of the organic constituents and densification all occurring in parallel in formation of the film on a substrate. To achieve a high process control level, the critical thickness above which cracks begin to form is a useful deposition parameter to define the feasible range of thin film thickness under a certain set of spraying conditions.

To determine the critical thickness of sprayed ceria thin films, we deposited films on Si_3N_4 coated (100) silicon wafers, arranged such that the center of a wafer was aligned with the spray gun nozzle. **Figure 5.1 a** schematically shows the spraying plume in which the atomized precursor is deposited from the spray gun onto the substrate in a conical distribution. In this flow pattern, precursor flow was highest at the center of the spray cone and radially reduced outward. This resulted in a radial thickness gradient along the wafer schematically depicted in **Figure 5.1 a** where higher volumes of the precursor are deposited closer to the center of the wafer. This inherent thickness gradient created a controlled means of determining the critical thickness during a single deposition. The film thickness distribution was then measured *via* surface profilometry at evenly spaced-out points from the center of each wafer outwards.

Figure 5.1 b displays the film thickness measured via profilometry as a function of distance from wafer center for films deposited at 350 °C, 400 °C, 450° C, and 500 °C. In spray pyrolysis, the temperature needs to be high enough such that the organic precursor undergoes pyrolytic decomposition during deposition, *i.e.,* the simultaneous evaporation of the organic solvent and the crystallization of the metal salt upon impact on the heated substrate. As such, we selected temperatures near and above the boiling point of the highest boiling point precursor used, bis-2-ethyl hexyl phthalate. Controlling the deposition temperature during the spray pyrolysis process allows for control over the rates of the two concurrent reactions, evaporation and crystallization, which in turn controls the deposition rate, microstructure, density, and potentially formation of organic residues in the film. At the center, films are the thickest, with a maximum thickness of approximately 2.5 μm, and radially decreasing thickness from the center. Optical micrographs were taken at each profilometry measurement point to determine the relationship between film thickness and film morphology. From optical micrographs of the film deposited at 500 °C in **Figure 5.1 a** (refer to the appendix for the remaining three deposition temperatures), one can see at the center of the spray cone and at a distance of 1 cm from it, that the films exhibit a substantial amount of cracking on the range of tens of microns in

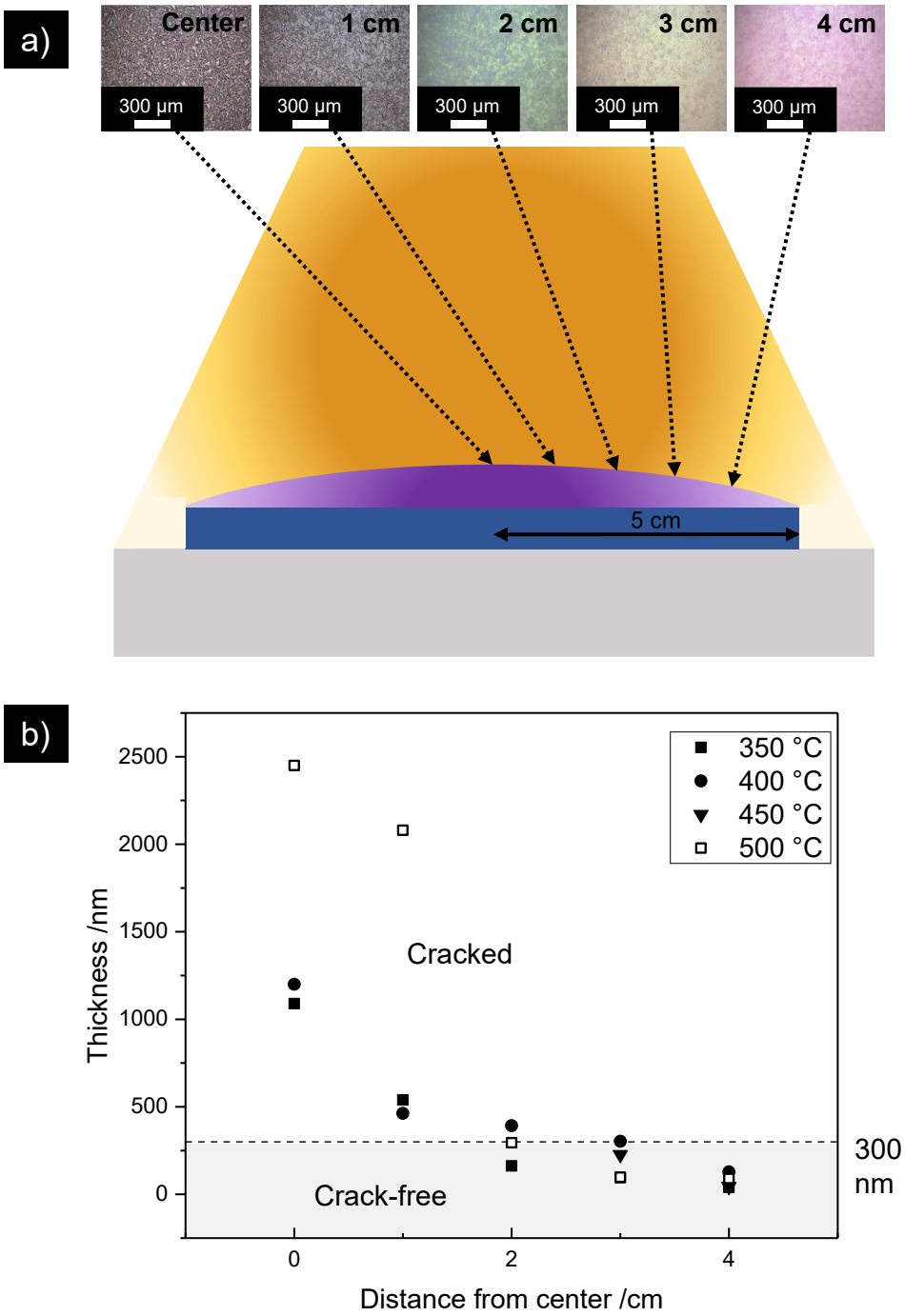

Figure 5.1 a) Schematic of the thickness gradient stemming from volume of precursor deposited during spray pyrolysis with optical micrographs of a sprayed wafer deposited at 500 °C from the center to 4 cm away. **b)** Film thickness as a function of distance from the center of a sprayed silicon wafer, with a critical thickness of 300 nm for all deposition temperatures.

crack length and also some loose powder at the surface. On the other hand, at a position of the substrate about 2-3 cm away from the center, films are dense, smooth, and crack-free. Moreover, the films show typical signs of pyrolysis dense films with rims of dried micron-sized droplets originating from the droplet-by-droplet deposition nature of spray pyrolysis. By correlating optical micrographs and measured thicknesses of films at each point and deposition temperature, we confirm successful film deposition at all deposition temperatures and observe cracking when the thickness exceeded approximately 300 nm with a maximum thickness measured of 2.5 μm, **Figure 5.1 b**. An interesting observation is that this critical thickness defining dense and crack-free film deposition is independent of deposition temperature.

The upper limit of thin film thickness during deposition, and crack formation above this critical thickness, is driven by two main factors. First, the formation of cracks is initiated when it is energetically favorable to release strain energy caused by lattice mismatch and the thin film/substrate interface. Second, during wet-chemical deposition, evaporation of solvents causes additional loss of volume which can lead to film cracking. On the first, one can turn to Griffith fracture mechanics.[190] This widely used model is applicable to brittle glasses and ceramics; for example, it has been used to understand the critical thickness of amorphous silicon thin films for Li-ion battery electrodes.[191] When cracks form, there is an increase in surface energy that stems from the formation of two new surfaces at the crack and a decrease in strain energy due to the release of internal stress. According to the Griffith criterion, cracking occurs when the release of strain energy is greater than or equal to the increase in surface energy due to cracking. Thin films exhibit a high amount of strain, ascribed to interactions and lattice mismatch between the film and substrate, as well as precursor residues in the case of sprayed thin films. In the present study of sprayed ceria thin films, we can apply analogous reasoning to the Griffith criterion: as film thickness increases, the strain energy in the film increases, reaching a point at the critical thickness where the cracks can form to alleviate the buildup in strain energy (see SI). Because the film strain energy is dependent on thickness, there exists a critical thickness in which there is enough strain energy for cracking to occur. When films are thicker than the critical thickness, cracks form. We find that this point is reached at a thin film thickness of 300 nm for sprayed ceria thin films.

5.3.2 Structural and Phase Evolution of Spray Pyrolysis Manufactured Films

To investigate the impact of thermal treatment on the microstructural evolution of spray pyrolysis ceria films, we turn to x-ray diffraction data, collected on ceria thin films deposited on Si/Si_3N_4 substrates. Based

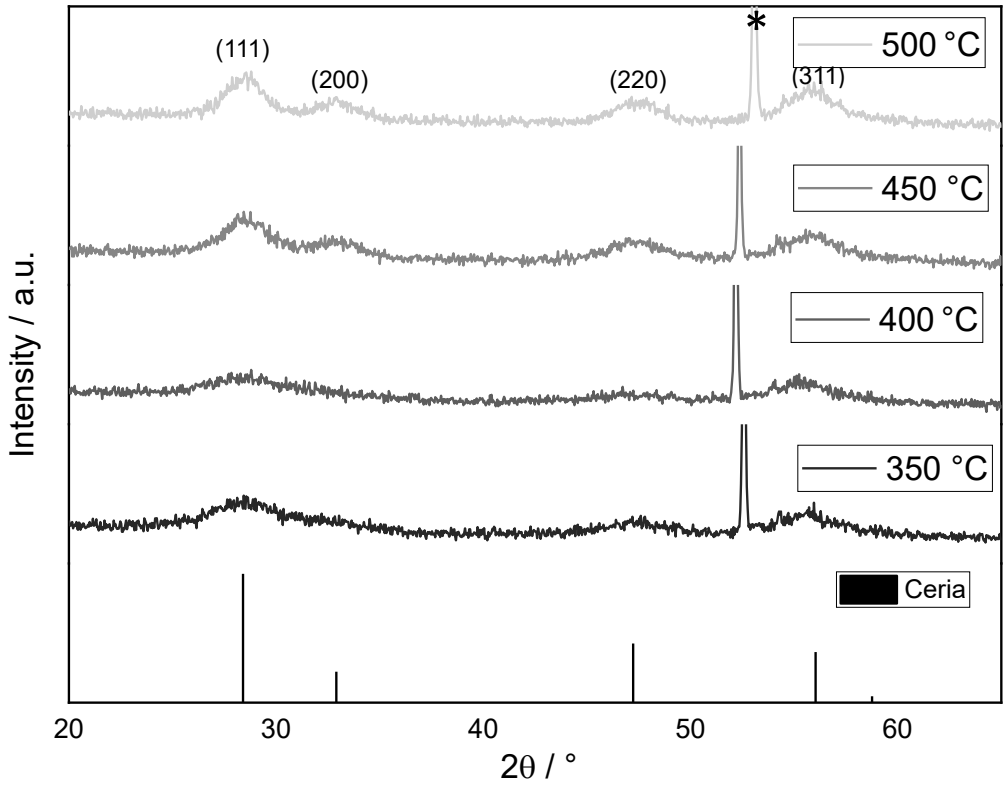

Figure 5.2 XRD of as-deposited sprayed films deposited at 350 °C, 400 °C, 450 °C, and 500 °C. Broad, weak ceria peaks are observed, corresponding to largely amorphous ceria with dispersed nano-crystallites.

on our critical thickness results, films for the remainder of this work were deposited at a distance of approximately 3 cm from the center of the spray cone to ensure dense, crack-free films. Four different deposition temperatures were explored, namely 350 °C, 400 °C, 450 °C, and 500 °C. This range of temperatures was accompanied with different thin film thicknesses due to the different rates of solvent evaporation at teach temperature, ranging from 30 nm for deposition at 450 °C to 250 nm for deposition at 350 °C. While this thickness variation affects the signal-to-noise of the structural analyses performed here, we do not expect that thickness itself influences the evolution of crystallinity, average grain size, or texture explored here. For all thin films, XRD patterns, **Figures 5.2 and 5.3**, exhibit the (111), (200), (220), and (311) peaks corresponding to the ceria cubic fluorite structure, and in addition, a sharp peak is present at 2θ = 52°, attributed to the single crystal silicon substrate. We first investigate the as-deposited films. **Figure 5.2** depicts the XRD data of the as-deposited films deposited at 350 °C, 400 °C, 450 °C, and 500 °C. XRD peaks of as-deposited films are broad with low intensity, showing a slight increase in intensity and decrease in full-width half-maximum (FWHM) at higher deposition temperatures. Broad peaks with

low intensity are characteristic for ceria deposited *via* spray pyrolysis and indicate that a significant fraction of the film is amorphous.[146] The increasing intensity and sharpness of peaks for increasing deposition temperature is caused by thermally promoted nucleation and grain growth.

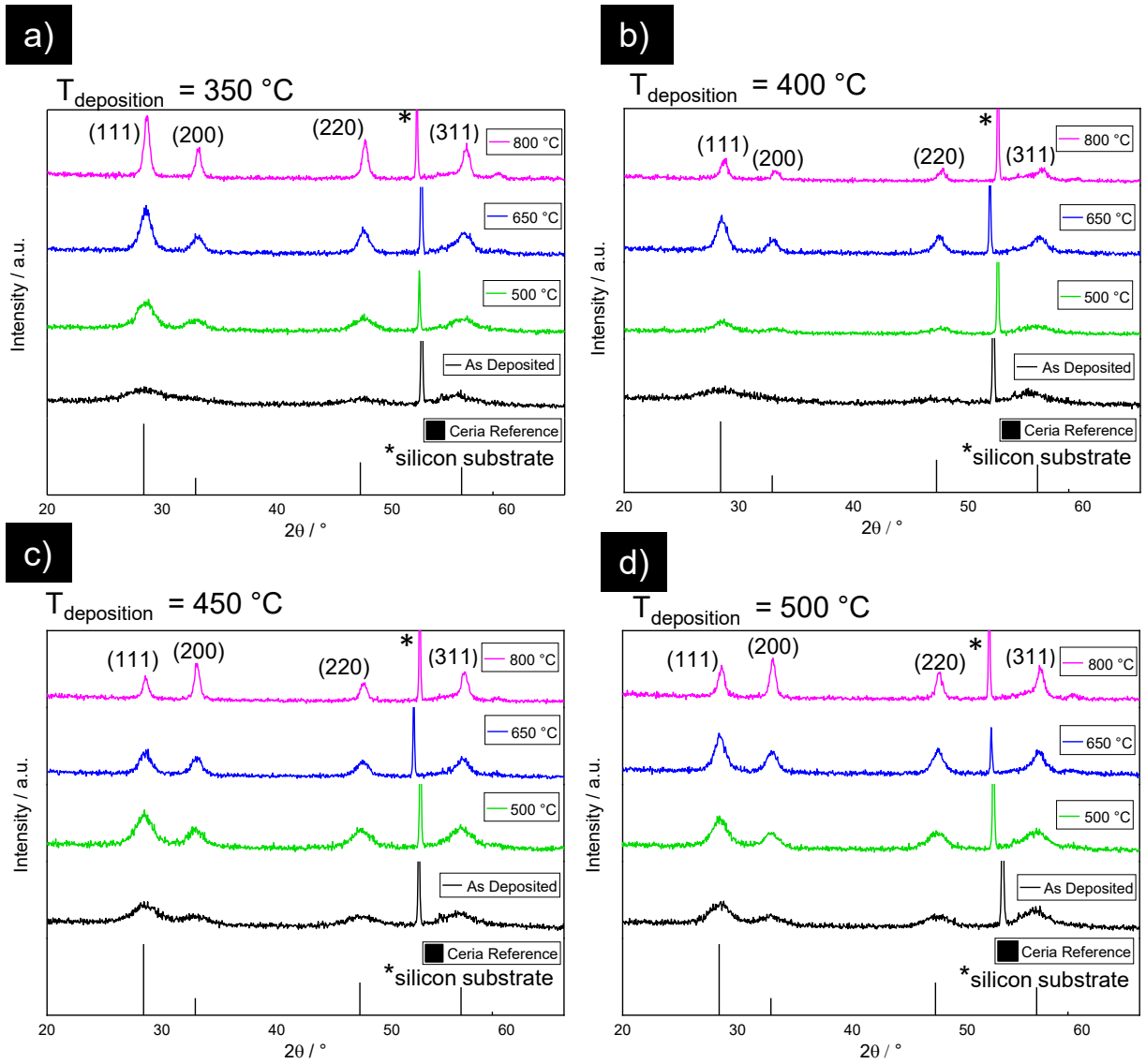

Figure 5.3 XRD of as-deposited and annealed films deposited at **a)** 350 °C **b)** 400 °C **c)** 450 °C **d)** and 500 °C. For all films, annealing causes XRD peaks to become sharper and more intense. For thin films deposited at 450 °C and 500 °C, annealing induces significant texture in favor of <100> orientations.

We detail the effect of post-annealing temperature between 500 °C and 800 °C on the synthesized film microstructure with the corresponding XRD patterns in **Figures 5.3 a-d**. No cracking was observed for any of those thin films. In general, we see the following qualitative trends: Firstly, increasing the deposition temperature results in slight increases in peak intensity and decrease in FWHM, and secondly, increasing

post-anneal temperature causes peak FWHM to drastically decrease by approximately 60-67 % and intensity to further increase. To analyze this in more detail, we plot in **Figure 5.4** average grain sizes calculated using the Scherrer equation, based on the FWHM value of the (111) peak, as a function of post-annealing and deposition temperature. Average grain sizes of different samples here range from 2 nm to 14 nm and increase with annealing temperature from 500 °C to 800 ° C. Closer inspection reveals that we have a higher impact of post-annealing temperature than effective deposition temperature for the films. The high errors in grain size for as-deposited films are due to the nature of the low intensity, broad XRD peaks characteristic of amorphous films. At the highest annealing temperature of 800 °C, we also observe large error bars in the grain size, corresponding to fluctuations in the FWHM and intensity of different XRD peaks. We attribute this to the presence of texture which affects relative intensity, a feature that will be discussed in more detail below.

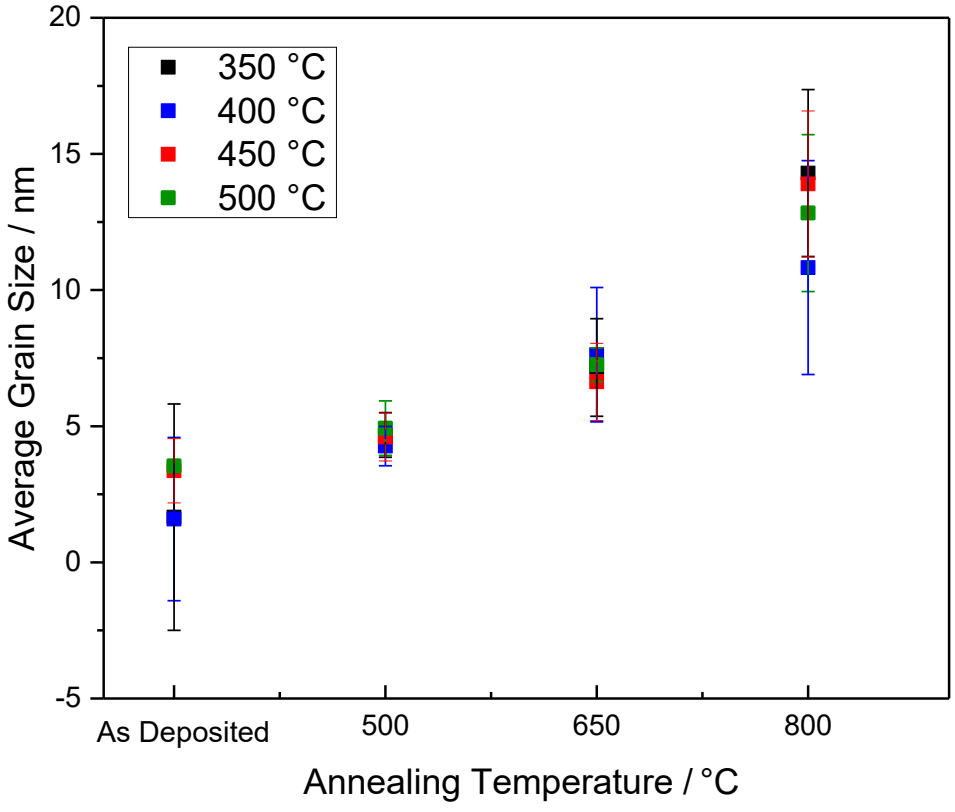

Figure 5.4 Average grain size as a function of annealing temperature calculated using the Scherrer equation for the (111) peak. Post-annealing induces crystallization and grain growth of the largely amorphous as-deposited ceria thin films.

Furthermore, the sharpening and intensification of XRD peaks with annealing temperature can also be ascribed to an increase in crystallinity. It has been demonstrated that as-deposited spray pyrolysis films tend to be primarily amorphous with small, dispersed seed crystals and fully crystallize upon annealing.[150,183,187,188] Extrapolating data from a Johnson-Mehl-Avrami-Kolmogorov (JMAK) analysis of spray-pyrolysis-deposited ceria films from a previous investigation[187] reveals that annealing at 500 °C for 5 hours results in a fully crystalline film if seed crystals are present as-deposited. The presence of broad, weak diffraction peaks in the as-deposited films confirms that some crystallites are present, yet the overall low signal of these peaks implies a largely amorphous structure.

In addition, the XRD data reveals interesting trends in the texture, or preferred orientation, induced by the thermal treatment of sprayed ceria thin films. For the majority of films, the (111) diffraction peak shows the highest intensity, in agreement with the randomly oriented ceria powder reference. The preference for the (111) orientation is expected due to the high stability of the (111) plane.[179],[192] ,[193] However, for samples deposited at substrate temperatures of 450 °C and 500 °C, a gradual shift of the preferred orientation from the (111) to the (200) orientation is observed with annealing. Remarkably, after annealing at 800 °C, the (200) peak has the highest intensity, meaning that annealing induced texture with a preference for (200) orientation in the plane parallel to the substrate. To better quantify this phenomenon, the texture coefficients of the (200) peak, presented in **Table 1**, were calculated using Eqn 2:

Texture Coefficient:
$$C_{200} = \frac{I_{200}}{I0_{200}} \left(\frac{1}{n} \sum \frac{I_{hkl}}{I0_{hkl}} \right)^{-1} \quad \text{Eqn. 2}$$

where I_{200} and I_{hkl} are the intensities of the (200) peak and a general peak with Miller indices (hkl), respectively. Further, $I0_{200}$ and $I0_{hkl}$ correspond to the intensities of a standard ceria powder diffraction reference (ICDD:00-067-0121),[194] and n is the number of reflections utilized in the summation within Eqn 2. Here, the (111), (200), (220), and (311) diffraction peaks were used in the calculation with $n = 4$. The (200) texture coefficient measures if there is a textural preference associated with {100} planes in the thin film. If the texture coefficient is 1, this implies that the texture matches that of the reference and that the <100> direction is not more or less prevalent than in a reference powder. In this reference case, the {111} set of planes is the most preferred for ceria. In contrast, a (200) texture coefficient greater than 1 corresponds to a preferred <100> orientation, and the higher the texture coefficient, the more pronounced the texture. A texture coefficient of less than 1 means that the <100> orientation is less preferred than in a randomly oriented sample.

$T_{deposition}$ /°C	$T_{Annealing}$ /°C	Texture Coefficient (200)	Lattice Constant / nm
350	As Deposited	-	-
	500	1.247	0.541 ± 0.009
	650	1.295	0.541 ± 0.010
	800	1.481	0.539 ± 0.009
400	As Deposited	-	-
	500	1.003	0.541 ± 0.032
	650	1.338	0.542 ± 0.008
	800	1.451	0.538 ± 0.030
450	As Deposited	-	-
	500	1.489	0.543 ± 0.006
	650	1.771	0.541 ± 0.007
	800	2.198	0.540 ± 0.006
500	As Deposited	-	-
	500	1.487	0.543 ± 0.010
	650	1.559	0.542 ± 0.005
	800	2.016	0.540 ± 0.007

Table 5.1 (200)-Texture coefficient and lattice constant (calculated from the (111) peak) of films at the four annealing and deposition temperatures. Texture in the <100> direction increases with annealing, and no trend is observed in the lattice constant with annealing

Because as-deposited films are mostly amorphous with only a minimal number of small crystallites, the concept of texture coefficient is not applicable, and we exclude these films from the texture coefficient analysis. Turning to the texture coefficients for films post annealed at 500 °C, we observe that films deposited at 350 °C and 400 °C have values close to 1, revealing a preference for the <111> direction as expected from the polycrystalline ceria reference data. However, films deposited at 450 °C and 500 °C also

post annealed at 500 °C have texture coefficients of approximately 1.5, indicating a significant preference to the [200] direction relative to the reference even at this low annealing temperature. As post-anneal temperature increases for all deposition temperatures, the texture coefficient increases, reaching a value of approximately 1.5 for films deposited at 350 °C and 400 °C and 2 for films deposited at 450 °C and 500 °C. Texture coefficients of 2 indicate that we obtain films with a remarkably high texture in the [200] direction at high deposition and annealing temperatures. The majority of films here have texture coefficients greater than 1, which suggests that there is an overall stronger presence of (200) oriented grains, compared to the polycrystalline ceria reference, that increases with temperature.

Such a thermally prompted shift in preferred orientation has previously been observed on ceria thin films deposited *via* spray pyrolysis[182],[183] pulsed laser deposition[184], and electron-beam-evaporation[186]. However, the reason for this prevalence of the (200) peak with increasing processing temperatures has been a point of speculation, as the (200) surface has been shown to be unstable due to its relatively high surface energy and net dipole moment arising from its arrangement of alternately charged planes.[192] Several density functional studies have confirmed that the ordering of surface energies of the low index ceria planes from highest energy to lowest energy is: {100}>{110}>{111}.[179],[180] Consequently, the transition from (111) to (200) oriented films is expected to be energetically unfavorable and unstable; one would expect that upon annealing, films would relax to the most energetically favorable configuration. Therefore, the energetics calculated in these studies must be incomplete. Recent studies have identified the emergence of {100} terminated facets in ceria nanoparticles[178], [185] and <100> preferred orientations in thin films[184],[195] upon thermal treatment. It has been suggested that surface defects[185], such as oxygen ion vacancies[178], impurities, or surface reconstructions[196] may facilitate the stabilization of {100} surfaces. In a computational study on {100} terminated ceria surfaces, it was determined using density functional theory that various reconstructions of the {100} surface could become energetically favorable at lower oxygen partial pressures by the formation of oxygen defects.[178] Annealing films that were deposited at higher temperatures may provide the required energy needed to reconstruct or form oxygen vacancies at the surface. However, in the present study, annealing was conducted under stagnant air and not under reducing conditions as described in ref. [178]. Therefore, the analysis only provides a partial explanation for how (200) oriented films could be stabilized and energetically favorable.

Understanding how to tune ceria processing such that the {100} facets are prevalent is appealing for catalyst applications and a point of active research. {100} surfaces have been demonstrated experimentally and computationally to have higher catalytic performance and activity[181],[197] than {111} surfaces as a result of the higher surface energy of {100} surfaces, which leads to more favorable oxygen vacancy formation energetics, and in turn a higher affinity to participate in oxygen-exchanging reactions. Therefore, the simple

method of controlling film texture with a preferred [100] orientation presented here shows promise in controlling and engineering catalytic surface activity of ceria.

To complete the XRD analysis, we turn to the lattice parameter, which can be useful in detecting lattice strain. **Table 1** shows the lattice parameter at each deposition and annealing temperature. Lattice parameters range from 0.539 nm to 0.542 nm which is close to the fully relaxed value 0.541 nm for ceria.[198] Slight fluctuations in lattice parameters are seen, yet there is no clear trend with annealing or deposition temperatures. While this implies the presence of some degree of lattice strain, the lack of trend with temperature shows that it is likely not thermally induced.

5.3.3 Raman Analysis

To complement the XRD film microstructure analysis, we turn to Raman spectroscopy, which can provide deeper insight into the short-range order, bonding, and strain within a solid. Due to its cubic symmetry, the only Raman active mode for pure, stoichiometric ceria is the triply degenerate F_{2g} stretching mode. This mode corresponds to the so-called oxygen breathing mode, *i.e.,* the bond vibrations between the cerium ion and eight tetrahedrally coordinated oxygen ions in the cubic fluorite structure, which appears at a 465 cm^{-1} wavenumber for bulk ceria.[168] **Figure 5.5** displays Raman spectra of films deposited at 350 °C and post-annealed at 500 °C, 650 °C, and 800 °C on MgO substrates. In each spectrum, the F_{2g} mode is present, and for the as-deposited film, several additional peaks are observed at wavenumbers ranging between 600 cm^{-1} and 1500 cm^{-1}. The Raman spectrum of bis 2-ethyl hexyl phthalate, the highest-boiling point organic component of the spray pyrolysis precursors, is displayed for reference of comparison to the as-deposited film. Overlapping peaks between the two spectra can be observed, suggesting that the additional peaks in the as-deposited film can be attributed to organic residues from the precursor. Interestingly, we only detect organic residues in the Raman spectrum for the film as deposited at 350 °C, which implies that at higher annealing and deposition temperatures organic residues further decompose and evaporate from the film, becoming undetectable for Raman spectroscopy. The presence of these organic Raman peaks confirms that the organic precursor becomes incorporated into the amorphous-crystalline film structure for films as-deposited at 350 °C. To the best of our knowledge, Raman has not been used before to clearly detect organic precursor residues in spray pyrolysis films. Controlling the amount of organic precursor residue is useful in situations where impurities could impact film functionality. For instance, ceria can be employed as a low temperature proton conductor, so having organic residues within the film could be beneficial in potentially increasing the protonic defect density and thereby proton conductivity.

Figure 5.6 displays Raman spectra around the F_{2g} mode for each deposition and annealing temperature, for further analysis of this characteristic Raman peak. For all spectra, except for the as-deposited film at 400 °C,

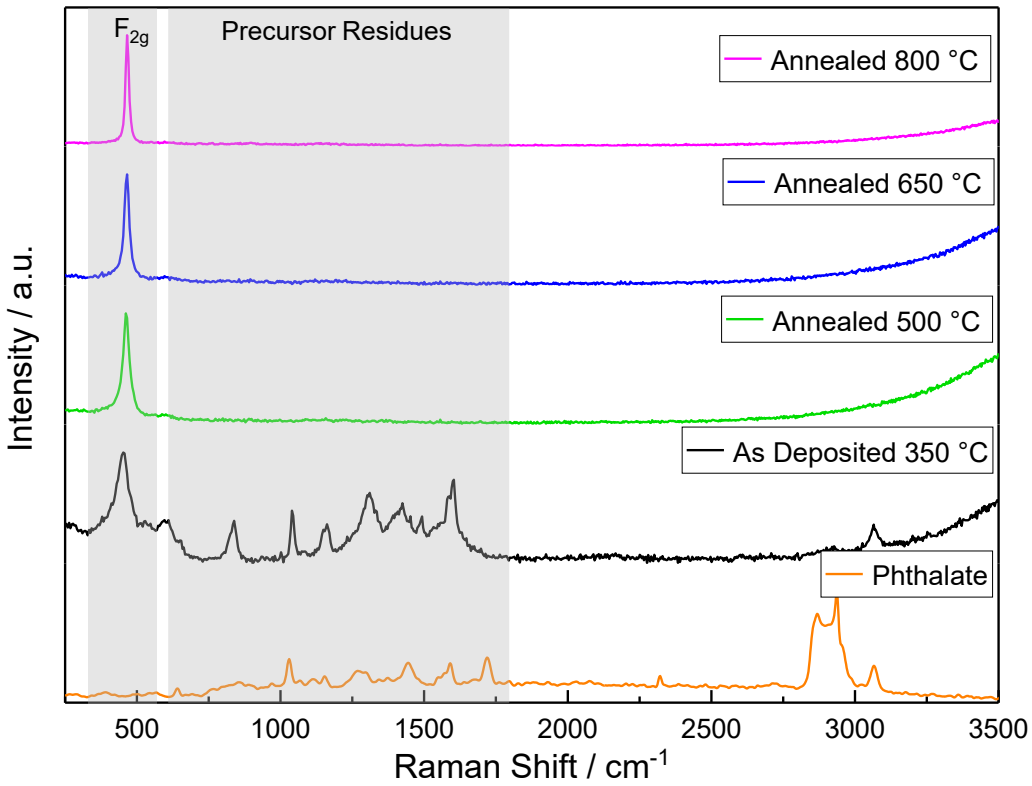

Figure 5.5 Raman spectra of a sprayed film as-deposited at 350 °C and annealed at 500 °C, 650 °C, and 800 °C. All films show sharp F_{2g} Raman peaks, and the film as deposited shows a signature of the organic precursor, indicating that organic precursor was incorporated into the film during deposition.

the F_{2g} peak is present. The overall peak intensity was weak due to the low thickness of the films, and for the film as-deposited at 400 °C, no F_{2g} peak was observed, likely due to the weak signal of this thin film. Due to film thickness variations and instrument limitations on focusing quality during measurements, relative peak intensities fluctuated greatly, so we cannot draw any conclusions from peak intensity. As-deposited peaks are relatively broad, due to their amorphous microstructure. The lack of periodicity in an amorphous solid results in lattice vibrations that are more disordered and differ from the phonons of a crystalline solid. This impacts Raman scattering, causing broader Raman peaks with an asymmetric line shape.[199] As annealing temperature increases, peaks narrow, indicating a transition from amorphous to crystalline microstructures[200] and grain growth,[201] agreeing with XRD results. Furthermore, changes in the F_{2g} Raman mode position with annealing are observed. This is shown in **Figure 5.7** where the F_{2g} mode position is plotted against annealing temperature and listed in **Table 2**. We classify two regions of F_{2g} peak positions: Region I (shaded in gray) and Region II, being below 465 cm^{-1} and above 465 cm^{-1}, respectively.

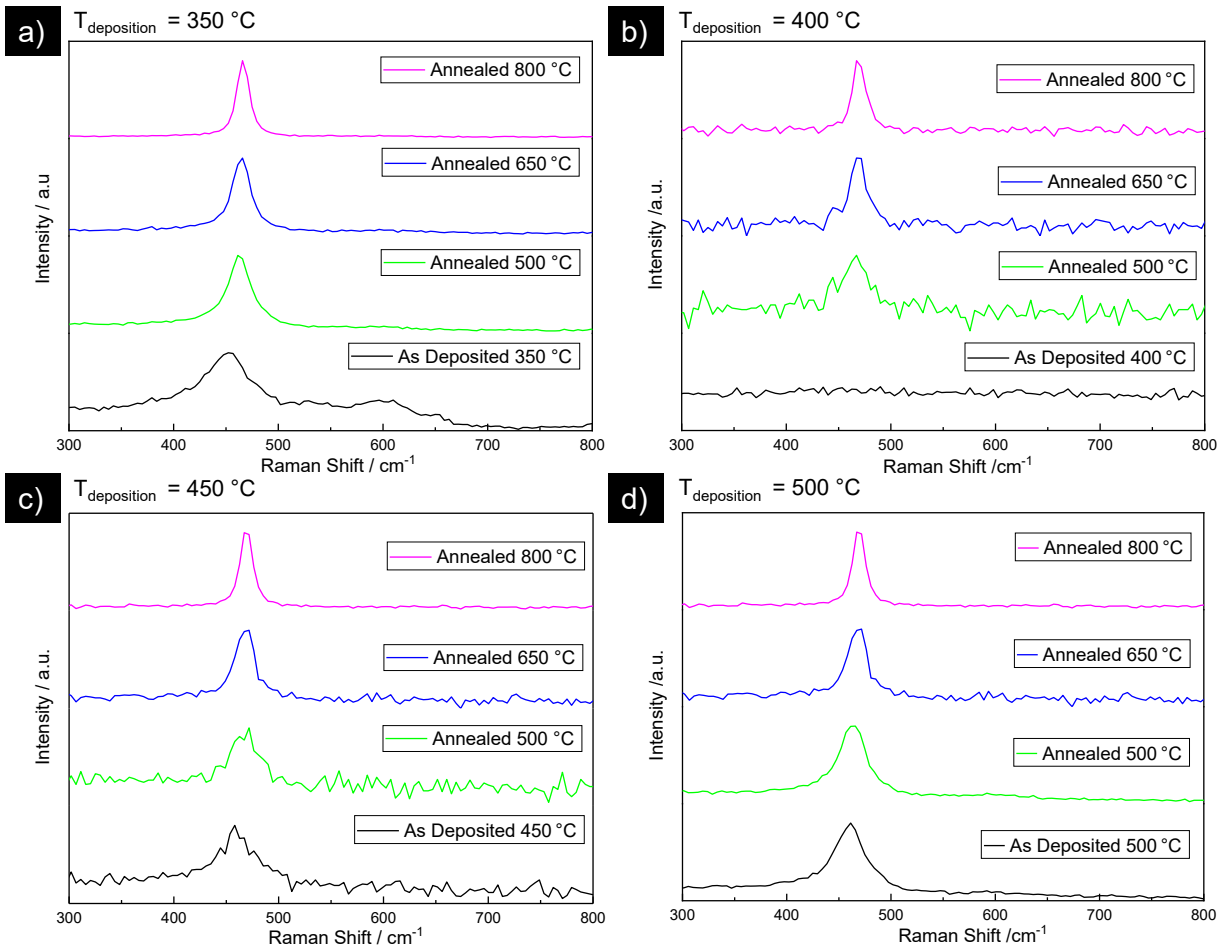

Figure 5.6 Raman spectra of the F_{2g} peak of as-deposited and annealed films deposited at **a)** 350 °C, **b)** 400 °C, **c)** 450 °C, **d)** and 500 °C.

In Region I, F_{2g} mode positions of as-deposited films are significantly below the characteristic bulk value of 465 cm^{-1}, with a general trend of increasing F_{2g} wavenumber with increasing post-anneal temperature. As established by XRD results, as-deposited films at all deposition temperatures exhibit a significant fraction of amorphous microstructure. Because annealing increases both grain size and crystallinity, a combination of these features prompts the general increase Raman mode frequency with annealing up to the bulk standard of 465 cm^{-1}.

The observation that for all as-deposited samples where an F_{2g} peak was present, the F_{2g} peak position was significantly lower than the expected bulk value of 465 cm^{-1} is expected: The amorphous structure is generally more disordered and has longer average cerium-oxygen bonds than the crystalline phase, which results in a lowered F_{2g} mode frequency for the largely amorphous as-deposited films. Additionally, the film as-deposited at 350 °C stands out with a notably low F_{2g} wavenumber of 450 cm^{-1}. While this low wavenumber can in part be attributed to its largely amorphous microstructure with a small number of

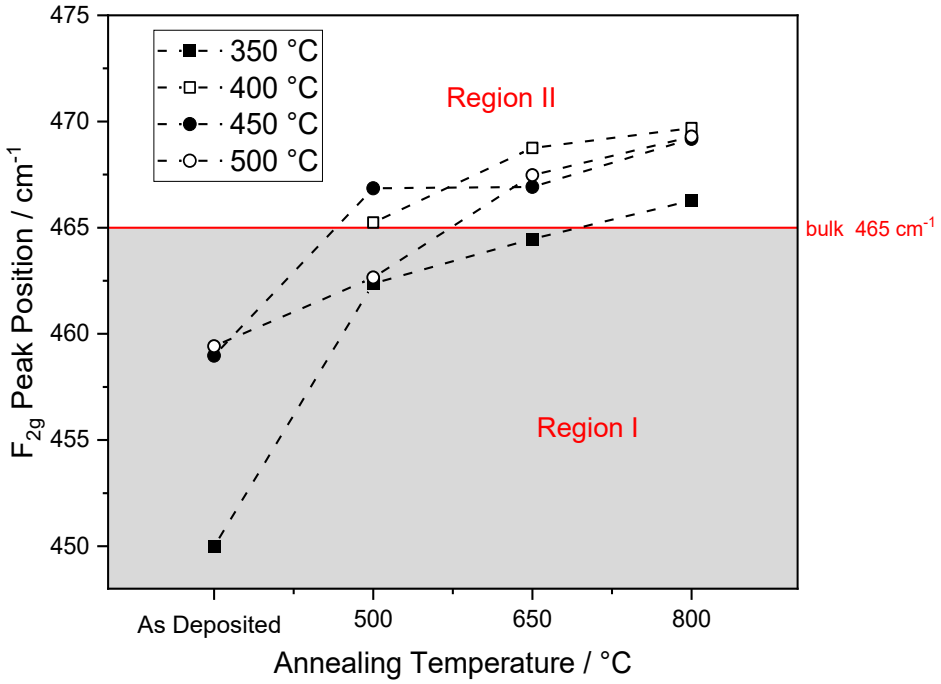

Figure 5.7 F_{2g} Raman peaks positions as a function of annealing temperature. Two regions are observed in the Raman F_{2g} peak position. Region I: For as-deposited films and some films annealed at 500 °C, the F_{2g} peak is below the bulk ceria value of 465 cm^{-1}. Region II: High temperature annealed films show a F_{2g} peak position above 465 cm^{-1}.

dispersed nano-crystallites, it is also important to note that the film as-deposited at 350 °C was the only to exhibit Raman-active organic precursor residues. The incorporation of organic precursor residues as space-filler in the structure of ceria films increases the cerium-oxygen bond distance, resulting in a lower F_{2g} mode frequency. As the residues evaporate during annealing, space in the film where residues resided is freed, allowing for closer packing of the cerium and oxygen ions and consequently an increase in F_{2g} mode frequency with annealing. Similar arguments have been made elsewhere that organic residues from the spray pyrolysis precursor can become incorporated into the film structure and result in a less compact structural packing.[147]

Four additional annealed films in Region I exhibit Raman peaks at or below the bulk peak position of 465 cm^{-1}. As shown from the XRD analysis in the previous section, particle size within thin films here is in the range of a few nanometers and increases with annealing temperature. It is well-known that for nanocrystalline ceria the F_{2g} peak is shifted to lower wave numbers compared to bulk ceria and that this shift increases with decreasing grain size.[147,201–203] This phenomenon is due to phonon confinement: when grain-size is on the nanoscale, phonons become constrained within the small grains, resulting in Raman

$T_{deposition}$ / °C	$T_{Annealing}$ / °C	F_{2g} Peak Position / cm^{-1}
350	As Deposited	450
	500	462
	650	464
	800	466
400	As Deposited	Peak not visible
	500	465
	650	469
	800	470
450	As Deposited	459
	500	467
	650	467
	800	469
500	As Deposited	459
	500	463
	650	467
	800	469

Table 5.2 Raman F_{2g} peak positions for different deposition and annealing temperatures.

peaks at lower frequencies with more asymmetric broadening compared to in the bulk state.[204–206] Therefore, given the particle size at the order of 5-10 nm for these films, phonon confinement can well explain the F_{2g} peak shift below the bulk ceria reference and the increase in wavenumber of this shift with increasing annealing temperature.

While there is general agreement in literature regarding the trends observed in Region I, the results from Region II are more surprising. In Region II, the F_{2g} mode similarly increases with annealing temperature. However, the F_{2g} peak exceeds the 465 cm^{-1} bulk value, reaching values around 470 cm^{-1} for films deposited

at 400 °C, 450 °C, and 500 °C and post-annealed at 800 °C. Such drastic changes in Raman shift and high F_{2g} mode frequencies are often indicative of lattice strain, which is particularly prominent in thin films. In literature, changes in F_{2g} mode frequencies on the scale shown here have been a result of chemical strain from doping[171], physically applied strain[207], and strain from the substrate[170] in thin films. However, films here are undoped, no external stress is applied, and the deposition of amorphous ceria with subsequent crystallization indicates that the substrate should not influence the strain either. Turning to the lattice parameters obtained from XRD measurements, **Table 1**, the macroscopic strain in all thin films is small and without a clear trend, which is inconsistent with the clear increase in F_{2g} frequency with annealing temperature. One would expect the lattice parameter to decrease with increasing Raman shift, as outlined by the Grüneisen parameter, which characterizes the correlation between lattice volume and vibrational frequency.[168] Raman shift is directly related to bond strength, which increases with decreasing bond length. Therefore, a noticeable decrease in lattice volume would be expected for such a drastic increase in F_{2g} frequency, which is however not observed in the long-range order as measured by XRD. In addition, we confirmed *via* XRD that there is no difference in the observed long-range order in thin films deposited on both the Si/Si_3N_4 substrates and the MgO substrates.

A recent study on epitaxially grown ceria has observed that apparent peak shifts toward higher Raman wavenumbers in ceria may be caused by breaks of crystal symmetry, and that the apparent Raman shift is actually a peak splitting of the triply degenerate F_{2g} mode.[208] However, this peak splitting should be detectable under polarized Raman spectroscopy, and we did not find any effect of polarization on the measured Raman peak position in this present study.

Interestingly, we observe a correlation between the F_{2g} peak position and the orientation of the grains, *viz.* the texture coefficient, as shown in **Figure 5.8**. Both parameters, the F_{2g} peak position and the texture coefficient, increase with increasing annealing temperature. We observe that for samples annealed at 500 °C, the F_{2g} peak position is close to the bulk value of 465 cm-1, and the (200) texture coefficient is close to 1. Therefore, samples annealed at 500 °C exhibit structural properties in agreement with the literature of equilibrated, stoichiometric cerium oxide.[118] In contrast, for samples annealed at 650 °C and 800 °C, we observe significant texture in favor of the <100> orientation, as well as high Raman F_{2g} wavenumbers between 465 cm^{-1} and 470 cm^{-1}. This suggests that the increase in texture for the <100> with annealing may cause a decrease in the cerium-oxygen bond length at the near order. This is a first indication that Raman spectroscopy could be used to measure thin film texture in ceria.

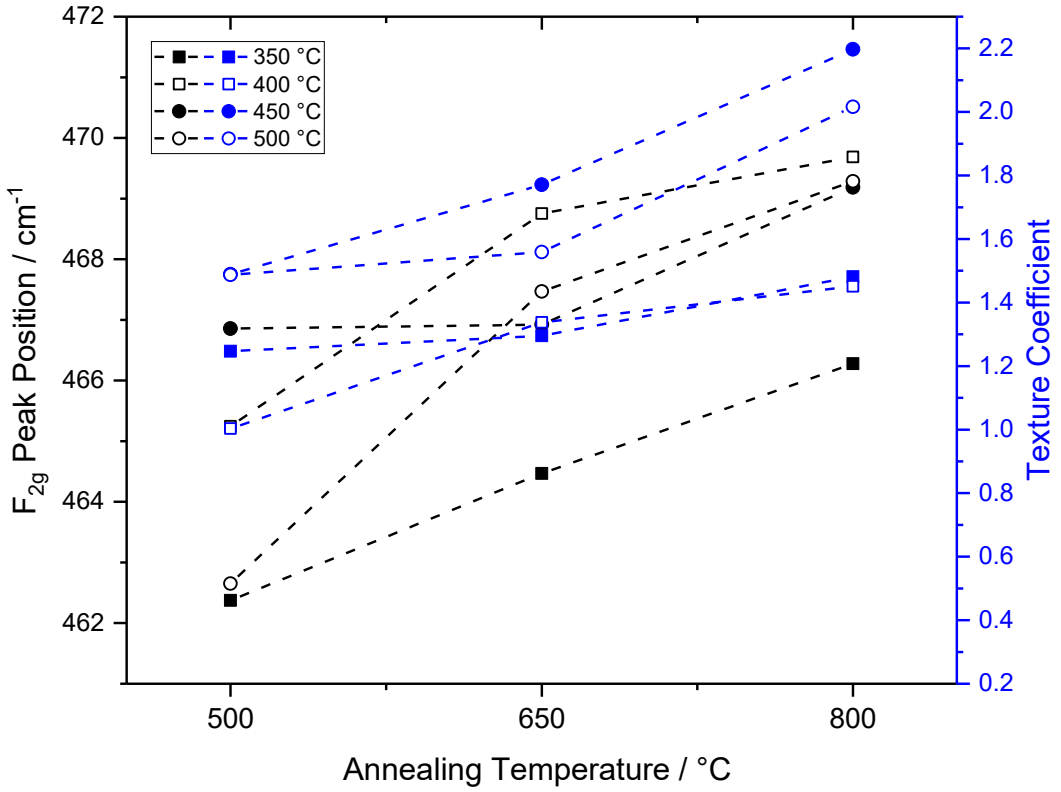

Figure 5.8 F_{2g} Raman peaks positions as a function of annealing temperature, for annealed thin films. The Raman F_{2g} peak position is correlated with the increasing (200) texture coefficient observed in annealed ceria thin films.

5.4 Conclusions

Spray pyrolysis is a promising method to deposit inexpensive ceramic thin film coatings with good control over microstructure and crystallinity. In particular, spray pyrolysis can be used to deposit ceria, which has particular importance as a catalyst material for solid oxide fuel cells, solar fuel conversion, and as an oxygen buffer in three-way catalysis. In this paper, we provide specific processing guidelines for the deposition of ceria thin films using spray pyrolysis, and study the effect of thermal processing on the orientation of sprayed ceria thin films, an important feature for catalytic applications. We consider what are the upper limits to deposit dense films under the complex interplay of solvent evaporation and ceria crystallization, and find that the critical thickness above which films cracked to be 300 nm. Understanding how to prevent crack formation is crucial when integrating spray pyrolysis deposited films into devices where crack formation hinders performance.

We newly report crystal texture data across a wide range of deposition and post-annealing temperatures, and find that a preferred orientation detected in XRD correlates to unusual peak shifts of the Raman F_{2g} oxygen breathing mode to higher wavenumbers. We find that the energetically unfavorable, but highly catalytically active [100] orientation becomes preferred after thermal annealing, and that Raman spectroscopy can be a useful, accessible tool to detect such orientation evolution for catalysis research.

Collectively this contributes to the fundamentals understanding of ceramic synthesis by spray pyrolysis, and specifically on the material class of ceria. In addition, it provides a cost-effective method to vary future catalyst coatings of ceria with orientations to control their functionality. For this we identify a new correlation between the F_{2g} Raman stretching mode and crystal orientation that can be used as a marker for future designs of thin film deposition pathways and catalytic coatings.

6. Chapter 6: Conclusions and Future Directions

6.1 Conclusions

In this thesis, a ceramic-electrolyte glucose fuel cell is demonstrated, with an unprecedented degree of miniaturization down to the nanoscale. It is shown that peak power densities of up to 43 $\mu W\ cm^{-2}$ can be achieved, showing that such ceramic glucose fuel cells based on a proton-conducting ceria electrolyte can reach power densities that meet the requirements of implantable devices. By selecting biocompatible materials that can be thermally sterilized, and through on-chip integration on silicon of the glucose fuel cell, these power sources can enable new implantable biomedical devices that require smaller and more reliable energy sources than currently available. The thesis optimizes the electrolyte microstructure both in terms of fabrication yield and device performance, through careful engineering of pulsed laser deposition parameters. Through this parameter optimization, in combination with a newly developed microfabrication route, a glucose fuel cell device fabrication yield of ~99% is achieved. Moreover, a dedicated characterization apparatus is developed, which enables the rapid characterization of glucose fuel cell device. This setup enabled the characterization of 150 glucose fuel cells in terms of their OCV, and of 12 glucose fuel cells in terms of their full power output performance. It is furthermore shown here that the ceramic electrolyte, ceria, exhibits proton conductivity sufficient for glucose fuel cell device operation, but extremely slow hydration kinetics at the order of days. Such slow hydration kinetics can explain the slow equilibration times observed during glucose fuel cell operation. Moreover, we see both through the operation of glucose fuel cells, and through model experiments on sprayed ceria thin films, that ceria exhibits significant proton conductivity within the interior of the material, and not just along adsorbed surface water. This confirms that proton conduction in ceria cannot be purely surface-governed, which has been a point of discussion in the literature so far.

Finally, new wet-chemical deposition methods for the ceramic ceria electrolyte are explored. The deposition parameter space of ceria spray pyrolysis is systematically explored, showing how thermal processing parameters during spray deposition and post annealing can control the degree of crystallinity, grain size, and film orientation. It is demonstrated that thermal annealing at 800 °C induces significant texture with a preference for the <100> direction. This has great significance for the application in glucose fuel cells and other catalytic applications, since ceria {100} surfaces are highly catalytically active due to increased oxygen vacancy density on such surfaces. Moreover, we find indications that this texture can be observed using Raman spectroscopy through the F_{2g} peak, creating an accessible and fast tool that could probe such texture at the near order.

6.2 Future Directions

6.2.1 Mechanistic Studies of Ceramic Glucose Fuel Cell Operation

This thesis explores some of the fundamental operation principles of a new electrochemical system, namely a ceramic-electrolyte glucose fuel cell. We demonstrate *in-vitro* that the novel ceramic-electrolyte glucose fuel cell shows promising power generation performance, that is sufficient to power implantable miniature bioelectronic devices. This constitutes a first, highly promising proof of concept, however, we observe relatively low open circuit voltage and relatively high fuel cell impedance compared to the expected proton conductivity of ceria. This indicates that under operation, the electrolyte is rate-limiting in the power output performance of the glucose fuel cell. It may be hypothesized that this is due to electronic leakage in ceria caused by electronic conductivity of ceria at low temperatures, and/or by pin holes or cracks created during the fabrication process, which would lead to metallic or chemical shorts in the fuel cell system. However, further mechanistic studies are required to explore the sources of losses and exact operation mechanism of the ceramic-electrolyte glucose fuel cell further. For example, experiments to determine the transference number of the ceria electrolyte would provide insights into the ratio of protonic to electronic transport within the electrolyte. This could be achieved through blocking-electrode experiments, which would prevent the transfer of protons or electrons and thus isolate the contribution of the freely passing species to total conductivity. Such studies will help understand what factors reduce the electrochemical performance parameters of the fuel cell, which is necessary to further engineer the glucose fuel cell and improve performance. In particular, future studies should consider different methods to distort the system from its equilibrium. As such, potential studies that could provide mechanistic insights include temperature-dependent measurements of the electrochemical impedance as well as power output performance, or to carry out electrochemical impedance spectroscopy and device performance measurements under bias.

Some preliminary studies were performed to explore the sources for losses in the fuel cell, and understand the relatively low OCVs observed in most ceramic-electrolyte glucose fuel cell devices. These are discussed in the **Appendix D** of this thesis. These first preliminary studies indicate that electronic leakage may contribute to overall low performance, but scatter in the data and variations of the model systems used complicate the interpretation. Thus, these preliminary studies were not able to fully answer questions about the relative contributions of electronic vs. protonic conduction in the fuel cell system, and particularly the electrolyte. More systematic studies examining the relative roles of oxygen stoichiometry, doping levels, microstructure, water loading, and thermal history will be helpful in unraveling these issues.

6.2.2 Future Ceramic-Electrolyte Glucose Fuel Cell Development for *in-vivo* Operation

This thesis demonstrates the first *in vitro* proof-of-concept of ceramic-electrolyte glucose fuel cells with the goal to harvest energy inside the human body to power implantable devices. To achieve *in vivo* operation of ceramic-electrolyte glucose fuel cells, several additional development steps need to be carried out. Here, we demonstrated a two-chamber glucose fuel cell operation mode, with an air breathing cathode. This development is important to give a proof of principle of the basic fuel cell chemistry and for material selection, and to demonstrate that such a glucose fuel cells can indeed work. In future work, one would consider next steps toward single-chamber operation, which is the required operation mode for an implanted glucose fuel cell because both glucose and oxygen are dissolved in the same fuel, *i.e.,* a body fluid. A potential pathway from two-chamber operation under an air-breathing cathode to a single fuel, single chamber operation is schematically outlined in **Figure 6.1**.

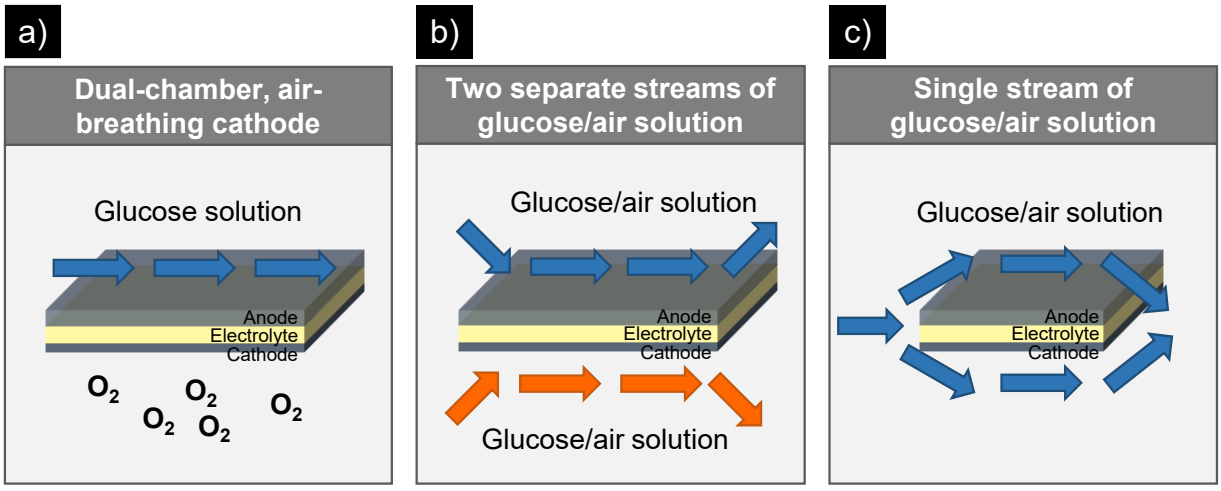

Figure 6.1 Development of the ceramic-electrolyte glucose fuel cell from **a)** a dual chamber, air-breathing cathode configuration, to **b)** the operation under two separate mixed, liquid fuel streams, and finally to **c)** a true single-chamber glucose fuel cell with a single fuel containing glucose and oxygen in solution.

The first step, **Figure 6.1 a**, was demonstrated in this thesis, where the anode was in contact with deaerated glucose solution, while the cathode was in contact with air. This configuration allows the verification of the basic electrochemical operation principle of the fuel cell system, as demonstrated here. The next, future step would be to put both electrodes in contact with separate streams of aerated glucose solution, **Figure 6.1 b**. By this separation, a chemical short circuit through the water flow is avoided, but at the same time, the catalyst selectivity can be determined due to the mixed nature of the fuel at both electrodes. This development stage will verify the catalytic selectivity of the catalyst designs presented here, and will allow

for further development of selective abiotic catalysts for the glucose oxidation and oxygen reduction reactions. In a third step, the fuel cell with selective electrodes would be placed in a single fuel stream which contains both fuels, **Figure 6.1 c**. This single-chamber device layout and operation mode of a ceramic-electrolyte glucose fuel cell would be applicable for actual implantation into the human body, where both electrodes would need to be in contact with the same fuel stream. This test would therefore be a realistic benchmark of functionality, to prepare for *in vivo* experimentation. It is important to note that the ceramic-electrolyte glucose fuel cell design presented in this thesis, employing a free-standing membrane architecture, lends itself for further development along this three-step pathway from dual-chamber to single-chamber glucose fuel cell operation. The silicon chip and fuel cell membrane system can be exposed to liquid on both sides if suitable modifications to the testing apparatus are implemented.

Single chamber operation will require further studies of the catalytic selectivity of both electrodes. Thus far, both electrodes have been designed with catalytic selectivity in mind, based on the different rate limiting steps of the glucose oxidation and oxygen reduction reaction, as reported in literature. However, this selectivity in the given design still needs to be proven. In particular, the present design makes use of a reactive sputtering fabrication route to fabricate nanoporous platinum, instead of the Raney-type process commonly employed in the literature. Unlike the Raney-type fabrication route, this reactive sputtering route does not employ sacrificial alloying metals, which may contribute to catalytic selectivity in previous studies due to modulations of the electronic structure in the platinum film. Therefore, an open question remains whether the reactive-sputtering-deposited nanoporous Pt anode employed here shows the same degree of catalytic selectivity as previous demonstrations of polymer-electrolyte glucose fuel cells. To verify and engineer this, simplified electrode model systems can be designed. For example, rotating disk electrodes are a common means to discern electron transfer reactions in catalytic systems, and could be employed to study the catalytic reactions on nanoporous platinum. Furthermore, in the single chamber design, concentration dependent studies can be performed, which determine the influence of glucose concentration on the oxygen reduction reaction and vice versa. Ultimately, it may be necessary to further engineer the catalytic selectivity of both electrode catalysts. This thesis provides an overview of various abiotic catalyst systems that have been explored for glucose fuel cells in the past, including carbon or noble metals beyond Pt. These materials, or composites of different materials, can serve as a starting point to further engineer selective catalysts for ceramic-electrolyte glucose fuel cells. In this endeavor, it is critical to ensure that all materials selected are compatible with microfabrication processes employed in semiconductor manufacturing, to ensure that any modified design still benefits from the ability to be fully integrated with bioelectronics.

Besides modifying the operation mode of the fuel cell, it will also be necessary to move toward fuels that more closely resemble body fluids. Here, simulated body fluids would be an appropriate expansion from the glucose/PBS solution that was used in the present work. Here, studies will be necessary which investigate the effect of other physiological endogenous substances on the glucose fuel cell operation, such as creatinine, ethanol, urea, ammonium chloride, or amino acids. These species, which are naturally present in body fluids, can create overpotentials, clogging, or catalyst poisoning, and thus measuring the ceramic-electrolyte glucose fuel cell's performance under such more realistic simulated body fluids is a reasonable next step. Ultimately, the ceramic-electrolyte glucose fuel cell should be operated in actual body fluid *in vitro*, as a final step prior to *in vivo* experimentation. *In vivo* experimentation, i.e., the actual implantation of a ceramic electrolyte glucose fuel cell into an organism, forms the final prototype demonstration that would be carried out after all previously mentioned operation steps. In vivo studies will be important to investigate long term performance, surface fouling, clogging of body fluids, and full device bio-compatibility. In particular, surface fouling of catalysts can become a challenge which will require further attention along the device development trajectory. Here, knowledge from implantable glucose sensors can help to develop adequate coatings, since implantable glucose sensors face similar challenges toward their long-term operation such as clogging and surface fouling.[209] Possible solutions include the use of a polyurethane membranes, which constitute a perm-selective membrane that can block the diffusion of endogenous species, and has been demonstrated to allow for implanted glucose sensor operation times of 56 days in rats.[210] Ultimately, i*n vivo* studies and subsequent clinical trials form the full demonstration and would complete the device development cycle from the inception and proof-of-concept that is presented in this thesis, all the way to implantation into the human body to power implantable devices that treat patients.

7. Biographical Notes and Publications

Philipp Simons was born in Mainz, Germany. He attended ETH Zurich in Zurich, Switzerland and graduated with a Bachelor of Science in Physics (with distinction) in 2013, and a Master of Science in Energy Science and Technology in 2015. During his Masters, he was a visiting student researcher at the California Institute of Technology in Pasadena, CA, USA, under the supervision of Prof. Sossina Haile, where he conducted research on the surface oxygen exchange kinetics of praseodymia-doped cerium oxide. Philipp Simons then joined CIMCO A/S in Copenhagen, Denmark as the Deputy General Manager, managing a team of 6 software developers and all day-to-day operations of the spin-off companies RapidCAM A/S and HSMTechnologies A/S. In 2016, he began his doctoral studies in Materials Science at ETH Zurich under the supervision of Prof. Jennifer L. M. Rupp, which he continued when he joined the Department of Materials Science and Engineering at the Massachusetts Institute of Technology in 2017. During his doctoral studies, Philipp Simons invented the first ceramic-electrolyte glucose fuel cell to power implantable medical devices, the smallest implantable power source to date and fully integrated into silicon technology for easy integration into miniaturized biomedical implants. His thesis research, at the intersection of biotechnology and energy conversion, demonstrated the first proof-of-concept of these nanoscale implantable power sources across over 150 fuel cells. Beyond device development, he investigated the proton transport properties of ceria and how cheap processing via spray pyrolysis can become an alternative pathway to assemble ceramic-electrolyte glucose fuel cells. Philipp Simons has received two of MIT's most prestigious graduate fellowships, namely the Hugh Hampton Young Memorial Fund Fellowship and the Broshy Graduate Fellowship. His research has been awarded the Displaying Futures Award by Merck KGaA, Darmstadt, Germany, worth $50,000, and he has received a best poster award at the 2018 MIT Materials Day and a Poster Pitch Award at the 2018 MIT Microsystems Annual Research Conference. Concurrently to his PhD, Philipp Simons is pursuing an MBA as a Leaders for Global Operations Fellow at the MIT Sloan School of Management.

Philipp Simons has co-authored the following publications and is a co-inventor of the following patent:

Publications

1) A Piezomicrobalance System for High-Temperature Mass Relaxation Characterization of Metal Oxides: A Case Study of Pr-Doped Ceria.
Philipp Simons*, Ho Il Ji, Timothy C. Davenport, Sossina M. Haile.* J. Am. Ceram. Soc. **2017**, 100 (3), 1161–1171.

2) Careful Choices in Low Temperature Ceramic Processing and Slow Hydration Kinetics Can Affect Proton Conduction in Ceria
Philipp Simons**, Kierstin P. Torres*, Jennifer L. M. Rupp.* Adv. Funct. Mater. **2021** *(accepted)*
**) Co-first authors*

3) Ceramic-Electrolyte Glucose Fuel Cell for Implantable Electronics
Philipp Simons*, Steven Schenk, Marco A. Gysel, Jennifer L. M. Rupp. (in revision)*

4) Deposition Parameters and Raman Crystal Orientation Measurements of Ceria Thin Films Deposited by Spray Pyrolysis
Philipp Simons**, Kierstin P. Torres*, Jennifer L. M. Rupp. (in revision)*
**) Co-first authors*

5) Design, Microfabrication and Testing Apparatus for Ceramic -Electrolyte Glucose Fuel Cells
Philipp Simons*, Steven Schenk, Marco A. Gysel, Jennifer L. M. Rupp. (in revision)*

6) Autonomous Cyber-Physical Manufacturing and Optimisation of Solid-State Batteries
Katarzyna P. Sokol, Jesse J. Hinricher, ***Philipp Simons****, Kun Joong Kim, Wojciech Matusik, Elsa Olivetti, Lincoln J. Miara, Jennifer L. M. Rupp. (in revision)*

7) A Sinter-Free Future for Solid-State Battery Designs
Zachary D. Hood, Yuntong Zhu, Lincoln J. Miara, Won Seok Chang, ***Philipp Simons****, Jennifer L. M. Rupp. (in revision)*

8) Pt-catalyzed D-Glucose Oxidation Reactions for Glucose Fuel Cells
Ji Huang, ***Philipp Simons****, Yusuke Sunada, Jennifer L. M. Rupp, Shunsuke Yagi. (in review)*

Patent

1) Solid State Glucose-Powered Micro Fuel Cell
Philipp Simons*, Jennifer L.M. Rupp.* US/15901732 (2018)

8. Appendix

8.1 Appendix A: Supplementary Information to Chapter 2

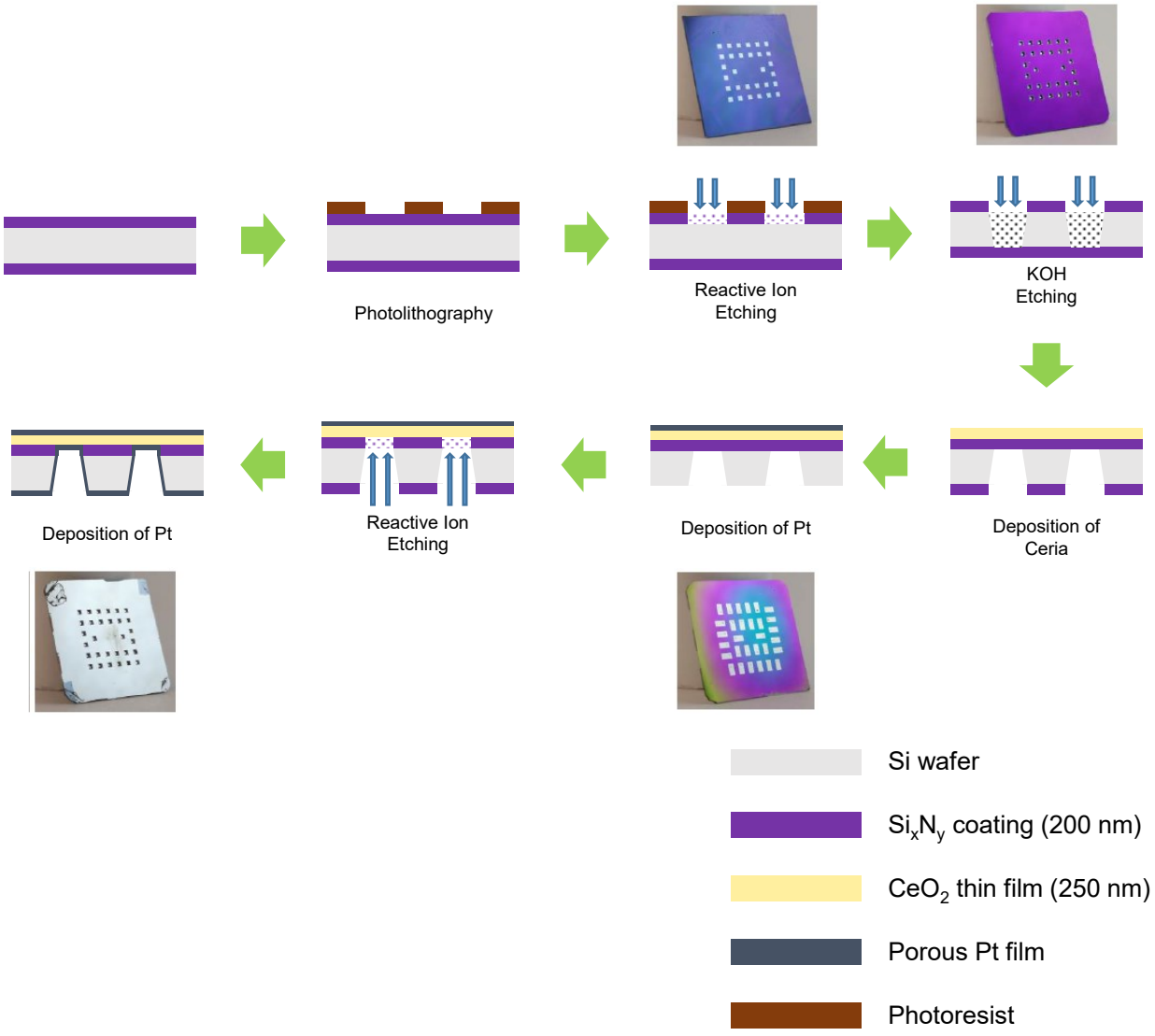

Figure 8.1 Microfabrication route to fabricate free-standing ceria membranes as glucose fuel cell devices.

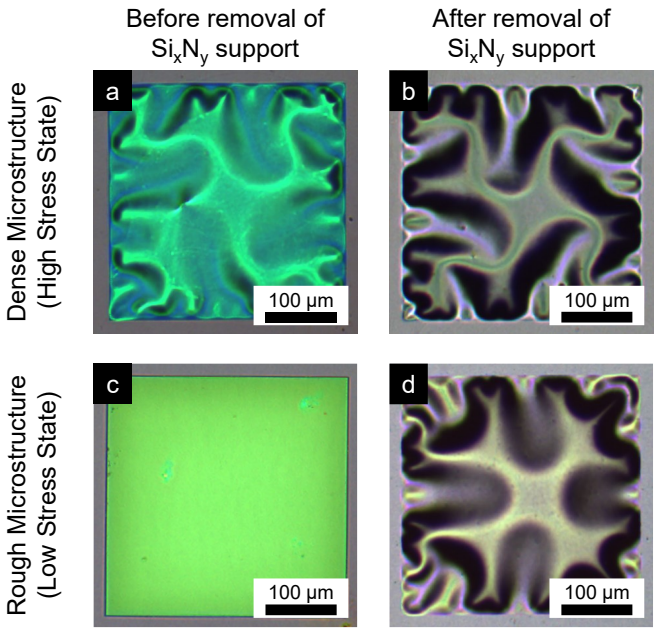

Figure 8.2 Optical micrographs of ceria membranes with dense **(a,b)** and porous **(c,d)** microstructure. Images **a)** and **c)** were captured before the deposition of the porous top-electrode and before the removal of the Si_xN_y support layer via reactive ion etching. Images **b)** and **d)** were captured after top-electrode deposition and Si_xN_y support layer removal. It can be seen that the dense microstructure shows a higher stress state, manifested in the more pronounced buckling pattern. For the porous microstructure, stress is released during deposition. In particular, before removal of the Si_xN_y support layer, the membrane with a rough microstructure does not show a visible buckling pattern at all, indicating significantly reduced stress in the film.

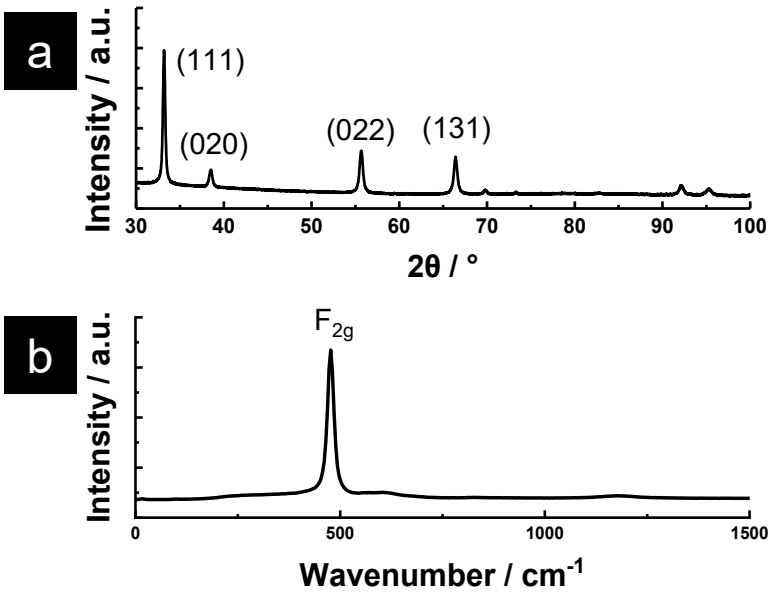

Figure 8.3 (a) X-ray diffraction pattern and **(b)** Raman spectrum of a ceria ceramic electrolyte thin film. The XRD pattern confirms the phase-pure, cubic fluorite structure of cerium oxide, in agreement with ICDD:00-067-0121. In the Raman spectrum, a single, sharp peak at 465 cm^{-1} is observed, corresponding to the F_{2g} oxygen breathing mode of cerium oxide. The data is in good agreement with the literature.[118]

Details on the analysis of electrochemical impedance spectroscopy results

In the model presented in ref [79] by Manabe et al., two arcs in the impedance spectrum refer inter and intra grain boundary proton conductivity, respectively, which both occur in the water layer adsorbed to the surface. However, the compressed nature of the impedance arcs observed here require an equivalent circuit model consisting of two serial R-Q-circuits, where Q denotes a constant phase element. We determine that a pure capacitor does not adequately reflect the behavior of the impedance spectra observed here, which implies that the surface roughness or spatial heterogeneities at interfaces modulated the capacitive impedance behavior.

Fit results:

$R_1 = 6{,}25 \cdot 10^7\ \Omega$

$Q_1 = 1.32 \cdot 10^{-9}\ S\ s^{n1}$

$n_1 = 0.871$

$R_2 = 9{,}95 \cdot 10^6\ \Omega$

$Q_2 = 7{,}58 \cdot 10^{-14}\ S\ s^{n2}$

$n = 0.63$

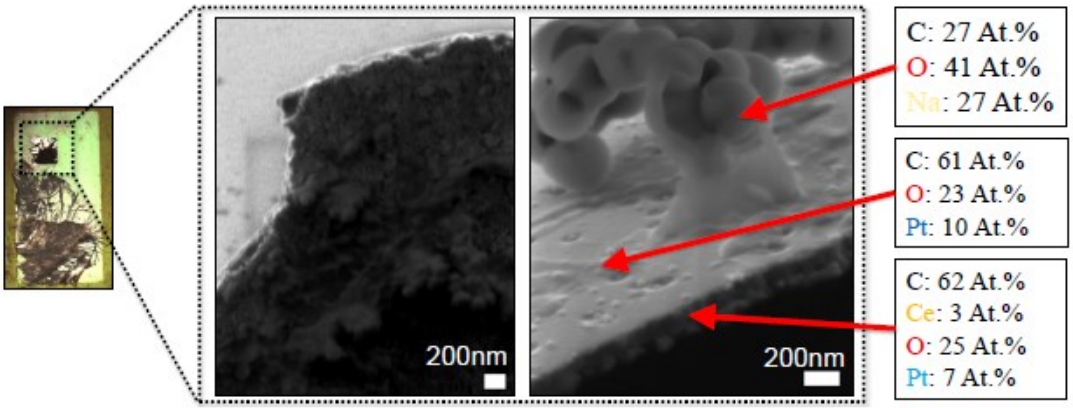

Figure 8.4 Precipitates observed during post-mortem analysis. SEM and EDS analysis shows that precipitates forming at the surface of glucose fuel cells are Na-containing depositions, i.e. likely salts precipitating from the glucose/PBS solution.

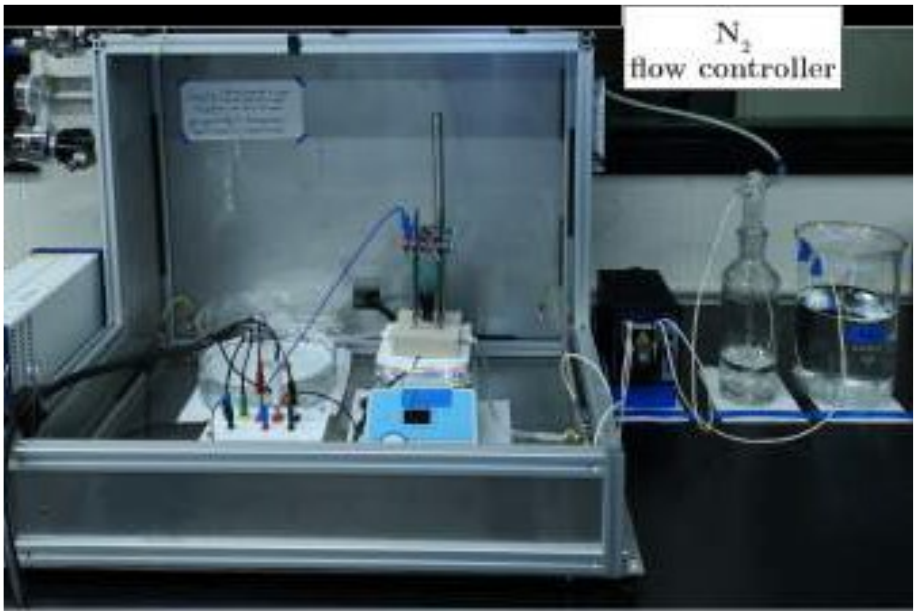

Figure 8.5 Measurement setup used to perform glucose fuel cell electrochemical performance measurements. Detailed accounts for the design of this setup are provided in Chapter 3 of this thesis.

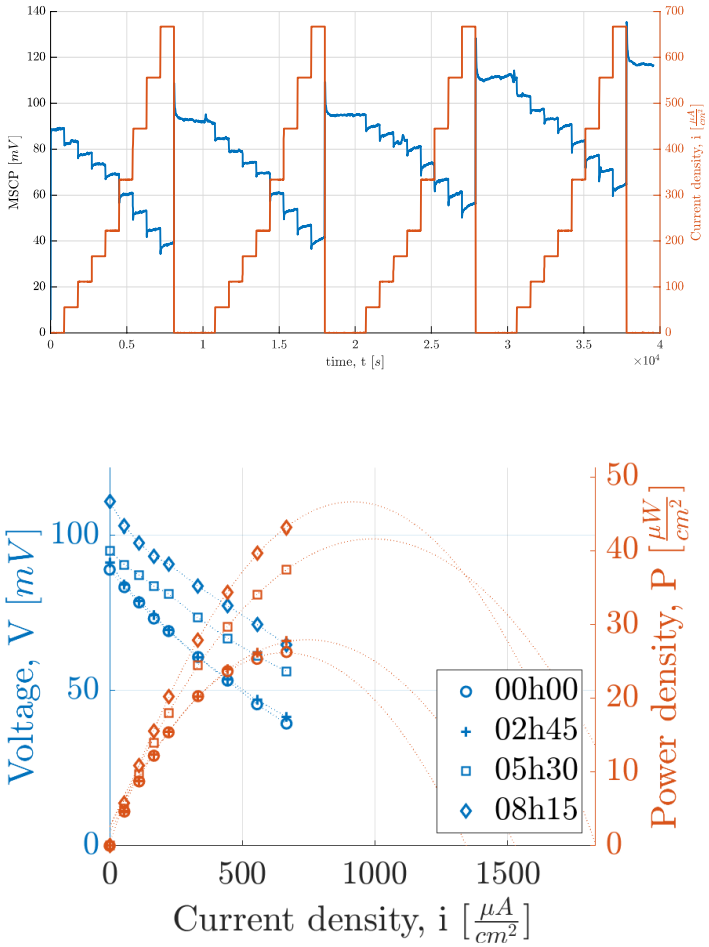

Figure 8.6 a) Exemplary time profile of fuel cell voltage and current density over the course of more than 10 hours. **b)** Voltage and power density as a function of time for record performing glucose fuel cell, extracted from the time series reported in **a)**.

8.2 Appendix B: Supplementary Information to Chapter 4

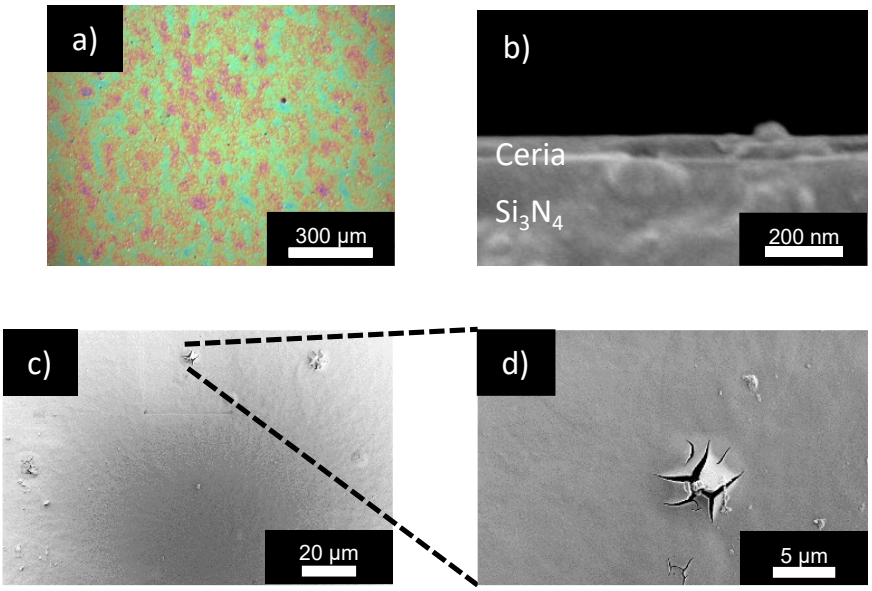

Figure 8.7 a) Optical micrograph of post-annealed film. **b)** Scanning electron micrograph of an un-annealed film, confirming a dense deposition. A large drift made thickness analysis impossible. **c)** Scanning electron micrograph of a post-annealed film with a small amount of cracks and **d)** magnified micrograph of a crack.

8.3 Appendix C: Supplementary Information to Chapter 5

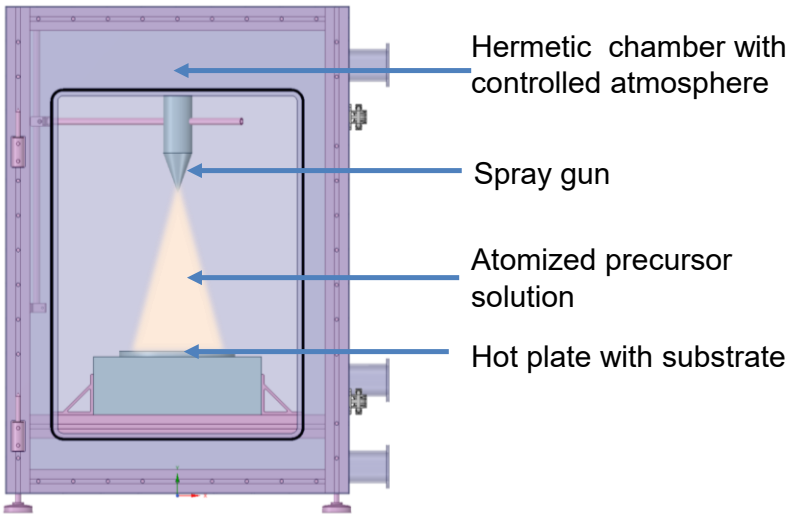

Figure 8.8 Schematic of spray pyrolysis deposition chamber

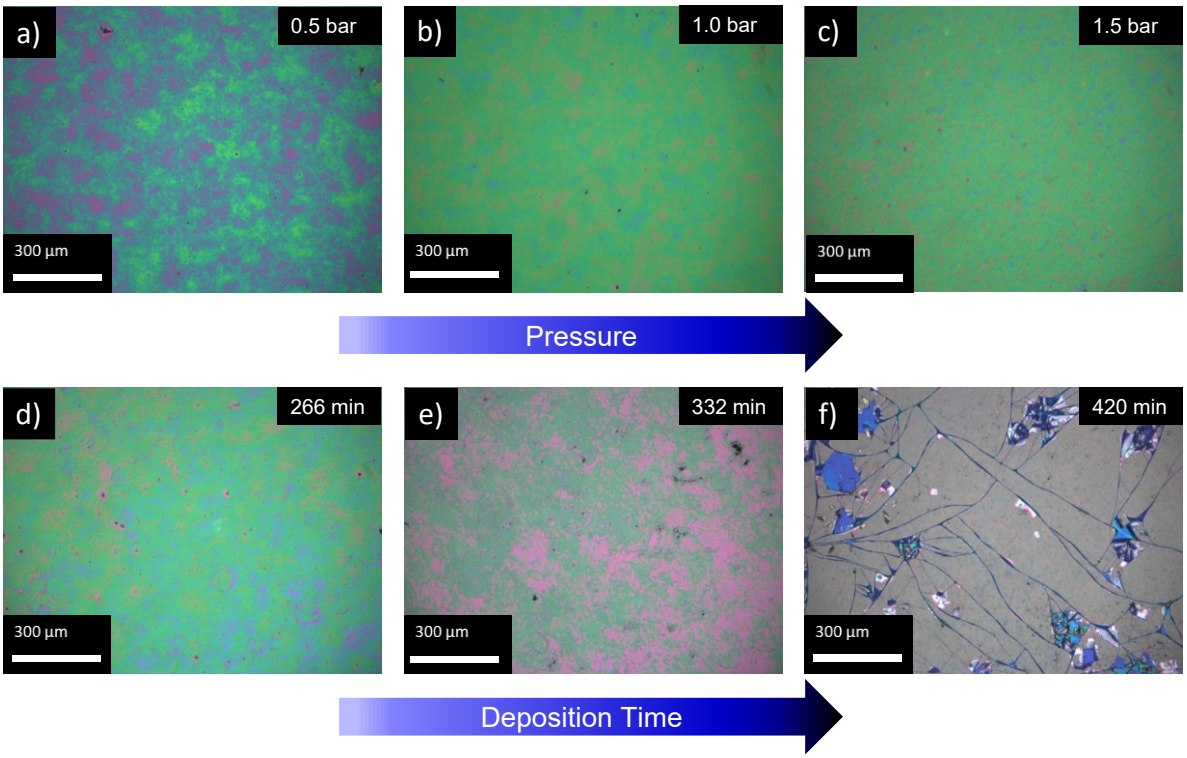

Figure 8.9 Optical micrograph of films deposited at an air pressure of **a)** 0.5 bar, **b)** 1.0 bar, and **c)** 1.5 at otherwise fixed deposition conditions. Optical micrograph of films deposited at **d)** 266 minutes, **e)** 332 minutes, and **f)** 420 minutes at otherwise fixed conditions (with the exception of **a)** being deposited at 0.6 bar and the others at 0.4 bar).

Discussion of the calibration of processing parameters for the spray pyrolysis deposition

The first step in this deposition analysis were to determine the optimal processing parameters towards depositing homogeneous, crack-free films. **Figure 8.9** displays optical micrographs of films deposited at varying spraying air pressures (**Figure 8.9 a-c**), but otherwise identical deposition conditions, and for different durations (**Figure 8.9 d-f**), also at otherwise identical conditions. Increasing the air pressure from 0.5 to 1.0 bar resulted in more homogeneous films, as seen in **Figure 8.9 a-c**. At higher pressures, the droplet size of the precursor decreases, allowing for more uniform films as seen by the even color distribution in the optical micrograph. In contrast, at lower pressures, droplets are larger, creating an inhomogeneous morphology as can be seen from the color pattern where individual droplet residues can be seen, causing color changes due to large thickness irregularities. The films deposited at 1.0 and 1.5 bars of air pressure only show slight morphology deviations, so a 1.0 bar pressure was used for subsequent depositions. The impact of spraying duration also proved to be critical towards depositing high-quality films. It was seen that spraying for 7 hours at a flow rate of 3 mL/hr resulted in cracked films (**Figure 8.9 f**). Generally, it was observed that longer depositions of thicker films resulted in cracked films whereas shorter depositions with otherwise identical deposition conditions led to intact films. This implies that there exists a critical film thickness, above which crack formation becomes favorable over dense, crack-free film deposition. Critical thickness is discussed in detail in chapter 5, and the energetics leading to crack formation in general are governed by the Griffith criterion:

$$\Delta U_{crack} = 2\gamma a - \Delta U_{released\ strain}$$

where ΔU_{crack} corresponds to the total internal energy difference associated with the formation of a crack, and $\Delta U_{released\ strain}$ corresponds to the internal energy difference of releasing strain energy through the crack formation. γ represents the surface energy, a the crack length, and the factor of 2 is present because cracking forms two surfaces. We can see that if the amount of released strain energy is greater than the surface energy term, the formation of cracks becomes energetically favorable.

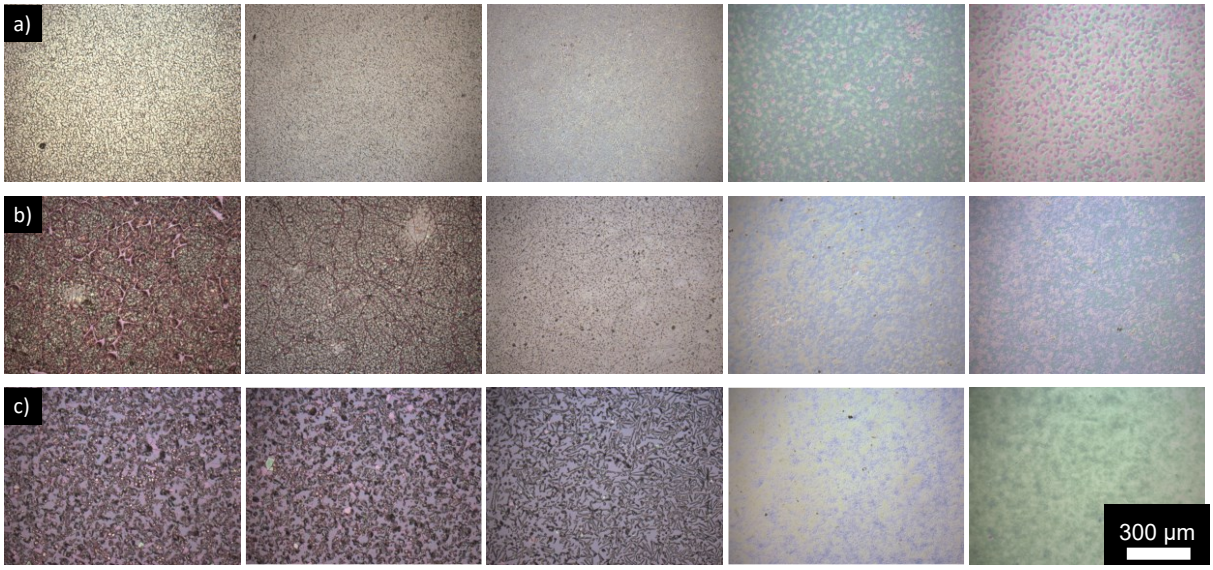

Figure 8.10 Micrograph of film along wafer from left to right: center, 1-4 cm from the center deposited at a) 350 C, b) 400 °C, and c) 450 °C. Scale bar valid for all micrographs.

8.4 Appendix D: Preliminary Mechanistic Studies of Losses in the Ceramic-Electrolyte Glucose Fuel Cell System

It is critical to understand the sources of losses in the glucose fuel cell system in order to engineer device performance. Among the glucose fuel cell performance data presented in this thesis, it is noteworthy that the observed OCV is generally between 10x to 100x below the theoretical electrochemical potential of the glucose-oxygen oxidation reaction. It is therefore desirable to understand the reason for this significantly lowered OCV. Some hypotheses for the sources of loss in the fuel cell system are electronic leakage due to electronic conductivity of the electrolyte or the formation of pin-holes during glucose fuel cell fabrication. A low overall proton conduction could also be the source of the low OCV, however, this explanation is likely giving the comparatively good power output performance of ceramic-electrolyte glucose fuel cells relative to the OCV performance.

To further explore these sources of losses, first mechanistic studies were performed using electrochemical impedance spectroscopy (EIS). EIS is a widely used tool to discern different contributions to charge transport resistance in electrochemical systems, and can provide useful insights into the transport processes occurring at different components of an electrochemical system.

We performed electrochemical impedance spectroscopy while distorting the glucose fuel cell system from equilibrium, by measuring impedance under different voltage biases and different temperatures. We first discuss the temperature-dependent response, and then the voltage dependent response.

The temperature-dependent impedances, as well as extracted total conductivities are displayed in **Figure 8.11**. The impedance was measured in a Linkam stage under dry air. The observed activation energy for the total conductivity in this temperature regime was 0.35 eV. This is in good agreement with electronic transport in pure and doped ceria, providing a first indication that electronic leakage can indeed be a major source of loss in the system.[133]

Secondly, the bias-dependent impedance was explored, **Figure 8.12**. Here, we qualitatively observe a strong bias-dependence of the electrochemical impedance of the glucose fuel cell system, with decreasing impedance for increasing bias voltage. This provides additional indications that interfacial transport is governing the conduction in the system, since typically, the interface and grain boundaries show a bias dependence in the electrochemical impedance spectrum. However, since these measurements were taken under dry conditions, further studies under moist and dry conditions, as well as *operando* are required to more fully understand the electrochemical mechanisms of the ceramic-electrolyte glucose fuel cell.

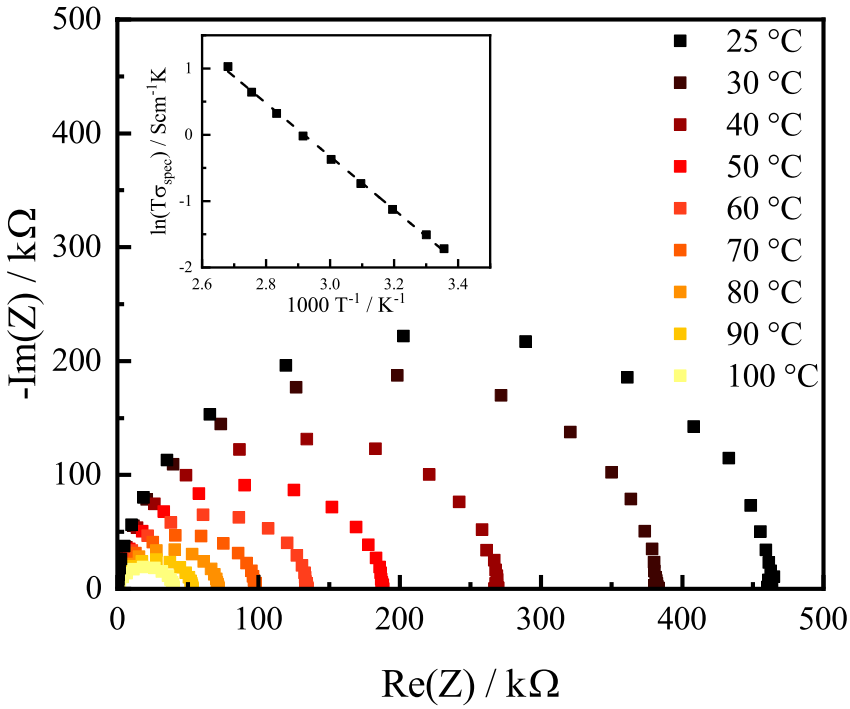

Figure 8.11 Temperature-dependent electrochemical impedance spectroscopy performed under dry air, and extracted total conductivity plotted in an Arrhenius-type plot. The observed activation energy is 0.35 eV, which is in good agreement with electronic conductivity in ceria.

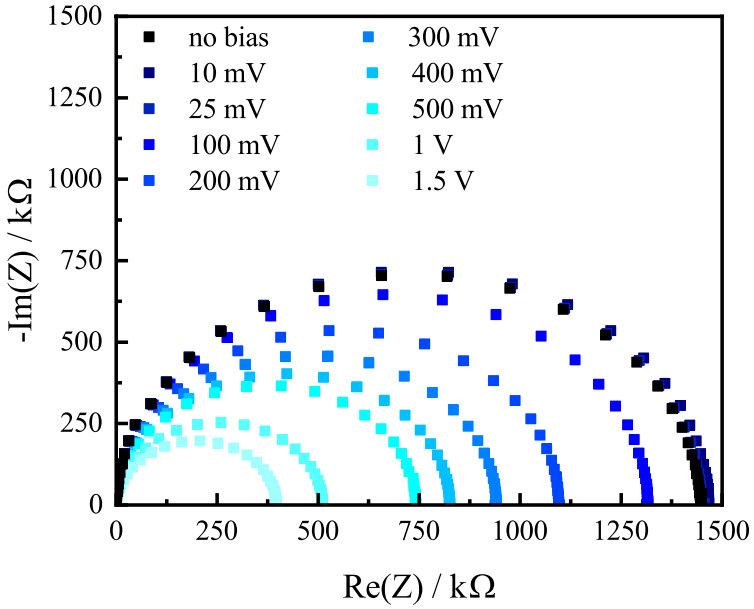

Figure 8.12 Electrochemical impedance spectroscopy under bias, performed under dry air conditions. A decreasing impedance with increasing bias indicates that grain boundaries or interfaces are dominant in charge transport at these temperatures.

Importantly, the results presented here were obtained under dry air, and measurements under humidified air or liquid water were inconclusive. The results provide some first indications that the major source of reduced OCV is electronic leakage, which means that future studies should explore methods to increase the protonic transference number, e.g., through doping of the ceria electrolyte.

9. References

[1] B. Hirschler, *GSK and Google parent forge $715 million bioelectronic medicines firm*, Reuters.

[2] D. Seo, R. M. Neely, K. Shen, U. Singhal, E. Alon, J. M. Rabaey, J. M. Carmena, M. M. Maharbiz, *Neuron* **2016**, *91*, 529.

[3] Ryan Cross, *C&EN Glob. Enterp.* **2020**, *98*, 14.

[4] P. A. Bleszynski, J. G. Y. Luc, P. Schade, S. J. Phillips, V. Tchantchaleishvili, *ASAIO J.* **2016**, *62*, 639.

[5] J. E. Poole, M. J. Gleva, T. Mela, M. K. Chung, D. Z. Uslan, R. Borge, V. Gottipaty, T. Shinn, D. Dan, L. A. Feldman, H. Seide, S. A. Winston, J. J. Gallagher, J. J. Langberg, K. Mitchell, R. Holcomb, *Results From Replace Regist.* **2010**, *122*, 1553.

[6] S. Kerzenmacher, J. Ducrée, R. Zengerle, F. von Stetten, *J. Power Sources* **2008**, *182*, 1.

[7] S. C. Barton, J. Gallaway, P. Atanassov, *Chem. Rev.* **2004**, *104*, 4867.

[8] Ó. Santiago, E. Navarro, M. A. Raso, T. J. Leo, *Appl. Energy* **2016**, *179*, 497.

[9] L. An, T. S. Zhao, S. Y. Shen, Q. X. Wu, R. Chen, *J. Power Sources* **2011**, *196*, 186.

[10] R. S. Sanders, In *Cardiac Pacing for the Clinician* (Eds.: Kusumoto, F. M.; Goldschlager, N. F.), Springer US, Boston, MA, **2008**, pp. 47–71.

[11] W. Greatbatch, J. H. Lee, W. Mathias, M. Eldridge, J. R. Moser, A. A. Schneider, *IEEE Trans. Biomed. Eng.* **1971**, *BME-18*, 317.

[12] D. C. Bock, A. C. Marschilok, K. J. Takeuchi, E. S. Takeuchi, *Batteries used to power implantable biomedical devices*, Vol. 84, NIH Public Access, **2012**, pp. 155–164.

[13] A. Kim, M. Ochoa, R. Rahimi, B. Ziaie, *IEEE Access* **2015**, *3*, 89.

[14] J. C. Schuder, *Artif. Organs* **2002**, *26*, 909.

[15] R. Venkatasubramanian, C. Watkins, C. Caylor, G. Bulman, *PowerMEMS 2006. 6th Int. Work. Micro Nanotechnol. Power Gener. Energy Convers. Appl.* **2006**, 1.

[16] Y. Yang, X. J. Wei, J. Liu, *J. Phys. D. Appl. Phys.* **2007**, *40*, 5790.

[17] Q. Zheng, B. Shi, F. Fan, X. Wang, L. Yan, W. Yuan, S. Wang, H. Liu, Z. Li, Z. L. Wang, *Adv. Mater.* **2014**, *26*, 5851.

[18] W. Jiang, H. Li, Z. Liu, Z. Z. Li, J. Tian, B. Shi, Y. Zou, H. Ouyang, C. Zhao, L. Zhao, R. Sun, H. Zheng, Y. Fan, Z. L. Wang, Z. Z. Li, *Adv. Mater.* **2018**, *30*, 1.

[19] G. T. Hwang, H. Park, J. H. Lee, S. Oh, K. Il Park, M. Byun, H. Park, G. Ahn, C. K. Jeong, K. No, H. Kwon, S. G. Lee, B. Joung, K. J. Lee, *Adv. Mater.* **2014**, *26*, 4880.

[20] Z. Yang, S. Zhou, J. Zu, D. Inman, *Joule* **2018**, *2*, 642.

[21] W. Greatbatch, C. F. Holmes, *IEEE Eng. Med. Biol. Mag.* **2002**, *10*, 38.

[22] V. S. Mallela, V. Ilankumaran, S. N. Rao, *Indian Pacing Electrophysiol. J.* **2004**, *4*, 201.

[23] A. Kloke, C. Köhler, R. Gerwig, R. Zengerle, S. Kerzenmacher, *Adv. Mater.* **2012**, *24*, 2916.

[24] G. Wohlfahrt, S. Witt, J. Hendle, D. Schomburg, H. M. Kalisz, H. J. Hecht, *Acta Crystallogr. Sect. D Biol. Crystallogr.* **1999**, *55*, 969.

[25] B. E. Logan, *Microbial Fuel Cells*, **2008**.

[26] F. Davis, S. P. Higson, *Biosens Bioelectron* **2007**, *22*, 1224.

[27] V. Oncescu, D. Erickson, *Sci Rep* **2013**, *3*, 1226.

[28] S. Rengaraj, P. Kavanagh, D. Leech, *Biosens. Bioelectron.* **2011**, *30*, 294.

[29] B. I. Rapoport, J. T. Kedzierski, R. Sarpeshkar, *PLoS One* **2012**, *7*.

[30] C. K. Colton, R. F. Drake, *ASAIO J.* **1969**, *15*.

[31] J. O. M. Bockris, B. J. Piersma, E. Gileadi, *Electrochim. Acta* **1964**, *9*, 1329.

[32] A. T. Yahiro, S. M. Lee, D. O. Kimble, *Biochim. Biophys. Acta* **1964**, *88*, 375.

[33] H. Warner, B. W. Robinson, *Digest of the Seventh International Conference on Medical and Biological Engineering* (Ed.: Jacobson, B.), Ingenjörsvetenskapsakademi, Stockholm, Stockholm, **1967**.

[34] R. F. Drake, B. K. Kusserow, S. Messinger, S. Matsuda, *ASAIO J.* **1970**, *16*.

[35] S. K. J. Wolfson, S. J. Yao, A. Geisel, H. R. J. Cash, *ASAIO J.* **1970**, *16*.

[36] J. H. Fishman, J. F. Henry, *Electrochem. Biosci. Bioeng.* **1973**, 199.

[37] M. Falk, C. W. Narváez Villarrubia, S. Babanova, P. Atanassov, S. Shleev, *ChemPhysChem* **2013**, *14*, 2045.

[38] R. J. Rao, G. Richter, F. von Sturm, E. Weidlich, *Berichte der Bunsengesellschaft für Phys. Chemie* **1973**, *77*, 787.

[39] S. Kerzenmacher, U. Kräling, M. Schroeder, R. Brämer, R. Zengerle, F. von Stetten, *J. Power Sources* **2010**, *195*, 6524.

[40] S. Kerzenmacher, M. Schroeder, R. Brämer, R. Zengerle, F. von Stetten, *J. Power Sources* **2010**, *195*, 6516.

[41] S. Kerzenmacher, U. Kräling, T. Metz, R. Zengerle, F. von Stetten, *J. Power Sources* **2011**, *196*, 1264.

[42] A. Kloke, B. Biller, U. Kräling, S. Kerzenmacher, R. Zengerle, F. von Stetten, *Fuel Cells* **2011**, *11*, 316.

[43] A. Zebda, C. Gondran, A. Le Goff, M. Holzinger, P. Cinquin, S. Cosnier, *Nat. Commun.* **2011**, *2*.

[44] V. Kumar, A. K. Abbas, N. Fausto, *Robbins and Cotran pathologic basis of disease.*, 7th ed., Elsevier Saunders, Philadelphia, **2005**.

[45] D. G. Maggs, R. Jacob, F. Rife, R. Lange, P. Leone, M. J. During, W. V. Tamborlane, R. S. Sherwin, *J. Clin. Invest.* **1995**, *96*, 370.

[46] A. H. Ropper, M. A. Samuels, J. P. Klein, S. Prasad, *Adams and Victor's Principles of Neurology*, 11th ed., McGraw-Hill Education, New York, **2019**.

[47] R. C. Reid, S. D. Minteer, B. K. Gale, *Biosens. Bioelectron.* **2015**, *68*, 142.

[48] E. Fabbri, D. Pergolesi, E. Traversa, *Chem. Soc. Rev.* **2010**, *39*, 4355.

[49] K. D. Kreuer, *Annu. Rev. Mater. Res.* **2003**, *33*, 333.

[50] S. Choi, C. J. Kucharczyk, Y. Liang, X. Zhang, I. Takeuchi, H. Il Ji, S. M. Haile, *Nat. Energy* **2018**, *3*, 202.

[51] T. Seiyama, N. Yamazoe, H. Arai, **1983**, *4*, 86.

[52] T. Nitta, *Ind. Eng. Chem. Prod. Res. Dev.* **1981**, *20*, 669.

[53] T. Nitta, Z. Terada, S. Hayakawa, *J. Am. Ceram. Soc.* **1980**, *63*, 295.

[54] N. Barsan, U. Weimar, *J. Electroceramics* **2001**, *7*, 143.

[55] F. Messerschmitt, M. Kubicek, J. L. M. Rupp, *Adv. Funct. Mater.* **2015**, *25*, 5117.

[56] F. Messerschmitt, M. Jansen, J. L. M. Rupp, *Adv. Electron. Mater.* **2018**, *4*, 1.

[57] E. Sediva, W. J. Bowman, J. C. Gonzalez-Rosillo, J. L. M. Rupp, *Adv. Electron. Mater.* **2019**, *5*, 1.

[58] Y. F. Chang, B. Fowler, Y. C. Chen, F. Zhou, C. H. Pan, T. C. Chang, J. C. Lee, *Sci. Rep.* **2016**, *6*, 1.

[59] M. Lübben, S. Wiefels, R. Waser, I. Valov, *Adv. Electron. Mater.* **2018**, *4*, 1.

[60] A. J. Tan, M. Huang, S. Sheffels, F. Büttner, S. Kim, A. H. Hunt, I. Waluyo, H. L. Tuller, G. S. D. Beach, *Phys. Rev. Mater.* **2019**, *3*, 1.

[61] A. J. Tan, M. Huang, C. O. Avci, F. Büttner, M. Mann, W. Hu, C. Mazzoli, S. Wilkins, H. L. Tuller, G. S. D. Beach, *Nat. Mater.* **2019**, *18*, 35.

[62] Y. Yamazaki, R. Hernandez-Sanchez, S. M. Haile, *Chem. Mater.* **2009**, *21*, 2755.

[63] H. G. Bohn, T. Schober, *J. Am. Ceram. Soc.* **2000**, *83*, 768.

[64] R. C. T. Slade, N. Singh, *Solid State Ionics* **1991**, *46*, 111.

[65] K. Katahira, Y. Kohchi, T. Shimura, H. Iwahara, *Solid State Ionics* **2000**, *138*, 91.

[66] K. D. Kreuer, S. Adams, W. Münch, A. Fuchs, U. Klock, J. Maier, *Solid State Ionics* **2001**, *145*, 295.

[67] J. R. Brown, E. Mastromatteo, J. Horwood, *Am. Ind. Hyg. Assoc. J.* **1963**, *24*, 131.

[68] S. M. Haile, G. Lentz, K. D. Kreuer, J. Maier, *Solid State Ionics* **1995**, *77*, 128.

[69] D. A. Boysen, T. Uda, C. R. I. Chisholm, S. M. Haile, *Science.* **2004**, *303*, 68.

[70] S. M. Haile, D. A. Boysen, C. R. I. Chisholm, R. B. Merle, *Nature* **2001**, *410*, 910.

[71] M. Doyle, G. Rajendran, In *Handbook of Fuel Cells*, John Wiley & Sons, Ltd, Chichester, UK, **2010**.

[72] Y. Sone, P. Ekdunge, D. Simonsson, *J. Electrochem. Soc.* **1996**, *143*, 1254.

[73] S. M. Haile, C. R. I. Chisholm, K. Sasaki, D. A. Boysen, T. Uda, In *Faraday Discussions*, The Royal Society of Chemistry, **2007**, pp. 17–39.

[74] K. D. Kreuer, *J. Memb. Sci.* **2001**, *185*, 29.

[75] B. Smitha, S. Sridhar, A. A. Khan, *J. Memb. Sci.* **2005**, *259*, 10.

[76] M. S. A. Kamel, H. F. M. Mohamed, M. O. Abdel-Hamed, E. E. Abdel-Hady, *J. Solid State Electrochem.* **2019**, *23*, 2639.

[77] G. Alberti, M. Casciola, L. Massinelli, B. Bauer, *J. Memb. Sci.* **2001**, *185*, 73.

[78] J. P. Agalloco, J. E. Akers, R. E. Madsen, *Moist heat sterilization - Myths and realities*, Vol. 52, **1998**.

[79] R. Manabe, S. Ø. Stub, T. Norby, Y. Sekine, *Solid State Commun.* **2018**, *270*, 45.

[80] S. Stub, E. Vøllestad, T. Norby, *J. Mater. Chem. A* **2018**, *6*, 8265.

[81] S. Ø. Stub, E. Vøllestad, T. Norby, *J. Phys. Chem. C* **2017**, *121*, 12817.

[82] M. Shirpour, G. Gregori, R. Merkle, J. Maier, *Phys. Chem. Chem. Phys.* **2011**, *13*, 937.

[83] G. Gregori, M. Shirpour, J. Maier, *Adv. Funct. Mater.* **2013**, *23*, 5861.

[84] T. S. Oh, D. A. Boyd, D. G. Goodwin, S. M. Haile, *Phys. Chem. Chem. Phys.* **2013**, *15*, 2466.

[85] H. J. Avila-Paredes, C. T. Chen, S. Wang, R. A. De Souza, M. Martin, Z. Munir, S. Kim, *J. Mater. Chem.* **2010**, *20*, 10110.

[86] S. Kim, H. J. Avila-Paredes, S. Wang, C.-T. Chen, R. A. De Souza, M. Martin, Z. A. Munir, *Phys. Chem. Chem. Phys.* **2009**, *11*, 3035.

[87] H. J. Avila-Paredes, J. Zhao, S. Wang, M. Pietrowski, R. A. De Souza, A. Reinholdt, Z. A. Munir, M. Martin, S. Kim, *J. Mater. Chem.* **2010**, *20*, 990.

[88] D. Beckel, A. Bieberle-Hütter, A. Harvey, A. Infortuna, U. P. Muecke, M. Prestat, J. L. M. Rupp, L. J. Gauckler, *J. Power Sources* **2007**, *173*, 325.

[89] Y. Shi, I. Garbayo, P. Muralt, J. L. Marguerite Rupp, *J. Mater. Chem. A* **2017**, *5*, 3900.

[90] Y. Shi, A. H. Bork, S. Schweiger, J. L. M. Rupp, *Nat. Mater.* **2015**, *14*, 721.

[91] S. Kim, U. Anselmi-Tamburini, H. J. Park, M. Martin, Z. A. Munir, *Adv. Mater.* **2008**, *20*, 556.

[92] K. D. Kreuer, *Solid State Ionics* **1997**, *94*, 55.

[93] Electroceuticals/Bioelectric Medicine Market Size, Share & Analysis, **2020**.

[94] K. Famm, B. Litt, K. J. Tracey, E. S. Boyden, M. Slaoui, *Nature* **2013**, *496*, 159.

[95] K. Birmingham, V. Gradinaru, P. Anikeeva, W. M. Grill, V. Pikov, B. McLaughlin, P. Pasricha, D. Weber, K. Ludwig, K. Famm, *Nat. Rev. Drug Discov.* **2014**, *13*, 399.

[96] H. G. Mond, G. Freitag, *PACE - Pacing Clin. Electrophysiol.* **2014**, *37*, 1728.

[97] A. Ben Amar, A. B. Kouki, H. Cao, *Sensors* **2015**, *15*, 28889.

[98] Y. Lee, D. Blaauw, D. Sylvester, *Proc. IEEE* **2016**, *104*, 1529.

[99] Y. Zhu, Z. Hood, J. C. Gonzalez-Rosillo, M. Balaish, K. J. Kim, J. L. M. Rupp, *Nat. Mater. Rev.* **2020**, Manuscript in Preapration (Invited).

[100] D. Leech, P. Kavanagh, W. Schuhmann, *Electrochim. Acta* **2012**, *84*, 223.

[101] J. T. Santini, M. J. Cima, R. Langer, *Nature* **1999**.

[102] A. L. Benabid, P. Pollak, A. Louveau, S. Henry, J. de Rougemont, *Stereotact. Funct. Neurosurg.* **1987**, *50*, 344.

[103] J. Wessberg, C. R. Stambaugh, J. D. Kralik, P. D. Beck, M. Laubach, J. K. Chapin, J. Kim, S. J. Biggs, M. A. Srinivasan, M. A. L. Nicolelis, *Nature* **2000**, *408*, 361.

[104] Z. L. Wang, J. Song, *Science.* **2006**, *312*, 242.

[105] F. R. Fan, Z. Q. Tian, Z. Lin Wang, *Nano Energy* **2012**.

[106] S. R. Samms, S. Wasmus, R. F. Savinell, *J. Electrochem. Soc.* **1996**, *143*, 1498.

[107] A. Evans, A. Bieberle-Hütter, J. L. M. M. Rupp, L. J. Gauckler, *J. Power Sources* **2009**, *194*, 119.

[108] Z. Shao, S. M. Haile, *Nature* **2010**, *3*, 255.

[109] E. D. Wachsman, K. T. Lee, *Lowering the temperature of solid oxide fuel cells*, Vol. 334, American Association for the Advancement of Science, **2011**, pp. 935–939.

[110] D. J. L. Brett, A. Atkinson, N. P. Brandon, S. J. Skinner, *Chem. Soc. Rev.* **2008**, *37*, 1568.

[111] S. Li, J. T. S. Irvine, *Solid State Ionics* **2021**, *361*, 115571.

[112] D. Pergolesi, E. Fabbri, A. D'epifanio, E. Di Bartolomeo, A. Tebano, S. Sanna, S. Licoccia, G. Balestrino, E. Traversa, **2010**.

[113] C. Walkey, S. Das, S. Seal, J. Erlichman, K. Heckman, L. Ghibelli, E. Traversa, J. F. McGinnis, W. T. Self, *Environ. Sci. Nano* **2015**, *2*, 33.

[114] C. Piconi, G. Maccauro, *Biomaterials* **1999**, *20*, 1.

[115] C. Xu, X. Qu, *NPG Asia Mater.* **2014**, *6*.

[116] J. R. Rao, In *Bioelectrochemistry I. Biological Redox Reactions* (Eds.: Milazzo, G.; Blank, M.), Plenum Press, New York, **1983**, pp. 283–335.

[117] A. Infortuna, A. S. Harvey, L. J. Gauckler, *Adv. Funct. Mater.* **2008**, *18*, 127.

[118] R. Schmitt, A. Nenning, O. Kraynis, R. Korobko, A. I. Frenkel, I. Lubomirsky, S. M. Haile, J. L. M. Rupp, *Chem. Soc. Rev.* **2020**, *49*, 554.

[119] W. Jung, J. J. Kim, H. L. Tuller, *J. Power Sources* **2015**, *275*, 860.

[120] J. L. M. Rupp, U. P. Muecke, P. C. Nalam, L. J. Gauckler, *J. Power Sources* **2010**, *195*, 2669.

[121] A. Bieberle-Hütter, P. Reinhard, J. L. M. Rupp, L. J. Gauckler, *J. Power Sources* **2011**, *196*, 6070.

[122] P. Simons, K. P. Torres, J. L. M. Rupp, *Prep.* **2021**.

[123] C. Köhler, M. Frei, R. Zengerle, S. Kerzenmacher, *ChemElectroChem* **2014**, *1*, 1895.

[124] A. Kloke, C. Köhler, R. Zengerle, S. Kerzenmacher, *J. Phys. Chem. C* **2012**, *116*, 19689.

[125] S. Kerzenmacher, J. Ducrée, R. Zengerle, F. von Stetten, *J. Power Sources* **2008**, *182*, 66.

[126] S. Ghaffari, M. R. Mousavi, M. Salehieh, *Proc. - Int. Conf. Intell. Syst. Model. Simulation, ISMS* **2013**, 148.

[127] A. Tschöpe, R. Birringer, *J. Electroceramics* **2001**, *7*, 169.

[128] E. Meng, T. Hoang, *Ther. Deliv.* **2012**, *3*, 1457.

[129] R. Sobot, *IEEE Technol. Soc. Mag.* **2018**, *37*, 35.

[130] P. Simons, S. A. Schenk, M. A. Gysel, L. F. Olbrich, J. L. M. Rupp, **2021**, Prep.

[131] P. Simons, J. L. M. Rupp, *Solid State Glucose-Powered Micro Fuel Cell.*, USA, **2018**.

[132] M. L. B. Rao, R. F. Drake, *J. Electrochem. Soc.* **1969**, *116*, 334.

[133] H. L. Tuller, A. S. Nowick, *J. Phys. Chem. Solids* **1977**, *38*, 859.

[134] J. K. Norskov, T. Bligaard, J. Rossmeisl, C. H. Christensen, J. K. Nørskov, T. Bligaard, J. Rossmeisl, C. H. Christensen, *Nat. Chem.* **2009**, *1*, 37.

[135] U. P. Do, F. Seland, M. M. Maharbiz, K. Wang, Ø. Johannesen, E. A. Johannessen, *J. Mater. Sci.* **2016**, *51*, 9095.

[136] E. Sediva, W. J. Bowman, J. C. Gonzalez-Rosillo, J. L. M. Rupp, *Adv. Electron. Mater.* **2019**, *5*, 1800566.

[137] Y. F. Chang, B. Fowler, Y. C. Chen, F. Zhou, C. H. Pan, T. C. Chang, J. C. Lee, *Sci. Rep.* **2016**, *6*, 21268.

[138] M. Lübben, S. Wiefels, R. Waser, I. Valov, *Adv. Electron. Mater.* **2018**, *4*, 1700458.

[139] F. Messerschmitt, M. Jansen, J. L. M. Rupp, *Adv. Electron. Mater.* **2018**, *4*, 1800282.

[140] Y. Meng, J. Gao, Z. Zhao, J. Amoroso, J. Tong, K. S. Brinkman, *J. Mater. Sci.* **2019**, *54*, 9291.

[141] T. Sancho, J. Soler, M. P. Pina, *J. Power Sources* **2007**, *169*, 92.

[142] F. M. B. Marques, V. V. Kharton, E. N. Naumovich, A. L. Shaula, A. V. Kovalevsky, A. A. Yaremchenko, *Solid State Ionics* **2006**, *177*, 1697.

[143] C. Tandé, D. Pérez-Coll, G. C. Mather, *J. Mater. Chem.* **2012**, *22*, 11208.

[144] B. Scherrer, M. V. F. Schlupp, D. Stender, J. Martynczuk, J. G. Grolig, H. Ma, P. Kocher, T. Lippert, M. Prestat, L. J. Gauckler, *Adv. Funct. Mater.* **2013**, *23*, 1957.

[145] F. Maglia, I. G. Tredici, G. Spinolo, U. Anselmi-Tamburini, *J. Mater. Res.* **2012**, *27*, 1975.

[146] J. L. M. Rupp, B. Scherrer, A. S. Harvey, L. J. Gauckler, *Adv. Funct. Mater.* **2009**, *19*, 2790.

[147] J. L. M. Rupp, B. Scherrer, L. J. Gauckler, *Phys. Chem. Chem. Phys.* **2010**, *12*, 11114.

[148] J. L. M. Rupp, B. Scherrer, N. Schäuble, L. J. Gauckler, *Adv. Funct. Mater.* **2010**, *20*, 2807.

[149] J. L. M. Rupp, L. J. Gauckler, *Solid State Ionics* **2006**, *177*, 2513.

[150] B. Scherrer, J. Martynczuk, H. Galinski, J. G. Grolig, S. Binder, A. Bieberle-Hütter, J. L. M. Rupp, M. Prestat, L. J. Gauckler, *Adv. Funct. Mater.* **2012**, *22*, 3509.

[151] D. Perednis, O. Wilhelm, S. E. Pratsinis, L. J. Gauckler, *Thin Solid Films* **2005**, *474*, 84.

[152] M. Avrami, *J. Chem. Phys.* **1939**, *7*, 1103.

[153] M. Avrami, *J. Chem. Phys.* **1940**, *8*, 212.

[154] M. Mogensen, N. M. Sammes, G. A. Tompsett, *Solid State Ionics* **2000**, *129*, 63.

[155] W. C. Chueh, C. K. Yang, C. M. Garland, W. Lai, S. M. Haile, *Phys. Chem. Chem. Phys.* **2011**, *13*, 6442.

[156] H. Mehrer, *Diffusion in solids: fundamentals, methods, materials, diffusion-controlled processes*, Springer, Berlin/Heidelberg, Germany, **2007**.

[157] R. W. Balluffi, S. M. Allen, W. C. Carter, *Kinetics of Materials*, **2005**.

[158] J. B. Park, J. Graciani, J. Evans, D. Stacchiola, S. Ma, P. Liu, A. Nambu, J. F. Sanz, J. Hrbek, J. A. Rodriguez, *Proc. Natl. Acad. Sci. U. S. A.* **2009**, *106*, 4975.

[159] Q. Fu, A. Weber, M. Flytzani-Stephanopoulos, *Catal. Letters* **2001**, *77*, 87.

[160] A. Trovarelli, *Catal. Rev. - Sci. Eng.* **1996**, *38*, 439.

[161] W. C. Chueh, Y. Hao, W. Jung, S. M. Haile, *Nat Mater* **2012**, *11*, 155.

[162] W. C. Chueh, C. Falter, M. Abbott, D. Scipio, P. Furler, S. M. Haile, A. Steinfeld, *Science (80-.).* **2010**, *330*, 1797 LP.

[163] E. Sediva, A. J. Carrillo, C. E. Halloran, J. L. M. Rupp, *ACS Appl. Energy Mater.* **2021**, *2021*, 1474.

[164] A. H. Bork, A. J. Carrillo, Z. D. Hood, B. Yildiz, J. L. M. Rupp, *ACS Appl. Mater. Interfaces* **2020**, *12*, 32622.

[165] R. Schmitt, J. Spring, R. Korobko, J. L. M. Rupp, *ACS Nano* **2017**, *11*, 8881.

[166] S. Schweiger, R. Pfenninger, W. J. Bowman, U. Aschauer, J. L. M. Rupp, *Adv. Mater.* **2017**, *29*, 1605049.

[167] T. Montini, M. Melchionna, M. Monai, P. Fornasiero, *Chem. Rev.* **2016**, *116*, 5987.

[168] R. Schmitt, A. Nenning, O. Kraynis, R. Korobko, A. I. Frenkel, I. Lubomirsky, S. M. Haile, J. L. M. Rupp, *Chem. Soc. Rev.* **2020**, *49*, 554.

[169] H. L. Tuller, S. R. Bishop, *Annu. Rev. Mater. Res.* **2011**, *41*, 369.

[170] O. Kraynis, E. Makagon, E. Mishuk, M. Hartstein, E. Wachtel, I. Lubomirsky, T. Livneh, *Adv. Funct. Mater.* **2019**, *29*, 1.

[171] J. L. M. Rupp, E. Fabbri, D. Marrocchelli, J. W. Han, D. Chen, E. Traversa, H. L. Tuller, B. Yildiz, *Adv. Funct. Mater.* **2014**, *24*, 1562.

[172] S. Schweiger, M. Kubicek, F. Messerschmitt, C. Murer, J. L. M. Rupp, *ACS Nano* **2014**, *8*, 5032.

[173] R. Korobko, A. Patlolla, A. Kossoy, E. Wachtel, H. L. Tuller, A. I. Frenkel, I. Lubomirsky, *Adv. Mater.* **2012**, *24*, 5857.

[174] R. Korobko, A. Lerner, Y. Li, E. Wachtel, A. I. Frenkel, I. Lubomirsky, *Appl. Phys. Lett.* **2015**, *106*.

[175] E. Makagon, E. Wachtel, L. Houben, S. R. Cohen, Y. Li, J. Li, A. I. Frenkel, I. Lubomirsky, *Adv. Funct. Mater.* **2021**, *31*, 2006712.

[176] Y. M. Chiang, E. B. Lavik, I. Kosacki, H. L. Tuller, J. Y. Ying, *Appl. Phys. Lett.* **1996**, *69*, 185.

[177] K. Zhou, X. Wang, X. Sun, Q. Peng, Y. Li, *J. Catal.* **2005**, *229*, 206.

[178] Y. Pan, N. Nilius, C. Stiehler, H. J. Freund, J. Goniakowski, C. Noguera, *Adv. Mater. Interfaces*

2014, *1*, 1.

[179] Y. Jiang, J. B. Adams, M. Van Schilfgaarde, *J. Chem. Phys.* **2005**, *123*, 064701.

[180] D. Marrocchelli, B. Yildiz, *J. Phys. Chem. C* **2012**, *116*, 2411.

[181] T. S. Sreeremya, A. Krishnan, K. C. Remani, K. R. Patil, D. F. Brougham, S. Ghosh, *ACS Appl. Mater. Interfaces* **2015**, *7*, 8545.

[182] A. K. B. Elidrissia, M. Addoua, M. Regraguia, C. Montyb, A. Bougrinea, ALaboratoire, *Thin Solid Films* **2000**, *379*, 23.

[183] J. L. M. Rupp, C. Solenthaler, P. Gasser, U. P. Muecke, L. J. Gauckler, *Acta Mater.* **2007**, *55*, 3505.

[184] G. Balakrishnan, S. T. Sundari, P. Kuppusami, P. C. Mohan, M. P. Srinivasan, E. Mohandas, V. Ganesan, D. Sastikumar, *Thin Solid Films* **2011**, *519*, 2520.

[185] L. Y. Kuo, P. Shen, *Mater. Sci. Eng. A* **2000**, *277*, 258.

[186] M. S. AI-Robaee, L. Shivalingappa, K. Narasimha Rao, S. Mohan, *Thin Solid Films* **1992**, *221*, 214.

[187] J. L. M. Rupp, B. Scherrer, A. S. Harvey, L. J. Gauckler, *Adv. Funct. Mater.* **2009**, *19*, 2790.

[188] B. Scherrer, S. Heiroth, R. Hafner, J. Martynczuk, A. Bieberle-Hütter, J. L. M. Rupp, L. J. Gauckler, *Adv. Funct. Mater.* **2011**, *21*, 3967.

[189] S. S. Dana, K. F. Etzold, J. Clabes, *J. Appl. Phys.* **1991**, *69*, 4398.

[190] A. A. Griffith, *Philos. Trans. R. Soc.* **1920**, *221*, 163.

[191] J. Li, A. K. Dozier, Y. Li, F. Yang, Y.-T. Cheng, *J. Electrochem. Soc.* **2011**, *158*, A689.

[192] P. W. Tasker, *J. Phys. C Solid State Phys.* **1979**, *12*, 4977.

[193] T. X. T. Sayle, S. C. Parker, C. R. A. Catlow, *Surf. Sci.* **1994**, *316*, 329.

[194] S. Gates-Rector, T. Blanton, *Powder Diffr.* **2019**, *34*, 352.

[195] T. Suzuki, I. Kosacki, H. U. Anderson, P. Colomban, U. M. R. Cnrs, U. Pierre, **2007**, *14*, 2007.

[196] D. C. Sayle, S. A. Maicaneanu, G. W. Watson, *J. Am. Chem. Soc.* **2002**, *124*, 11429.

[197] E. Aneggi, J. Llorca, M. Boaro, A. Trovarelli, *J. Catal.* **2005**, *234*, 88.

[198] L. Gerward, J. Staun Olsen, L. Petit, G. Vaitheeswaran, V. Kanchana, A. Svane, *J. Alloys Compd.* **2005**, *400*, 56.

[199] P. Yogi, M. Tanwar, S. K. Saxena, S. Mishra, D. K. Pathak, A. Chaudhary, P. R. Sagdeo, R. Kumar, *Anal. Chem.* **2018**, *90*, 8123.

[200] G. Gouadec, P. Colomban, *Prog. Cryst. Growth Charact. Mater.* **2007**, *53*, 1.

[201] S. Saitzek, J. F. Blach, S. Villain, J. R. Gavarri, *Phys. Status Solidi Appl. Mater. Sci.* **2008**, *205*, 1534.

[202] F. Zhang, S. W. Chan, J. E. Spanier, E. Apak, Q. Jin, R. D. Robinson, I. P. Herman, *Appl. Phys. Lett.* **2002**, *80*, 127.

[203] I. O. Mazali, B. C. Viana, O. L. Alves, J. M. Filho, A. G. S. Filho, **2007**, *68*, 622.

[204] H. Richter, Z. P. Wang, L. Ley, *Solid State Commun.* **1981**, *39*, 625.

[205] A. K. Arora, M. Rajalakshmi, T. R. Ravindran, V. Sivasubramanian, *J. Raman Spectrosc.* **2007**, *38*, 604.

[206] Z. V. Popović, Z. Dohčević-Mitrović, M. Ŝćepanović, M. Grujić-Brojčin, S. Aŝkrabić, *Ann. der Phys.* **2011**, *523*, 62.

[207] H. Li, P. Zhang, G. Li, J. Lu, Q. Wu, Y. Gu, *J. Alloys Compd.* **2016**, *682*, 132.

[208] E. Sediva, D. Bohdanov, G. F. Harrington, I. Rafalovskyi, J. Drahokoupil, F. Borodavka, P. Marton, J. Hlinka, *ACS Appl. Mater. Interfaces* **2020**.

[209] R. Gifford, *ChemPhysChem* **2013**, *14*, 2032.

[210] B. Yu, N. Long, Y. Moussy, F. Moussy, *Biosens. Bioelectron.* **2006**, *21*, 2275.